NAVAL POSTGRADUATE SCHOOL

MONTEREY, CALIFORNIA

THESIS

THERMAL MANAGEMENT CAPABILITY OF PHASE CHANGE MATERIAL IN ADDITIVELY MANUFACTURED HEAT SINKS

by

Thomas M. Genito

June 2023

Thesis Advisor:	Walter C. Smith
Co-Advisor:	Claudia C. Luhrs
Second Reader:	David F. Dausen

THIS PAGE INTENTIONALLY LEFT BLANK

REPORT DOCUMENTATION PAGE	*Form Approved OMB No. 0704-0188*

1. AGENCY USE ONLY ***(Leave blank)***	**2. REPORT DATE** June 2023	**3. REPORT TYPE AND DATES COVERED** Master's thesis

4. TITLE AND SUBTITLE THERMAL MANAGEMENT CAPABILITY OF PHASE CHANGE MATERIAL IN ADDITIVELY MANUFACTURED HEAT SINKS	**5. FUNDING NUMBERS**
6. AUTHOR(S) Thomas M. Genito	
7. PERFORMING ORGANIZATION NAME(S) AND ADDRESS(ES) Naval Postgraduate School Monterey, CA 93943-5000	**8. PERFORMING ORGANIZATION REPORT NUMBER**
9. SPONSORING / MONITORING AGENCY NAME(S) AND ADDRESS(ES) N/A	**10. SPONSORING / MONITORING AGENCY REPORT NUMBER**

11. SUPPLEMENTARY NOTES The views expressed in this thesis are those of the author and do not reflect the official policy or position of the Department of Defense or the U.S. Government.

12a. DISTRIBUTION / AVAILABILITY STATEMENT Approved for public release. Distribution is unlimited.	**12b. DISTRIBUTION CODE** A

13. ABSTRACT (maximum 200 words)

This study examines the passive thermal management capability of phase change material (PCM) to maintain thermally loaded parts within a defined temperature window as the PCM isothermally absorbs heat during phase change from solid to liquid. The study is application-based, focusing on a model of a central processing unit (CPU) from a desktop computer. Stearic acid (SA) is selected as the primary PCM based on the operating temperature range of the application, but others also are considered. Simulation models are built for transient thermal loading conditions and are used for heat sink design selection. Liquid metal (aluminum 4008) jet printing additive manufacturing with the Xerox ElemX 3D printer is used for printing parts for the study and developing a design space study for other applications using this thermal management strategy. The study found that incorporating stearic acid into a hollow heat sink lowered the average temperature transient of a modeled CPU by up to 36% compared to heat sinks of similar geometry.

14. SUBJECT TERMS phase-change material, PCM, additive manufacturing, stearic acid, SA, aluminum 4008, central processing unit, CPU, heat sink	**15. NUMBER OF PAGES** 155
	16. PRICE CODE

17. SECURITY CLASSIFICATION OF REPORT Unclassified	**18. SECURITY CLASSIFICATION OF THIS PAGE** Unclassified	**19. SECURITY CLASSIFICATION OF ABSTRACT** Unclassified	**20. LIMITATION OF ABSTRACT** UU

NSN 7540-01-280-5500

Standard Form 298 (Rev. 2-89)
Prescribed by ANSI Std. 239-18

THIS PAGE INTENTIONALLY LEFT BLANK

THERMAL MANAGEMENT CAPABILITY OF PHASE CHANGE MATERIAL IN ADDITIVELY MANUFACTURED HEAT SINKS

Thomas M. Genito
Lieutenant, United States Navy
BS, Pennsylvania State University, 2015

Submitted in partial fulfillment of the
requirements for the degree of

MASTER OF SCIENCE IN MECHANICAL ENGINEERING

from the

NAVAL POSTGRADUATE SCHOOL
June 2023

Approved by: Walter C. Smith
Advisor

Claudia C. Luhrs
Co-Advisor

David F. Dausen
Second Reader

Brian S. Bingham
Chair, Department of Mechanical and Aerospace Engineering

THIS PAGE INTENTIONALLY LEFT BLANK

ABSTRACT

This study examines the passive thermal management capability of phase change material (PCM) to maintain thermally loaded parts within a defined temperature window as the PCM isothermally absorbs heat during phase change from solid to liquid. The study is application-based, focusing on a model of a central processing unit (CPU) from a desktop computer. Stearic acid (SA) is selected as the primary PCM based on the operating temperature range of the application, but others also are considered. Simulation models are built for transient thermal loading conditions and are used for heat sink design selection. Liquid metal (aluminum 4008) jet printing additive manufacturing with the Xerox ElemX 3D printer is used for printing parts for the study and developing a design space study for other applications using this thermal management strategy. The study found that incorporating stearic acid into a hollow heat sink lowered the average temperature transient of a modeled CPU by up to 36% compared to heat sinks of similar geometry.

THIS PAGE INTENTIONALLY LEFT BLANK

Table of Contents

List of Figures

List of Tables

THIS PAGE INTENTIONALLY LEFT BLANK

List of Acronyms and Abbreviations

2D	2-dimensional
Al	aluminum
AM	additive manufacturing
C	Celsius
CAD	computer aided design
cm	centimeters
CPU	central processing unit
DOD	Department of Defense
DSC	differential scanning calorimetry
FM	Field’s Metal
HPHS	hybrid passive heat sink
IHS	integrated heat spreader
LMFA	low-melt fusible alloy
LMJP	liquid metal jet printing
m	meters
mm	millimeters
NI	National Instruments
NIST	The National Institute of Science and Technology
NPS	Naval Postgraduate School

PCM	phase change material
PLA	polylactic acid
RADAR	radio detection and ranging
RPM	revolutions per minute
SA	stearic acid
SEM	scanning electron microscope
STA	simultaneous thermogravimetric analysis
TDP	thermal design power
TEG	thermal energy generation
TIM	thermal interface material
TGA	thermogravimetric analysis
USN	U.S. Navy
UUV	unmanned underwater vehicle
V	volts
W	watts

Acknowledgments

First and foremost, I would like to extend my gratitude and appreciation to Dr. Walter Smith, Dr. Claudia Luhrs and Mr. Dave Dausen for their guidance throughout this project. I have learned and continue to learn an incredible amount from them from subject matter to conducting research to approaching an engineering problem. It has been humbling and enjoyable and to work with them.

I would also like to thank Forest Shaner. I have been genuinely impressed by his productivity, infectious eagerness to learn engineering concepts and tools, and his all-in approach to research and problem solving. It was a pleasure to work with him throughout this project and I look forward to seeing his development throughout this career.

I would be remiss had I not thanked my cohort for their camaraderie through the process. It was a challenge to complete the course work and thesis work, but we all got through it together.

To my instructors, thank you for your instruction throughout the various courses that helped me increase my understanding of engineering problems and solutions so that I could connect and apply concepts, new and old, to this thesis and other courses throughout my time at NPS.

To everyone I've met at NPS, especially throughout this project, I hope to keep in touch.

Finally, I would like to thank my family–Mom, Dad, Michael, John and Kevin–for their unconditional support throughout my time here across the country at NPS. I'm looking forward to coming back to the East Coast and spending more time together.

THIS PAGE INTENTIONALLY LEFT BLANK

CHAPTER 1:
Introduction

1.1 Motivation

1.1.1 Central Processing Units

Thermal management of central processing units (CPUs) is an integral part to the efficient operation of the computing resources. Power is supplied to fans for active cooling of fins via forced circulation to continuously cool the heat sink and draw heat from the CPU. While this is a proven thermal management technique, the power required to operate the fan may not be as readily available as design specifications require. In such a case, performance of electrical components within a computer may start to degrade or experience intermittent failure when temperatures exceed the design operating range [1], [2], measured in degrees (°) Celsius (C). This research aims to prove the capability of using stearic acid (SA) as a phase change material (PCM) for incorporation into additive manufactured hollow parts as a passive thermal management strategy to maintain the average peak temperature of the heat source (the CPU) within +/- 5 °C of target temperature range during operating power cycles. This research is based on a CPU application to establish tangible parameters for experimental designs and testing. The goal is to reduce the average temperature of the CPU reached as it experienced cyclic thermal loading during operations.

1.1.2 Unmanned Underwater Vehicles

In some applications, power supplied to components for active cooling thermal management may be detrimental to the sustainability of the device. An example of such a device is an unmanned underwater vehicle (UUV). As power is consumed by the battery for the internal components such as sensing devices, less power is available for propulsion and operation of sensory equipment in the UUV. This limits the time available per charge to complete, for example, U.S. Navy (USN) mission essential tasks such as ocean floor mapping and environmental data collection. PCM-based UUVs have been developed to attempt to solve this problem. A PCM-based UUV takes advantage of the PCMs heat absorption during solid-liquid phase change to store thermal energy, which is later converted to electrical energy, supplying power to the UUV [3]. Figure 1.1 shows the conceptual design for using PCMs as an energy storage and supply mechanism. However, the thermal energy created is limited by the temperature difference between the ocean surface and at depth. Moreover, the power conversion efficiency is low for PCM-based UUVs due to the relatively low thermal conductivity of wax-based PCMs [3]. This research is focused on energy storage for heat dissipation rather than for energy conversion. Thus, in addition to the goals of Section 1.1.1, the research aims to show that utilizing the PCM to limit peak temperatures of operating electronic components for longer operational cycles is potentially an alternative to using PCMs for energy generation.

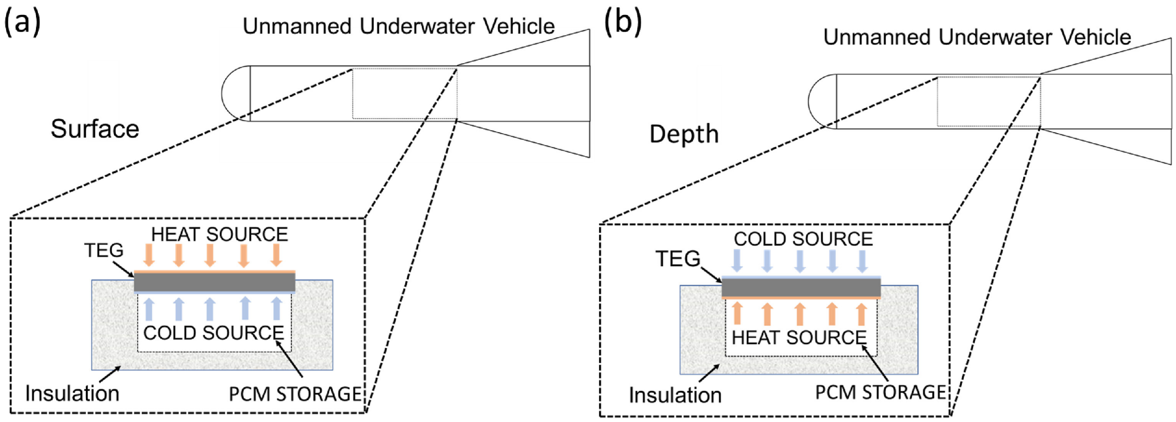

Figure 1.1. Conceptual design for PCM-based UUV for TEG (a) at the surface and (b) at depth. Source: [3].

1.1.3 RADAR Systems

Systems aboard USN ships such as radio detection and ranging (RADAR) are another example of a system that is subject to cyclic thermal loads. Except, these systems reach much higher temperature than a CPU or UUV. Figure 1.2 shows an example of a RADAR system aboard a USN vessel.

Figure 1.2. RADAR system. Source: [4].

Liquid cooling technologies are generally used for these systems [4]. Heat rejection through liquid-to-air heat exchanging loops or chiller systems are effective but can be expensive and cumbersome to maintain. Isothermal conditions within a RADAR system are crucial to their optimal performance. Thus, there exists a potential to use PCM as a thermal management strategy for transient temperature changes and minimize the temperature fluctuations of a RADAR system during operations.

1.1.4 Traditional Forced Convection Cooling

Restricted Space Availability

Traditional heat sinks within CPUs are typically finned metal blocks that are cooled by forced convection via a small axial flow fan. A challenge when employing traditional forced convection is space availability. To ensure air is adequately circulated for cooling there must be sufficient space around components for air to flow, to include the space external to the computer at fan intake. Consequently, the performance of a fan is also environment dependent, relying on air purity for sustained operation since contaminant-filled air can cause a buildup of dust within a fan. The buildup from dust can reduce cooling capability of the fan and act as thermal insulation to heat generating components within a computer [2]. Figure 1.3 shows dust contamination for heat generating (power supply) and thermal management (cooling fan, heat sink) components in a desktop computer. It is therefore imperative to research passive thermal cooling alternatives to forced convection cooling techniques that can be implemented into confined spaces.

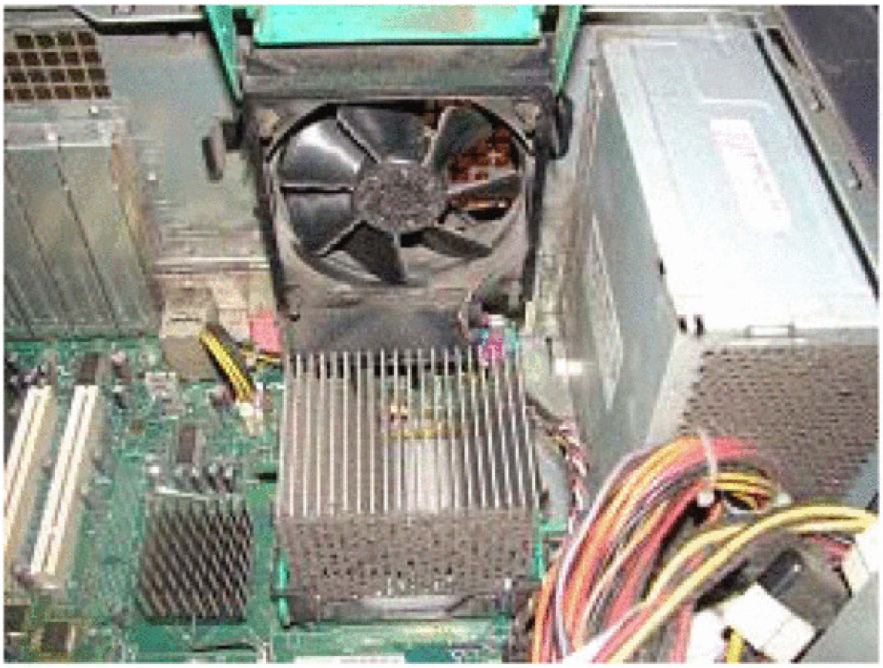

Figure 1.3. Dust contamination on power supply, heat sink, and cooling fan of a desktop computer. Source: [2].

Noise

Noise production is also a concern in forced convection cooling. An increase in fan speed for a CPU described in Section 1.1.1 improves cooling rate but increases noise production. An increase in fan speed will result in an increase in noise as given by

$$dB2 = dB1 - 50\log_{10}(RPM1/RPM2), \tag{1.1}$$

where dB2 is the final sound level, dB1 is the initial sound level, RPM2 is the final fan speed and RPM1 is the initial fan speed. This is known as a “soft failure” of the fan, which is ergonomically unfavorable [2]. User alteration of fan speed to reduce noise production leads to a trade-off between processing performance and ergonomic preferences of the user. For example, consider the case of a desktop computer where the “Quiet” setting is selected via Power Manager [5]. As cooling fan speeds and processing power are lowered for noise reduction of the computer, system performance is reduced and the computer is subjected to increased system surface temperature [5]. Though tip clearance optimization of fan blades has been evaluated as a potentially effective design to reduce noise levels while maintaining cooling capacity, improvements in design are limited by the ability to maintain the design specification dimensions of the fan blades [6]. Dust buildup, as previously described, can be a contributing factor to a deviation of fan blade dimensions from design specification.

1.2 Problem Statement

The capability of PCMs has been a developing research area for thermal management, especially for metal PCMs where the melting point can be tailored for a given application. Current heat sinks rely on active cooling to regulate the temperature of an operating component. If the active cooling is lost, the the lack of temperature regulation subjects the operating component to high peak and average temperatures, large thermal transients and a variable operating temperature band over thermal cycles (heating and cooling). This negatively effects the efficiency of electrical components and subjects the chassis of the components to thermal mechanical stresses. Incorporation of PCM into channels of hollow structures provides the potential a passive thermal management method to regulate the average temperature of an operating component within a narrow band by absorbing latent heat of fusion and dissipating it over a long period of time. Part creation using additive manufacturing (AM) techniques provides the ability to develop hollow structures with complex geometries that may be suitable for PCM storage. Recent studies showing the development of hollow parts with AM methods as well as the infusion of PCM within the porous structure suggests the potential for inclusion of PCM into the cavity of hollow manufactured parts [7], [8]. This study seeks to determine the capability of AM to create hollow structures with channels for inclusion of PCM as an enhanced passive thermal management technique. The implementation of a passive thermal management technique that does not rely on forced convection techniques would permit the enclosure of the operating environment and mitigate traditional cooling method issues discussed in Section 1.1.4.

By including PCM into an additively manufactured hollow heat sink, this study aims to test the ability to achieve the following goals when compared to heat sinks of similar geometries:

- Reduce the average temperature of a cyclically thermally loaded component.
- Reduce the peak temperature of a cyclically thermally loaded component.
- Regulate the thermal transient by maintaining the temperature of a cyclically thermally loaded component within a narrow, consistent temperature range.

This research seeks to contribute the following to the fields of thermal management and additive manufacturing:

- Establish a heat sink design methodology which can be applied and repeated for any PCM.
- Develop efficient methods for adding PCM into hollow parts.
- Prove the capability of using a PCM within additively manufactured parts as a passive thermal management technique to reduce the average peak temperature of a temperature-sensitive component during operation-induced cyclic thermal loading.
- Prove the capability of using AM methods for thermal management device manufacturing.

1.3 Overview of the Document

The document begins with a review of literature of applicable studies and related problems in Chapter 2. It outlines studies and other research applicable to the selected PCM and AM technique as well as the material compatibility. Heat transfer fundamentals are then reviewed to narrow the focus of the reader to the applicable heat transfer concepts for this work. Given that this research uses over the counter materials that were not specifically designed for thermal management and, instead, have other primary uses (i.e., food additives, cosmetics), discrepancies between cited reference values and empirical observations are discussed.

Chapter 3 discusses the experimental methods of the work. The chapter is organized such that the order of the sections can be used as a general reference procedure for heat sink design with PCM incorporation into additively manufactured parts for any application. First, it discusses the application selection for a component subject to thermal cyclical loading. The selected AM method is then discussed along with an evaluation of the compatibility of the design space of the printer with the selected application. The design space code is discussed in detail, explaining the equations used and basis for parameters.

The PCM selection process is then discussed, ultimately concluding with the PCM selection based on melting point, availability and non-toxicity. It is compared to other potential PCMs and their thermophysical properties as well. The AM method selection and PCM selection is integral to understanding the bases for the design of follow-on test procedures discussed in this chapter so it is initially presented in this chapter instead of the results and discussion chapter (Chapter 4).

The process for printing hollow heat sinks with the selected AM method is then shown followed by the procedure for adding the selected PCM into a hollow part. The two-step printing process to additively manufacture a hollow part as well as the filling of PCM into the part are new techniques and, thus, are presented in a procedure-like format.

With the PCM added into the printed hollow part, the behavior (expansion, potential for leakage) of the PCM within the container is discussed, presenting a density test and sealant test to understand and respond to PCM expansion during heating. A thermal conductivity test is developed and outlined in a procedure-like format with the goal of ensuring the conductive characteristics of the metal container were not inhibited by the PCM inside.

Design strategies are then presented which include potential methods for incorporation of the PCM into the part to maximize thermal management potential. The designs are evaluated for practicality of development with the constraints of the given AM technique and PCM selection. The designs are then simulated using ANSYS 2-dimensional (2D) transient thermal simulations to determine the relative ability of each design to thermally manage a constant heat load. The design basis, including the required amount of the selected PCM to thermally manage the application heat load, for the heat sink vessel is introduced. However, the final design is not discussed until Chapter 4 as the final design is based on the ANSYS simulation results.

Finally, the experimental test procedure is described, sequentially walking through the set up of the test rig and execution methodology of the power cycle tests. There are two sets of power cycle tests. One is for short duty cycles over a long period (30 seconds on at high power heat load, 30 seconds off for many cycles) and the other is for a long duty cycle over a short testing period (hundreds of seconds on at high power heat load, hundreds of seconds off for a few cycles). These are done to ensure the goals of the study are met with minimal bias. The chapter concludes with a summary of comparable heat sink mediums used as controls to validate the power cycles testing.

Chapter 4 presents and analyzes the results produced from the experimental methods of Chapter 3. It follows the same flow to reiterate the procedure-like organization of the document.

Each aspect of the design space is evaluated with respect to the selected application to ensure the printer is capable of supporting heat sink generation for the study. For context and future work considerations, the entire design space of the printer is presented in the chapter.

Charging (heating up) and cooling data for the PCM within a container of the printed material is presented as a comparison to the characteristic shape of a PCM, suggesting comparable thermal management potential of the selected PCM to other PCMs.

Density data is provided, highlighting the need for a sealant to contain the PCM during heating due to density-induced expansion. Thermal conductivity data is analyzed to ensure a balance of heat flow through the part and heat absorption of the PCM as to not inhibit the heat sink from continuously drawing heat from the heat source.

The results of the ANSYS 2D transient thermal simulations are presented, which are used to generate the final heat sink vessel design. The internal volume of the final design is validated to be adequate to properly absorb a conservative heat load estimate. Finally, the results of all power cycle tests are presented along with a corresponding summary of the primary observation and analysis of heat sink success compared to heat sinks of similar geometry.

Chapter 5 focuses on developing the concept past the methodology presented in Chapter 3. With the design process established and the results analyzed, Chapter 5 seeks to improve upon the results and offer alternative methods of achieving the goals of Section 1.2. It discusses the process of adding a metal PCM into a hollow part during the print process to minimize penetrations into the part during post manufacturing filling, as done with the original PCM. This is also applicable to future work considerations were a metal PCM may be desired. The results of a thermal conductivity test are also presented for a container with the metal PCM enclosed for comparison to the results with the organic PCM in Chapter 4. A second idea is presented regarding the use of natural circulation to explot the convection capability of the PCM as it moves through a channel following phase transition. This is presented to improve on results of the short duty cylce, long test duration results since the PCM did not have adequate time to solidify and the advantage of using latent heat of fusion absorption was not as effective.

The document concludes with Chapter 6, summarizing conclusions and presenting suggestions for future work to expand on this research.

THIS PAGE INTENTIONALLY LEFT BLANK

CHAPTER 2:
Literature Review

2.1 PCM as a Thermal Management Strategy

Sensible heat absorption in a material increases its temperature whereas latent heat is absorbed isothermally. Figure 2.1 shows the enthalpy vs. temperature plot during such a phase change.

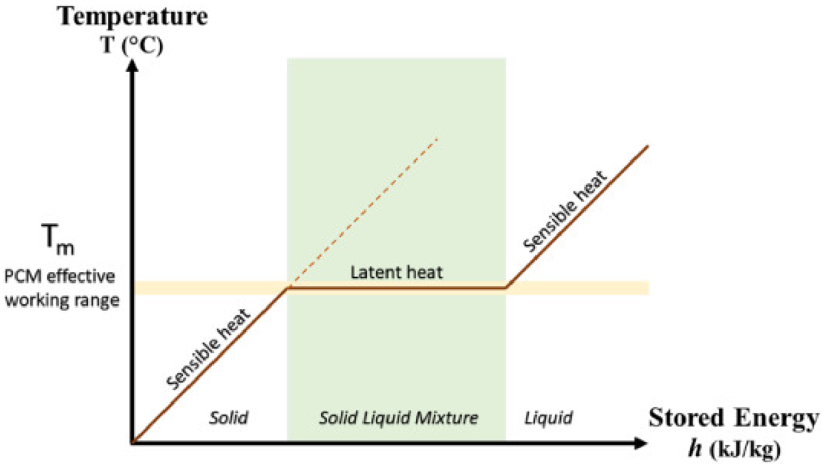

Figure 2.1. Characteristic shape of temperature vs. stored energy (enthalpy) curve during solid-liquid phase change. Source: [9].

As cooling and heating occurs in a PCM, it exhibits a “shark fin” shape as seen in Figure 2.2. Temperature does not continuously rise in the charging portion of the cycle despite a constant heat load, illustrated by the flattened slope during the latent heat of fusion transfer regions for both the heating and cooling cycles. Latent heat of fusion absorption can serve as a passive thermal management technique to reduce the average temperature of a component during cyclic thermal loading.

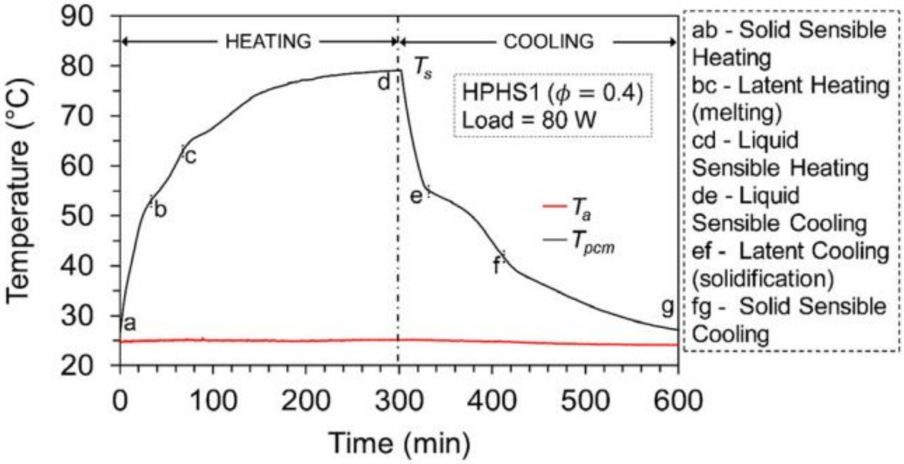

Figure 2.2. Graph of the heating and cooling cycles of a (HPHS) with 0.4 volume fraction (ϕ) of paraffin wax for cooling of a battery charger. Source: [10].

2.2 PCM Applications

PCMs as a thermal management strategy is not a new idea. Many types of PCMs have been used an developed in various applications in the field of thermal management. Figure 2.3 shows the classification of PCMs within the context of thermal energy storage, which can be formed into composites for thermal management.

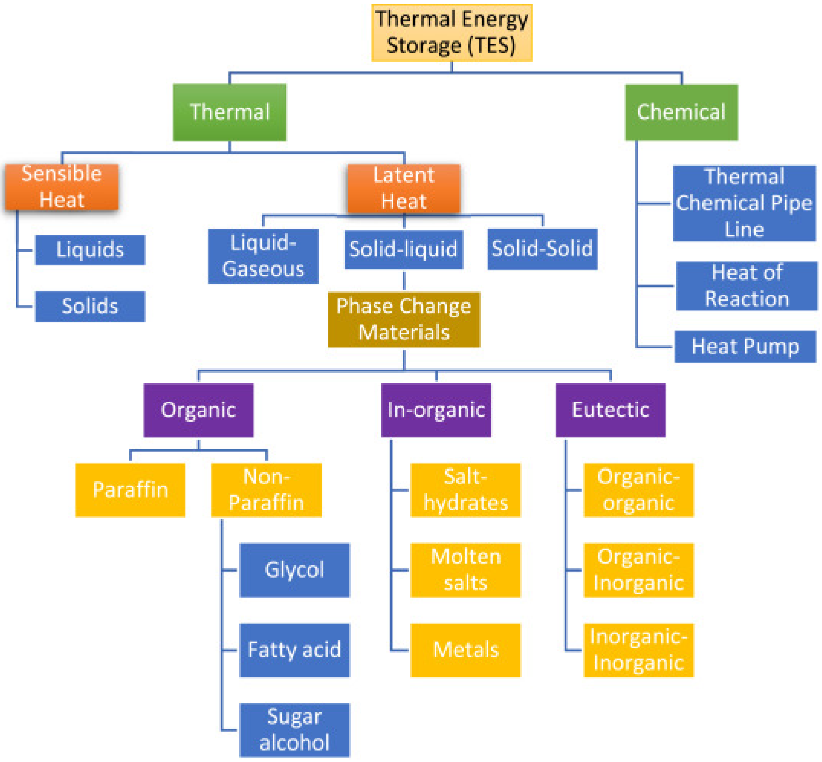

Figure 2.3. A chart of the classification of PCMs. Source: [9].

Latent heat is absorbed during liquid-gaseous, solid-liquid and solid-solid transitions. PCMs are a subset of the solid-liquid transition. There are three categories of PCMs: organic, inorganic and eutectic. Organic PCMs are subdivided between paraffins and non-paraffins (fatty acids, sugar alcohols). They are typically wax-like substances in their solid form and tend to have a relatively low melting point. Their thermal instability based on density changes over a given temperature gradient make them a challenging material for thermal management if the intention is to limit a local heat-affected area to a given temperature. Inorganic PCMs are comprised of salt-hydrates, molten salts and metals. Their enthalpy and melting points tend to be higher than organic PCMs. Eutectic PCMs are composites of the organic and/or inorganic categories. Their melting points can be tailored for various temperature and thermal load applications. Figure 2.4 shows the ranges of enthalpy and temperature ranges for some of the different classes of PCMs.

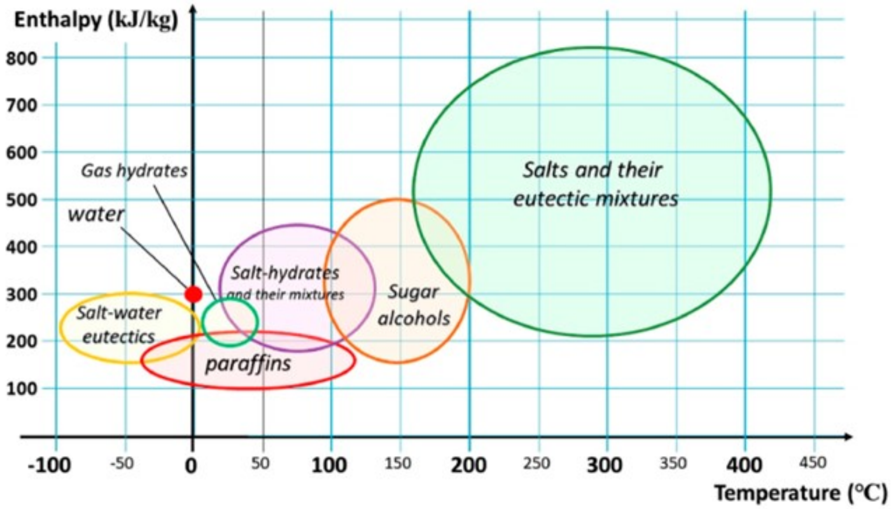

Figure 2.4. Enthalpy vs. temperature for various classification of PCMs. Source: [9].

Figure 2.5 summarizes the advantages and disadvantages of the PCM types. Green text shows a particularly advantageous characteristic while red text shows a particularly disadvantageous characteristic. Tradeoffs between their thermophysical properties are dependent on the application. While salt-hydrates have high melting temperatures for higher temperature thermal management applications, their corrosive behavior is a material concern. Their instability over repeated cycles also makes them less preferred for cyclic thermal loading applications. Non-paraffin organics offer a wide range of potential applications, but are expensive and can experience permanent degradation if the container reaches high temperatures. Metallics are advantageous with respect to thermal cycling but their relatively low latent heat properties limit their effectiveness. Weight can also be a concern, particularly for space systems applications, and must be factored into the PCM selection process.

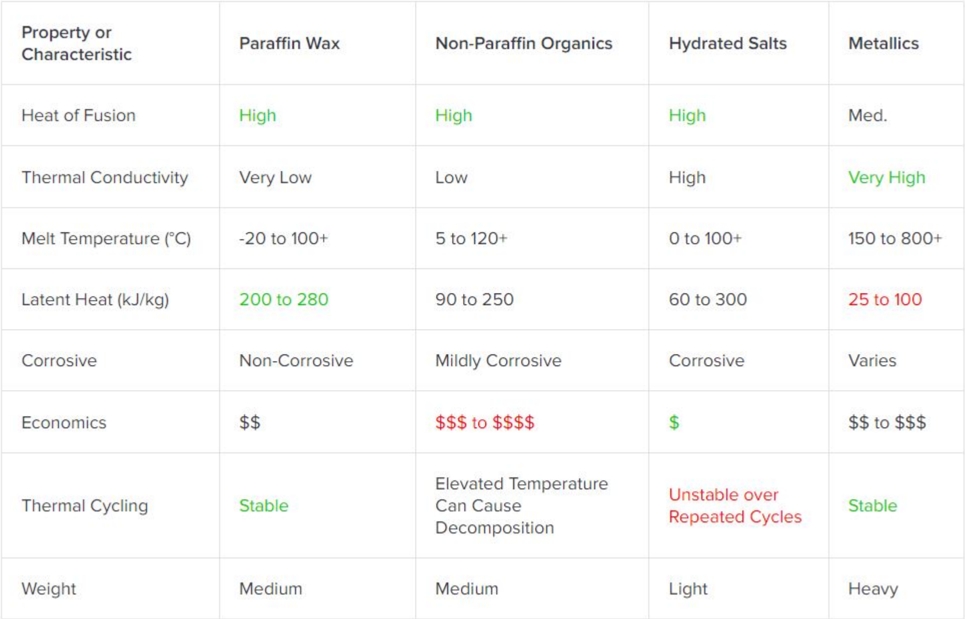

Property or Characteristic	Paraffin Wax	Non-Paraffin Organics	Hydrated Salts	Metallics
Heat of Fusion	High	High	High	Med.
Thermal Conductivity	Very Low	Low	High	Very High
Melt Temperature (°C)	-20 to 100+	5 to 120+	0 to 100+	150 to 800+
Latent Heat (kJ/kg)	200 to 280	90 to 250	60 to 300	25 to 100
Corrosive	Non-Corrosive	Mildly Corrosive	Corrosive	Varies
Economics	$$	$$$ to $$$$	$	$$ to $$$
Thermal Cycling	Stable	Elevated Temperature Can Cause Decomposition	Unstable over Repeated Cycles	Stable
Weight	Medium	Medium	Light	Heavy

Figure 2.5. Advantages and disadvantages for various classification of PCMs. Source: [11].

PCM selection is largely application dependent for melting temperature considerations. Environmental engineering and civil engineering are two prominent fields that rely on effective thermal engineering designs within to solve some of their most difficult problems. For example, fish and aquatic vegetation depend on water temperatures to sustain the ecosystem and PCMs can be used to regulate water temperatures [12]. For civil engineering, proper insulation pays dividends in future costs to the customer and PCMs are being researched as a viable thermal management strategy to solve the issue [13]. There have also been studies that have researched composites for metal and organic PCMs to attempt to exploit the advantages of each since they have very different thermal conductivities and melting temperatures [14].

2.3 PCM and Container Material Interactions

Another consideration of PCM selection is the interaction between the PCM and its container material used for the heat sink development. Interactions between various PCMs, by classification, have been studied. Organic, inorganic, and metal PCMs all interact differently with different container materials, particularly metal containers. Phase segregation, corrosion of the container material and degradation of the PCM lead do degradation of energy storage PCM performance. Aluminum, brass, carbon steel and copper have been studied as potential suitable containers for various PCMs. The least compatible combination was between carbon steel and inorganic PCMs while aluminum was most suitable container for all PCMs [15]. A separate experiment showed significant corrosion concerns following consistent application of a thermal load with a metal PCM and an aluminum container [16]. The primary criteria for this conclusion was the level of corrosion based on mass loss and observable color changes to the PCM-container interface [15]. In a separate study with a salt-hydrate PCM in an acrylic glass container, phase segregation occurred following continuous thermal cycling, causing a decrease in thermal energy storage capability of the PCM [17]. An effective method for understanding material interaction is simultaneous thermogravimetric analysis (STA), where multiple material testing techniques are combined to determine compatibility of materials under a thermal load and obtain thermophyiscal properties of the material from the data. This may include tests that measure heat flow and peak temperatures reached over many cycles. A scanning electron microscope (SEM) can be used to see microscopic behavior of the material and observe corrosive interactions of materials, for example. The SEM observations could be done following the STA testing and combined with the STA data for a complete understanding of material compatibility between a PCM and container material. Based on the variety of results for different PCM and container material studies, it is imperative to understand the effect of the container material and thermal loading on the selected PCM before implementation into a thermal energy storage device design.

2.4 Additive Manufacturing

Selection of a method to create a part to incorporate PCM into a cavity for storage and thermal management use requires knowledge of the capabilities of additive manufacturing techniques. Additive manufacturing is a technique that produces objects layer-by-layer instead of traditional subtractive manufacturing which removes sections of a whole piece of material to create a final part [18]. There are seven categories as shown in Figure 2.6.

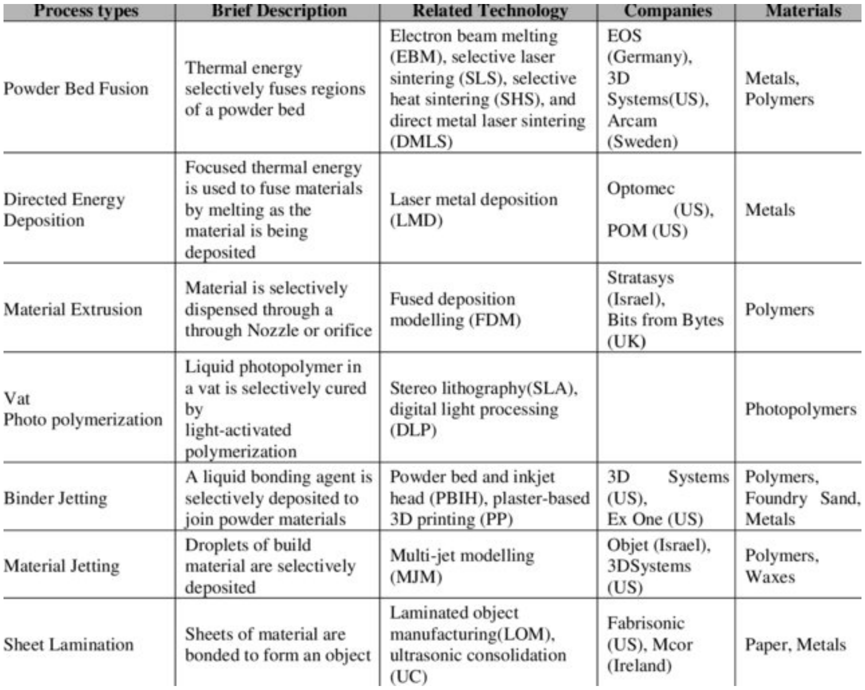

Process types	Brief Description	Related Technology	Companies	Materials
Powder Bed Fusion	Thermal energy selectively fuses regions of a powder bed	Electron beam melting (EBM), selective laser sintering (SLS), selective heat sintering (SHS), and direct metal laser sintering (DMLS)	EOS (Germany), 3D Systems(US), Arcam (Sweden)	Metals, Polymers
Directed Energy Deposition	Focused thermal energy is used to fuse materials by melting as the material is being deposited	Laser metal deposition (LMD)	Optomec (US), POM (US)	Metals
Material Extrusion	Material is selectively dispensed through a through Nozzle or orifice	Fused deposition modelling (FDM)	Stratasys (Israel), Bits from Bytes (UK)	Polymers
Vat Photo polymerization	Liquid photopolymer in a vat is selectively cured by light-activated polymerization	Stereo lithography(SLA), digital light processing (DLP)		Photopolymers
Binder Jetting	A liquid bonding agent is selectively deposited to join powder materials	Powder bed and inkjet head (PBIH), plaster-based 3D printing (PP)	3D Systems (US), Ex One (US)	Polymers, Foundry Sand, Metals
Material Jetting	Droplets of build material are selectively deposited	Multi-jet modelling (MJM)	Objet (Israel), 3DSystems (US)	Polymers, Waxes
Sheet Lamination	Sheets of material are bonded to form an object	Laminated object manufacturing(LOM), ultrasonic consolidation (UC)	Fabrisonic (US), Mcor (Ireland)	Paper, Metals

Figure 2.6. The seven additive manufacturing categories. Source: [18].

Material extrusion uses polymeric printing material known as polylactic acid (PLA). However, the thermal conductivity of pure PLA is approximately 0.183 W/mK [19]. This value shows that PLA is very resistant to heat flow and would not suffice as a heat sink material. Additionally, its glass transition temperature is around 55 °C to 60 °C, which causes softening and structural deformity [19]. This may be too limiting with regard to most applications. Therefore, techniques that print metals are preferred for heat sink design. The powder bed fusion technique, used in an Electro Optical Systems (EOS) printer, is incapable of printing hollow parts and its printed material (titanium) does not permit ease of post-manufacturing. For the other AM printing processes that print metals, printing hollow parts is a significant challenge or not possible. A relatively new AM technique, liquid metal jet printing (LMJP), provides the capability of printing hollow parts [20]. In this process, metal filament wire is fed through tubing into a heated reservoir. The wire melts in the reservoir and coils surrounding the reservoir are pulsed with current, inducing a magnetic field. This causes a magnetohydrodynamic pressure in the reservoir, ejecting metal droplets onto a cooler bed plate. The lower temperature of the bed plate causes solidification of the metal and adherence of the droplet to the bed plate or previously printed layers. It prints drop by drop, layer by layer along a bed plate moving in the x and y directions to build the structure. The Xerox ElemX printer uses LMJP to build structures. Limitations of printing dimensions and geometries continues to be researched, but ample data is available for most parts [7]. The print process can be paused at any time, allowing an operator to inspect the part since the head moves up in the z direction during the pause process. In addition to hollow parts, this AM technique allows for the creation of parts with unique shapes to fit into unused voids and internal geometries of temperature sensitive components. The creations of parts with these qualities also cannot be done with traditional subtractive manufacturing methods. Finally, the aluminum (Al)-4008 metal used in the Xerox ElemX is very thermally conductive (148 W/mK) so it is advantageous as a heat sink material [21].

2.5 Heat Transfer Fundamentals

To narrow the conceptual scope heat sink design and application, heat transfer fundamentals are reviewed. Conduction and convection are the primary modes of heat transfer in any heat sink design. Thus, conduction and convection are reviewed prior to discussing general heat sink design.

2.5.1 Conduction

Conduction heat transfer occurs when heat is transferred between two materials in contact. The rate of heat transfer is proportional to the surface area and thermal gradient [22]. The rate of heat transfer is also proportional to the thermal conductivity of the material. The thermal conductivity of a material is analogous to a resistor in an electrical system. It is an intrinsic property of a material that determines its ability to conduct (or resist) the flow of heat through it. Given a constant thermal gradient and relatively constant thermal conductivity over a limited temperature range, the resulting rate of heat transfer is primarily driven by the surface area for which the heat flows through. Thus, designing interior features in a heat sink with larger surface areas is imperative to optimally drawing heat from the heat source and delivering it to the PCM. Fourier's Law, shown in Eq. 2.1, can be used to describe conduction and is given by

$$q = -k \cdot A \cdot \nabla T, \tag{2.1}$$

where q is the rate of heat transfer, k is the thermal conductivity, A is the heat transfer area, and T is the temperature.

2.5.2 Convection

Convection heat transfer involves a cooling fluid flowing over a material, removing the energy from the hotter material. As heat is transferred from the hotter material to the colder fluid, the density of the fluid decreases and sinks, allowing for follow-on cooling. As the local area temperature stabilizes, air density becomes relatively constant surrounding the heated material, reducing the rate of heat transfer. Unless forced air is used, the relatively constant density air will remain stagnant around the material, as indicated by a lower convection coefficient magnitude (5-25 W/mK) [22]. This is the underlying concept of natural (free) convection, which is essentially a passive heat transfer mechanism. Similar to conduction, the heat flux due to convection is proportional to the surface area of the heat sink. The convection equation, shown in Eq. 2.2, is given by

$$q = h \cdot A \cdot \nabla T, \tag{2.2}$$

where h is the convection coefficient of a fluid moving across the surface of a material.

2.6 Heat Sink Design

When designing a heat sink, material selection, shape of the heat sink and the use of fins to extract heat from the source and expand the heat transfer surface area play a crucial role in the success of the thermal management capability of a heat sink. It is especially important when forced circulation is available, but effective fin design can also be advantageous in a free convection environment. Fin performance is quantified by fin effectiveness and fin efficiency. Fin effectiveness, ϵ_f, is the fraction representation of the improved heat transfer rate of a heat sink with fins compared to one without fins and is given by

$$\epsilon_f = \left(\frac{q_f}{h \cdot A_{c,b} \cdot \theta_b}\right), \tag{2.3}$$

where q_f is the fin heat transfer rate, h is the convection coefficient, $A_{c,b}$ is the cross-sectional area of the fin at the base and θ_b is the difference between temperature at the base and the surrounding environement. Equation 2.3 reveals several characteristics about a well-designed fin array. First, a large perimeter and low cross-sectional area, as accomplished by using thin fins spaced closely together, is an effective heat sink design so long as the spacing is adequate for convective cooling flow of the surrounding fluid [23]. Second, for a given convection coefficient, a material with a higher thermal conductivity is preferred to improve thin effectiveness. Metals such as aluminum, steel and copper are thermally conductive and could be suitable options for a heat sink material. However, cost, weight and manufacturability must be considered when developing the heat sink. In AM, for example, a metal suitable for printing could allow for the creation of complex shapes and geometries. Fin efficiency, η_f, is also used to quantify the performance of a finned heat sink and is given by

$$\eta_f = \frac{q_f}{q_{max}}, \tag{2.4}$$

where q_f is the heat transfer rate of the fin and q_{max} is the maximum heat transfer rate of a fin at base temperature (no conduction resistance-induced temperature gradient). Fin efficiency is dependent on the fin shape. Straight fins, circular fins and pin fins are common fin shapes. The slopes of each fin shape from the base to the tip are also variable and also effect the fin efficiency. Depending on the manufacturing method, straight fins may be preferred since they are easier and cheaper to manufacture especially in the case of triangular straight fins were less volume of material is required for sufficient heat transfer rates compared to rectangular straight fins. Given a tubular geometry, annular fins can also be considered for heat sink design improvement. Finally, the performance of a fin array on a heat sink can be quantified by the overall surface efficiency, which is the extrapolated efficiency of one fin to an array of the same fin shape and design. Since this is dependent on geometry and dimensional constraints of the heat sink, it is imperative to choose a fin design that sufficiently rejects heat to the environment.

2.7 Reference Value Discrepancies

Even though a heat sink may be optimally designed and a selected PCM may seem to have the correct thermophysical properties for a given application, the cited reference values may not be accurate and may affect the ability of a heat sink to manage a thermal load. Though metal PCMs are designed for thermal management applications, organic and inorganic PCMs are still being researched for their thermal management potential. The original use of many organic PCMs have resulted in limited published and reliable data for their thermophysical properties. Some examples of original uses of organic PCMs include cosmetics, food additives and candles [24]. Furthermore, there is not a consolidated collection of this data for all PCMs. The National Institute of Science and Technology (NIST) publishes data based on available research, but is not always up-to-date and the research is largely inconsistent. This complicates the PCM selection process since, without defined thermophysical properties with minimal uncertainty, a heat sink or thermal absorption system must be designed to a range of values.

THIS PAGE INTENTIONALLY LEFT BLANK

CHAPTER 3:
Experimental Methods

This chapter explains the procedural method for the heat sink design and testing. The sections are organized such that this sequence of methodology can be applied to any research project involving additively manufacturing a hollow heat sink for the purpose of incorporating PCM for thermal management. No results of empirical tests used in the development or testing of the heat sink are presented in this section. Rather, this chapter aims to outline a repeatable procedure for other applications using the strategy of this research.

First, it the application for this research is selected for a component subject to thermal cyclical loading. The selected AM method is then selected and discussed along with an analysis of the design space of the printer to ensure it is adequate for the selected application. The PCM selection process is then selected and compared to PCMs of similar thermophysical properties, ultimately concluding with the PCM selection based on melting point, availability and non-toxicity. The process for printing hollow heat sinks with the selected AM method. This process if followed by the procedure for adding the selected PCM into a hollow part.

With the PCM added into the printed hollow part, the behavior (expansion, potential for leakage) of the PCM within the container is discussed. Density and sealant test are generated and discussed to understand and respond to PCM expansion during heating. A thermal conductivity test is developed and outlined in a procedure-like format with the goal of ensuring the conductive characteristics of the metal container were not inhibited by the PCM inside.

Design strategies are then presented which include potential methods for incorporation of the PCM into the part to maximize thermal management potential. The designs are evaluated for practicality of development within the constraints of the given selected AM technique and selected PCM. The designs are then simulated using ANSYS 2D transient thermal simulations to determine the relative ability of each design to thermally manage a constant heat load. The design basis for the printed heat sink vessel, including the required amount of the selected PCM to thermally manage the application heat load, is also introduced.

Finally, the experimental test procedure is described, sequentially walking through the set up of the test rig and execution methodology of the power cycle tests. The chapter concludes with a summary of comparable heat sink mediums used as controls to validate the power cycles testing.

3.1 Application Selection

The application for this study is an i5 Intel® 6th Generation Intel Core^{TM} processor found in a Dell OptiPlex 5040 desktop computer [25]–[27]. The primary CPU thermal parameters of concern for this study are the thermal design power (TDP), measured in watts (W), and case temperature (T_{CASE}), measured in °C. The TDP "represents the average power, in watts, the processor dissipates when operating at Base Frequency with all cores active under an Intel-defined, high-complexity workload" and the T_{CASE} is "the maximum temperature allowed at the processor integrated heat spreader (IHS)" [25], [26]. The purpose of the IHS, as illustrated in Figure 3.1, is the evenly distribute heat from the heat source to the heat sink, maximizing the rate of heat transfer for a given heat flux, q" [28].

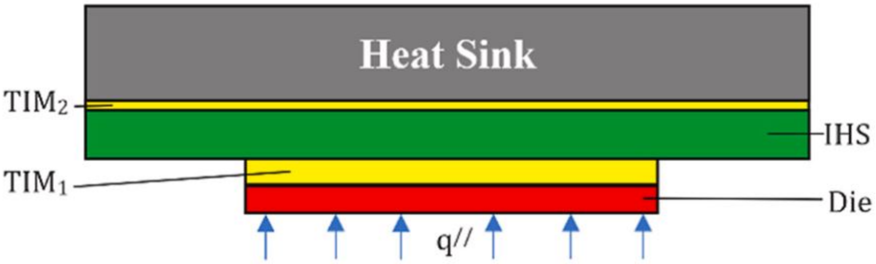

Figure 3.1. Graphic of IHS in between TIM. Source: [28, Figure 1(b)].

Based on T_{CASE}, The 6500T and 6500 model CPUs are operationally limited to 66 °C and 71 °C, respectively. Based on TDP, the 6500T and 6500 model CPUs are operationally limited to 35 W and 65 W, respectively. Therefore, the target temperature and target supply power for testing in this research is within the ranges of 66 °C to 71 °C and 35 W to 65 W, respectively. The dimensions, as measured in centimeters (cm), of the CPU are 3.2 cm x

3.2 cm, which form the basis for the contact area between the heat source and the heat sink for experimental testing.

3.2 AM Method

3.2.1 AM Method Selection

Based on the purpose of this research, the heat sink generated needed to be hollow with channels that supported the filling of PCM. Therefore, the AM method selected was LMJP based on its ability to allow for the creation of complex geometry, including hollow parts, and facilitate post-manufacturing [7]. The Xerox ElemX 3D printer was used during part creation. Parts were designed in SolidWorks computer aided design (CAD) software then sliced using the Xerox-provided slicing software in preparation for printing. The printed metal was Al-4008, which is very thermally conductive and consists of 7 % Si, 0.08 % Fe, 0.4 % Mg, and 0.08 % Ti. The bed plate temperature was 475 °C and the reservoir temperature was 825 °C.

3.2.2 Design Space Study

The design space of the printer used for AM needed to be verified to be adequate for creating heat sinks that would dimensionally and thermally (based on material and geometry) fit the application. The design space study was completed using the parameters of the ElemX printer. The base code was developed to be customizable for any 3D printer and was adjusted to tailor the code to the parameters of the ElemX printer used in this study [29]. It can be found in Appendix A. The natural convection coefficient was assumed to be 10 W/mK and the thermal conductivity was assumed to be 148 W/mK based on 4000 series Al. The base thickness was assumed to be a minimum of 3 millimeters (mm) and the mass was limited to 0.9 kg based on printing limitations. For reference, the mass of the heat sink in this project was approximately 0.23 kg. The variables considered were heat sink power throughput, heat sink mass, and heat sink footprint area, and the number of fins. A straight triangular shaped fin was used in the study, similar to the image in Figure 3.2. The straight triangular shaped fin was advantageous for weight limitations and overall surface efficiency of the fin since “for equivalent heat transfer, it requires much less volume (fin material) than a rectangular profile” [23].

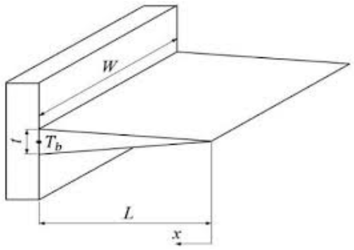

Figure 3.2. Straight triangular fin. Source: [30].

First, the volume of the heat sink base, V_{base}, is calculated as given by

$$V_{base} = w \cdot St_b \cdot N_{fins},$$

where w is the width of one fin, S is the sum of the thickness of one fin and its spacing from another fin, t_b is the base thickness and N_{fins} is the number of fins on the heat sink. The variables w and N_{fins} are elements of arrays developed based on ElemX dimensional constraints. The uniform fin height, finheight, is then calculated, given by

$$h_{fin} = \sqrt{L^2 + (t/2)^2},$$

where L is an element of the fin length array, and t is the fin thickness [23]. The uniform fin height is then used to calculate the area of the fin, A_f, given by

$$A_f = 2 \cdot w \cdot (h_{fin}). \tag{3.1}$$

For mass calculation, the volume of each fin, V_f, is also calculated as given by

$$V_f = 0.5 \cdot t \cdot w \cdot (h_{fin}). \tag{3.2}$$

With the individual fin dimensions calculated, the individual fin efficiency is then calculated. The individual fin efficiency, η_f, for a straight triangular fin is given by

$$\eta_f = \frac{1}{m \cdot L} \frac{I_1(2 \cdot m \cdot L)}{I_0(2 \cdot m \cdot L)}, \tag{3.3}$$

where $I_1(2mL)$ and $I_0(2mL)$ are modified first-order and zero-order Bessel functions, respectively, of the first kind [23]. With the fin efficiency calculated, the heat transfer rate of the fin can be calculated. To do so, the maximum heat transfer rate of the fin, Q_{maxfin}, is then calculated based on Eq. 2.2, given by

$$Q_{maxfin} = h \cdot A_f \cdot \theta_b, \tag{3.4}$$

where θ_b is the difference between the base temperature of the heat sink and the ambient temperature. For this application, the base temperature of the heat sink is conservatively assumed to reach 110 °C and the ambient temperature is assumed to be 25 °C. Equations 3.3 and 3.4 are then combined to calculate the actual individual fin heat transfer rate, Q_f, given by

$$Q_f = Q_{maxfin} \cdot \eta_f. \tag{3.5}$$

The next step is to calculate the overall efficiency of the array of fins. To do so, the maximum heat transfer rate through the array and the overall fin efficiency are calculated. The maximum heat transfer rate of the array, $Q_{maxarray}$, is given by

$$Q_{maxarray} = h \cdot A_{total} \cdot \theta_b, \tag{3.6}$$

where A_{total} is the sum of the heat sink base area and the total fin area. Then, the overall surface efficiency of the array of fins, η_o, is calculated as given by

$$\eta_o = 1 - \frac{N_{fins} \cdot A_f}{A_{total}}(1 - \eta_f) \tag{3.7}$$

for a straight triangular fin [23]. The array for plotting the design space is then built by calculating the actual array heat transfer rate for the fins, the mass of the heat sink and the footprint area of the heat sink. The actual heat transfer of the array, Q_{tarray}, is calculated using Eq. 3.6 and Eq. 3.7 and is given by

$$Q_{tarray} = \eta_o \cdot Q_{maxarray}. \tag{3.8}$$

The mass of the heat sink is calculated using the density of the material and the sum of the volume of fins and base of heat sink. Finally, the footprint area of the heat sink, A_{HS}, is given by

$$A_{HS} = w \cdot S \cdot N_{fins}.$$

The design space study functions were iteratively solved for the parameters of interest until the limitations of the ElemX printer were met.

3.3 Phase Change Material Selection

The PCM was then selected based on the operating parameters of the application. Out of the various types of PCMs seen in Figure 2.3, two types of PCMs are evaluated in this study, organic compounds and low-melt fusible alloys (LMFAs) based on non-toxicity, availability and melting point. Three organic compound PCMs were considered: paraffin wax, palmitic acid and stearic acid (SA). Paraffin wax seems to be more commonly used that SA or palmitic acid and is likely because its availability as well as research previously completed that has incorporated composites of paraffin wax with other materials for increased thermal conductivity [31]. However, the desire to further apply the concept with a less commonly used PCM, paraffin wax was ruled out of consideration. Palmitic acid, though arguably appropriate for the lower powered CPU, did not have the desired melting point. Therefore, SA was the preferred organic compound and was purchased through SigmaAldrich at a quality of 95 % to minimize the effect of impurities on the thermophysical propertied of the material.

Two metal PCMs were also considered: Field's Metal (FM) and Wood's Metal. FM Contains 32.5% Bismuth (Bi), 51% Indium (In), 16.5% Tin (Sn) whereas Wood's Metal contains 50% Bi, 26.7% Lead (Pb), 13.3% Sn, 10% Cadmium (Cd). The presence of Cadmium makes Wood's Metal toxic and was eliminated from selection possibilities, FM, although non-toxic, did not meet the melting point requirement.

Therefore, SA was selected as the PCM.

Table 3.1 summarizes the comparison of PCMs considered.

Table 3.1. Comparison of PCMs. Adapted from [10], [32]–[36].

	PCM	Composition	Melting Temperature (°C)
Organic Compounds	Paraffin Waxes	C_nH_{2n+2}	-12 - 85
	Palmitic Acid	$CH_3(CH_2)_{14}COOH$	55
	Stearic Acid	$CH_3(CH_2)_{16}COOH$	69
LMFAs	Field's Metal	Bi, In, Sn	62
	Wood's Metal	Bi, Pb, Sn, Cd	62

3.4 SA/Al-4008 Material Testing and Compatibility

With the PCM and AM method selected, the cyclability of SA and compatibility of the SA in an Al-4008 heat sink had to be studied. Previous research into the cyclability of SA and interaction of SA with Al-4008 provided data for understanding of the materials used within the study. A NETZSCH Instruments STA 449 F3 Jupiter was used for differential scanning calorimetry (DSC) to characterize SA by determining peak transition temperatures and heat flows of its melting and solidification transformations [37]. DSC worked by adding a small sample of the SA into a crucible that was accompanied by an identical, but empty, crucible in the DSC. Heating a cooling cycles were then applied to the crucibles, measuring the amount of heat required to heat the crucibles to the specified temperatures. The crucibles were cylced between 40 °C and 80 °C with heat flows ranging between 0.6 µW/mg and -0.6 µW/mg over 50 cycles. A thermogravimetric analysis (TGA) recording also measured weight changes during the cycles. A FEI Inspect f50 SEM was used to observe microscopic material interactions, including phase segregation, corrosion and pore size changes after 0, 25, and 50 cycles. 10 kV were applied to produce images at 5 µm for each set of cycles.

3.5 Printing and Filling Hollow Parts

3.5.1 Printing Hollow Parts

To generate the heat sink, the process for printing hollow parts had to be developed. Hollow parts of unique shapes were produced without the need for printed supports using a two-step process. For each hollow part, a heat sink model was designed with empty space for a “lid” and the corresponding lid was designed as a separate part. This was necessary due to the overhang caused by the required geometry to print an empty volume within the part [7]. Figure 3.3 shows a cutout side view of the wrapped design, where the blue shaded region is the designed space for the lid. Figure 3.4 shows the SolidWorks model of the lid (bottom view). The lid has a square hole in the center so it does not interfere with the primary heat sink geometry in the center and, can instead, be placed flush on top. To ensure contact and a tight fit, a chamfer design was created for the heat sink to lid interface, which can be seen in both figures.

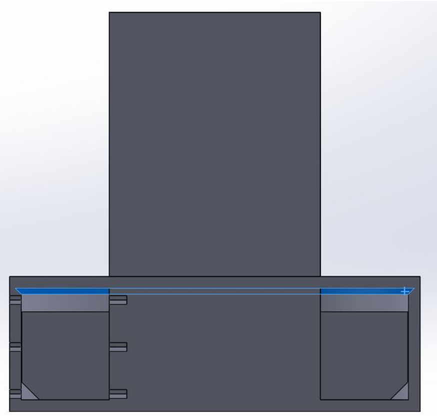

Figure 3.3. Section view (side): reservoir design

.

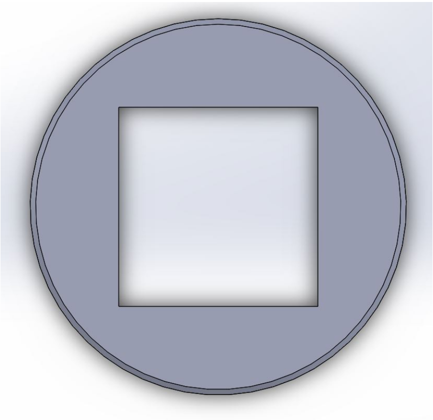

Figure 3.4. Bottom view: lid

.

First, the lid was printed then removed from the bed plate as shown in Figure 3.5.

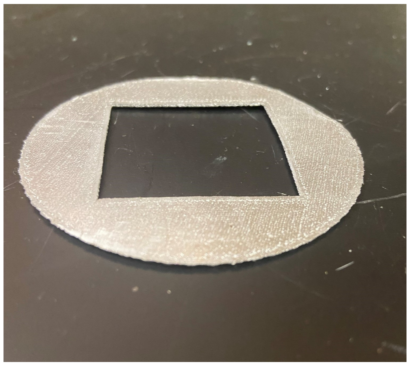

Figure 3.5. Printed lid for reservoir design following removal from bed plate and quenching.

Then, the base part was printed up to the layer corresponding to the designed lid location in the heat sink. Once this layer was reached, the print process was "paused" so that the print head would move out of the way of the part and the lid could be placed on top.

Figure 3.6 shows the part in the center of the bed plate. The lid can be seen on the bottom left as it is being pre-heated in preparation for installation so that expansion of the part may occur to ensure a flush fit with the heat sink during the print process. Figure 3.7 shows the heat sink during the print process following the installation of the lid. Note that the internal fins are no longer visible at this point in the process.

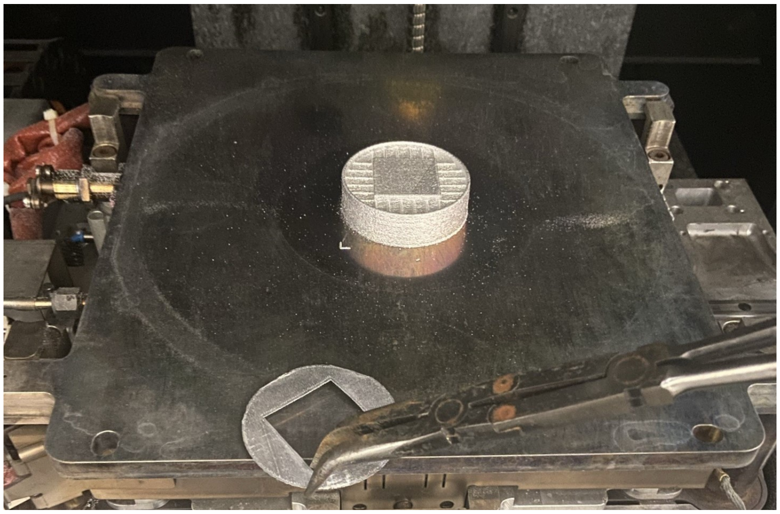

Figure 3.6. Pre-heating the lid (bottom left) prior to installation on the heat sink during printing.

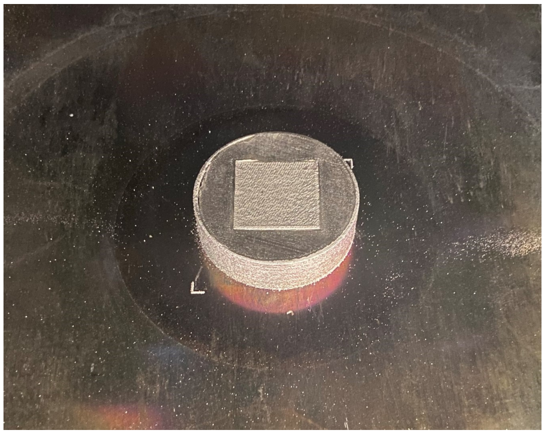

Figure 3.7. Top view of heat sink during printing with lid installed.

Once the lid was in place, the print was resumed and the layers printed above the lid effectively welded the lid onto the heat sink, as seen in Figure 3.7, while leaving the hollow area free of droplets and material.

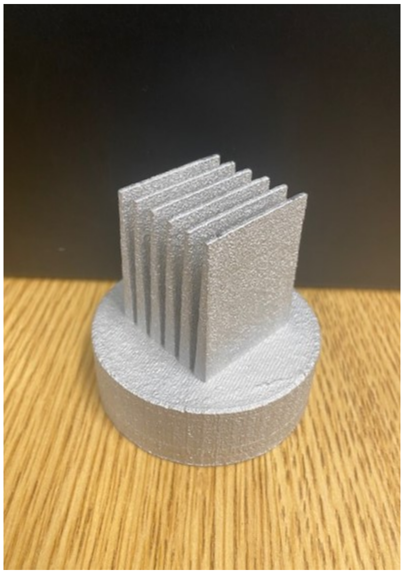

Figure 3.8. Printed heat sink.

The heat sink was removed from the bed plate using a quenching process to thermally shock the base plate and remove the part. The base plate was then reinstalled into the printer. Given the printer was not shutdown, operated for a long period of time (greater than approximately six hours based on print-quality degradation concerns), and sufficient argon flow remained for follow-on printing, the part could be printed again once the bed plate returned to within the operating temperature range. All files required for successive prints were saved onto the printer operating system for quick reproduction of heat sinks for testing.

3.5.2 Filling a Hollow Part with SA

Once created, post manufacturing and a proven filling process was required to fill the part. First, holes were drilled to for the thermocouple locations. Holes for filling the SA were also drilled, then tapped for screwing the barbs and set screws into the heat sink. Tygon tubing was attached to the barbs in preparation for SA filling. The SA was placed in a beaker then melted using a design similar to a double boiler by partially submerging the beaker in heated water. Once the SA was melted, a hand vacuum pump was used to draw a vacuum and pull the SA through the tubing and through the part. The excess tubing was wrapped around the warm bowl of water to ensure the SA remained a liquid as it travelled through the tubing. When the fill holes were on the side, the part was placed on a tilted stand to ensure all air escaped. With the exception of the final wrapped design, all parts used for various tests had fill holes designed on the sides. Thus, an example of one of the earlier prototype designs was used to show the filling process. Once SA was observed downstream of the part, the filling process was over and set screws were used to prevent draining of the SA. Figure 3.9 shows the labeled primary components of the filling process.

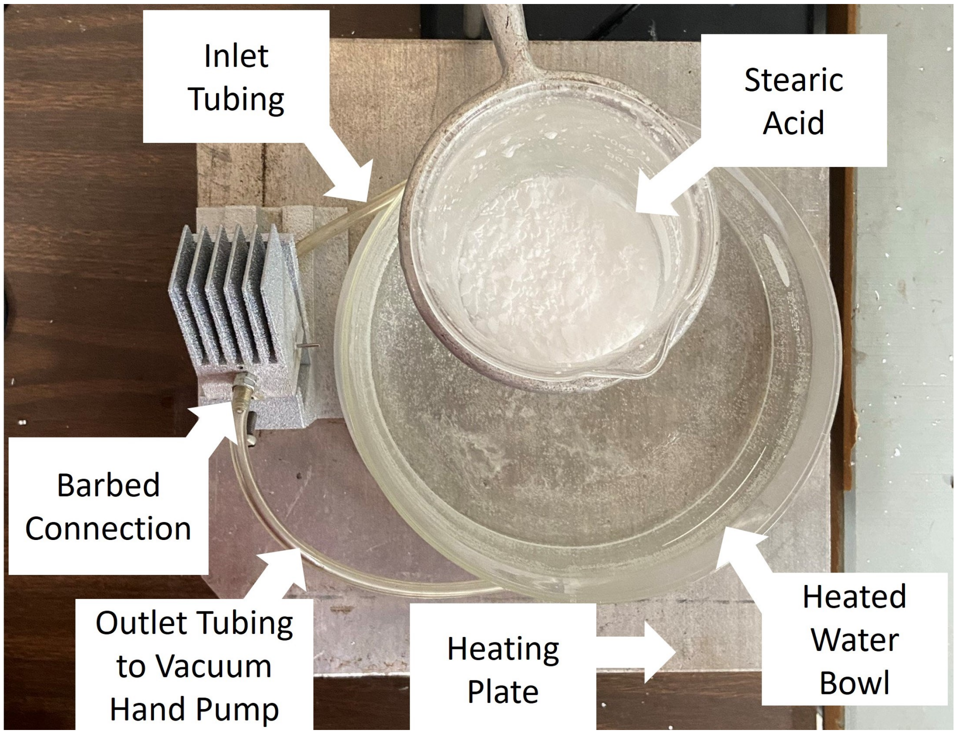

Figure 3.9. Top view of process for filling SA into heat sink.

3.5.3 Stearic Acid Density Testing

Once filled, the stearic acid behavior during heat-up needed to be understood. Since limited published density data was available, a density test was developed. The density information was also required for ANSYS simulations and to accurately measure the SA required to fill a container. The mass and volume of SA was required to determine the density [22]. The density, ρ, is given by

$$\rho = \frac{m}{V},$$

where m is the mass and V is the volume. 0.8 g of SA were added to a graduated cylinder with 0.2 ml precision. A thermocouple attached to a digital display data acquisition unit was used to accurately measure the temperature during the test. The graduated cylinder was heated to melt the SA, as shown in Figure 3.10.

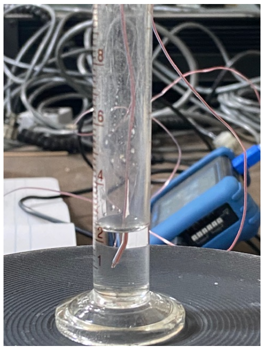

Figure 3.10. SA density test with thermocouple in liquid SA and digital data acquisition system in background.

The volume in the graduated cylinder was read at various temperatures and the density was calculated at each temperature using the measured mass of the SA and the observed volume.

3.5.4 Sealing Stearic Acid

Sealant tests were completed to determine the behavior of the SA inside the metal and ensure no leakage occured as the SA expanded during heat-up. To do this, a hollow metal box was printed and holes were drilled for thermocouple connections. Two thermocouples were connected on the left side and one was connected on the top, as seen in Figure 3.11. The box was then filled with SA in accordance with Section 3.5.1 and Section 3.5.2. Then, the part was heated to 80 °C. An air-temperature curable stainless steel coating was used to seal the SA in the container. The coating applied as a yellow-tinted liquid coating, as seen on the top of the container around the thermocouple in Figure 3.12.

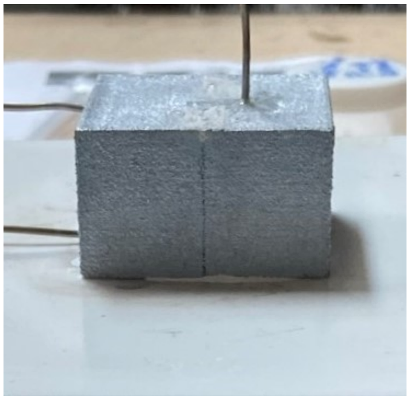

Figure 3.11. SA-filled box.

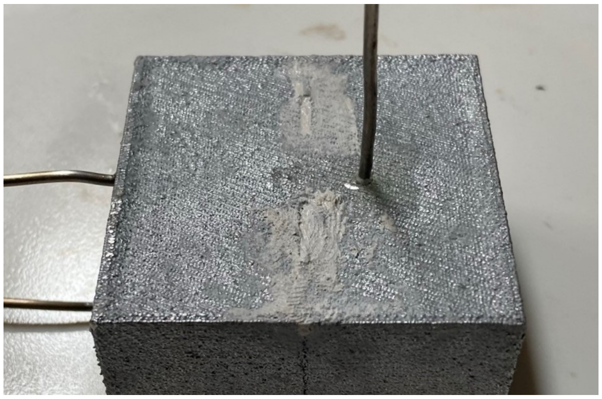

Figure 3.12. Yellow-tinted sealant.

3.6 Thermal Conductivity Test

The effect of adding SA into Al-4008 on overall thermal conductivity needed to be understood so a one-dimensional thermal conductivity test was developed using a vertical alignment of test pieces and insulation. The test was comprised of three cylinders stacked vertically, as shown in Figure 3.13 and Figure 3.14. Figure 3.13 shows the associated thermocouple holes, with labeled locations (i.e., TC1) as applicable to data collection during the test. The smaller holes at the top and bottom of the cylinders were used for thermocouple placement. The top and bottom cylinders were solid Al-4008 reference "pucks." The middle cylinder was filled with SA. The set screw toward the top of the middle cylinder was installed to seal the fill hole, which was used to fill the cylinder with SA. The walls of the middle cylinder were 3 mm thick to minimize the amount of Al required to hold the SA. The minimum wall thickness was based on the printing limitations of the ElemX printer [7].

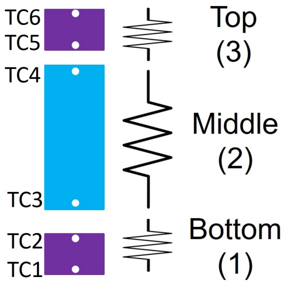

Figure 3.13. Schematic.

Figure 3.14. Vertically stacked cylinders.

To reduce surface roughness, the top and bottom surfaces of the cylinders were polished in accordance with Figure 3.15 [8]. The steps of the process were completed with water flowing over the polishing surface. Silicon carbide of various grits and time of polish at 100 revolutions per minute (RPM) and 5 pounds of pressure were used to flatten the surface of the contact surfaces. The first step involved polishing with a P1000 silicon carbide disk for a time of 10 minutes followed by sequential polishing steps using P1500, P2500, and P4000 silicon carbide disks with polishing times of 15, 20, and 30 minutes, respectively. A Buehler Ecomet 4 variable speed polisher with an Automet 2 Power Head was used for polishing.

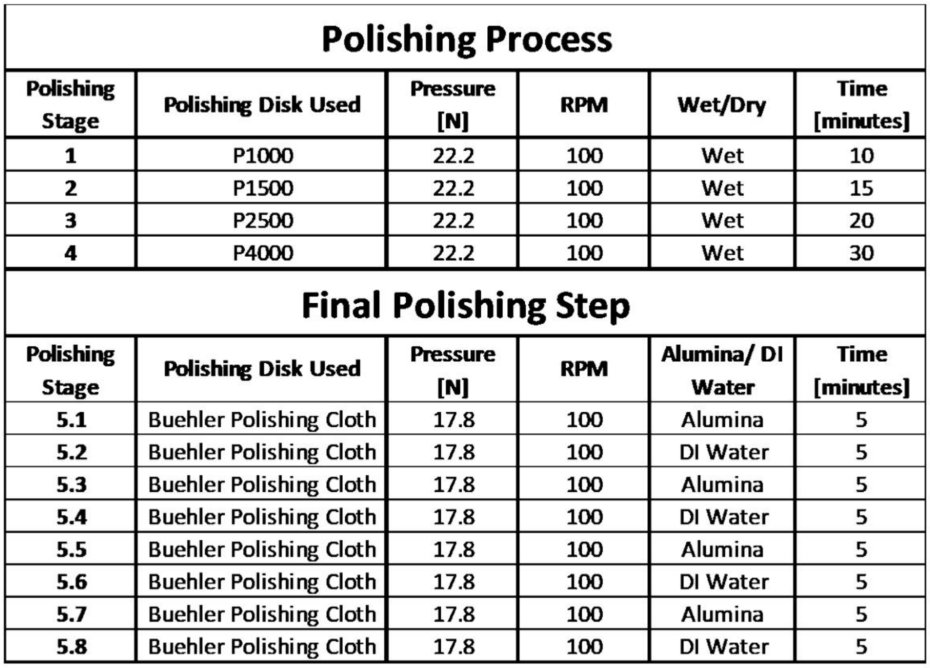

Polishing Process

Polishing Stage	Polishing Disk Used	Pressure [N]	RPM	Wet/Dry	Time [minutes]
1	P1000	22.2	100	Wet	10
2	P1500	22.2	100	Wet	15
3	P2500	22.2	100	Wet	20
4	P4000	22.2	100	Wet	30

Final Polishing Step

Polishing Stage	Polishing Disk Used	Pressure [N]	RPM	Alumina/ DI Water	Time [minutes]
5.1	Buehler Polishing Cloth	17.8	100	Alumina	5
5.2	Buehler Polishing Cloth	17.8	100	DI Water	5
5.3	Buehler Polishing Cloth	17.8	100	Alumina	5
5.4	Buehler Polishing Cloth	17.8	100	DI Water	5
5.5	Buehler Polishing Cloth	17.8	100	Alumina	5
5.6	Buehler Polishing Cloth	17.8	100	DI Water	5
5.7	Buehler Polishing Cloth	17.8	100	Alumina	5
5.8	Buehler Polishing Cloth	17.8	100	DI Water	5

Figure 3.15. Polishing procedure used on the contacting surfaces of the thermal conductivity test cylinders and components. Source: [8].

A mirror finish was not required nor desired during the polishing. Accordingly, the procedure in Figure 3.15 was modified to exclude steps 5.1-5.8. Instead, to ensure complete surface area contact, thermal paste was used as the IHS on the top and bottoms of the cylinders, as shown in Figure 3.16.

Figure 3.16. Assembling the cylinders and components for the thermal conductivity test, including the application of thermal paste on surfaces.

Two thermocouples were inserted into small holes in the sides of each puck and the SA-filled cylinder. Two blocks of "Super Firetemp S" high temperature insulation were bored out and mated to encase the cylinders. Small slots were carved into the insulation to allow space for the thermocouple extrusions. Finally, the top was closed from the atmosphere by a heavy Al-4008 weight, which also ensured adequate contact pressure during the test. The weight was also used as a heat sink following testing via forced circulation of a small computer fan through its fins. Figures 3.17 and 3.18 show the complete exploded and assembled view, respectively, of the thermal conductivity test rig.

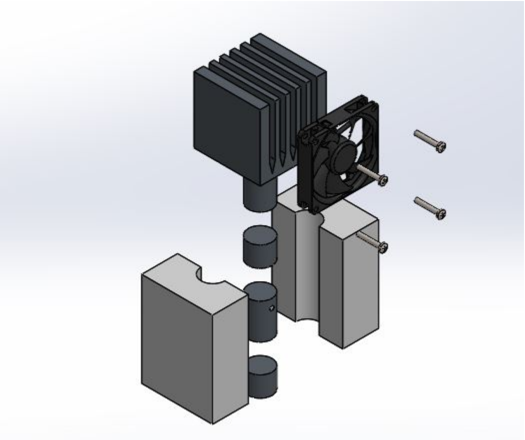
Figure 3.17. Exploded view. Source: [38].

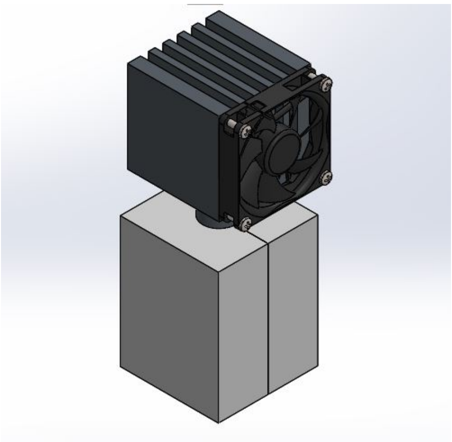
Figure 3.18. Assembled view. Source: [38].

Once the test rig was assembled, the insulation pieces were pressed together using a bolted frame, as shown in Figure 3.19, and placed on an IKA C-MAG HS-7 hot plate. The rig was initially cycled with various temperatures to determine the required hot plate surface temperature for the SA-filled middle cylinder to reach within the range of the CPU application. These hot plate temperatures ranged from 65 °C to 125 °C. 85 °C was determined to be the optimal temperature. Therefore, the surface of the hot plate was heated to approximately 85 °C prior to placing the rig on the hot plate. This allowed for fast heating of the cylinder assembly, reducing time required to reach quasi-steady state conditions. Quasi steady state conditions were considered reached when there was less that 1 °C temperature change over the course of 2 minutes.

Figure 3.19. Full assembly of thermal conductivity test rig.

The insulation surrounding the cylinders created adiabatic conditions, rendering the rate of heat transfer in the radial directions negligible. Nominal and measured values of the test cylinders were noted, as shown in Table 3.2. The "Diameter" measurements were with respect to the cylinder contact surface diameters whereas the "Length" measurements were the distance between thermocouples for each cylinder.

Table 3.2. Thermal conductivity test nominal and measured values for applicable cylinder dimension.

Dimension	Nominal Value	Measured Value
Top Reference Puck Length (mm)	15	15.88
Middle Cylinder Length (mm)	45	44.80
Bottom Reference Puck Length (mm)	15	14.85
Top Reference Puck Diameter (mm)	25	25.18
Middle Cylinder Diameter (mm)	25	24.90
Bottom Reference Puck Diameter (mm)	25	25.15

The discrepancies in distances between nominal and measured values were due to slight inconsistencies in the post-manufacturing process. The discrepancies in measurements between the cylinder diameters were due to surface imperfections resulting from a combination of the AM and polishing processes.

The average rate of heat transfer, q_{ave}, was calculated using the rate of heat transfer through the top and bottom reference pucks, as given by

$$q_{ave} = \frac{q_1 + q_3}{2}. \tag{3.9}$$

The average rate of of heat transfer through the reference pucks was then used to solve for the thermal conductivity of each cylinder, k_i, as given by

$$k_i = \frac{q_{ave} \Delta x_i}{A_i \Delta T_i}, \tag{3.10}$$

where ΔT_i is the difference in temperature across the thermocouples, Δx_i is the measured distance between thermocouples, and A_i is the cross-sectional area of the contact surfaces between cylinders based on the measured diameters. The subscripts in each equation correspond to the cylinders assigned in Table 3.3.

Table 3.3. Thermal conductivity test subscript designations corresponding to Eq. 3.10.

Subscript (i)	Cylinder
1	bottom
2	middle
3	top

Once quasi steady state temperatures were reached, the data was processed using MATLAB. The code is shown in Appendix B.

3.7 Heat Sink Design Selection

3.7.1 Heat Sink Design Strategies

Four conceptual designs were initially considered as a possible heat sink:

1. Store the SA in a hollow section located in the center of the heat sink.
2. Use external reservoirs to store the SA to draw and maintain the heat from the CPU.
3. Incorporate SA within the heat sink material during printing vice physically separating the SA and metal.
4. Exploit natural circulation of SA within the fins.

Based on the temperatures required to print the metal covered in Section 3.2.1, the SA could not be incorporated into the metal during the print process since it would flash to vapor. Thus, the third design was not possible for this application. The fourth conceptual design required further experimentation and testing to determine practicality of the natural circulation capability and was ultimately shifted to another phase of the research.

Therefore, only two out of the four designs were selected for further testing. Once contained SA in the center of the hollow heat sink and the other contained SA in external reservoirs (connected to the heat sink).

3.7.2 ANSYS Transient Thermal Simulations

With material behavior, compatibility and interaction understood, along with possible design concepts considered, the focus of the design development shifted toward a geometry focus. Based on the two designs selected for further-on testing from Section 3.7.1, transient thermal simulations were built and run using ANSYS 2022 R1 software to determine their relative thermal management ability to one another. For efficiency and simplicity of analysis, especially given this test was to determine the best design in a relative sense, a 2D analysis was performed. The surfaces were built using the SpaceClaim CAD software built into ANSYS. In each design, with the exception of the solid (no SA) control design, equal amount of SA was incorporated into the simulation based on the area of the 2D surface.

Figure 3.22 shows the "solid control" design for generation of a baseline set of comparative data to the simulation results. The control was not used for simulations. Rather, it was an abstraction of a model without SA.

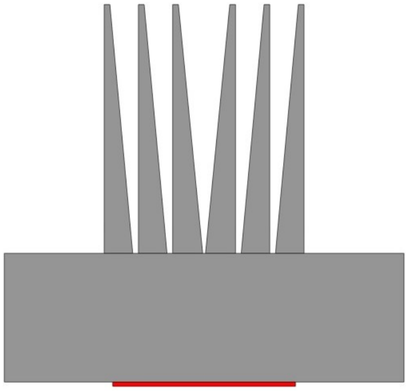

Figure 3.20. SpaceClaim surface of solid heat sink for 2D ANSYS transient thermal simulation.

Figure 3.21 is the bulk design model. Figure 3.22 is the reservoir design model. The gray areas are printed Al-4008, the beige areas are SA and the red area is the heating element. Placing the SA on the sides is conceptually equivalent to a design with SA located in reservoirs, as described in Section 3.7.1. Of note, the heating element is about 0.05 mm thick in the simulations instead of the larger 0.75 mm shown so that heat flow is directed only into the conceptual designs instead of the heating element as well.

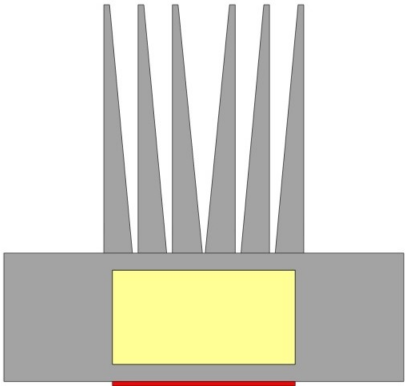

Figure 3.21. SpaceClaim: bulk design.

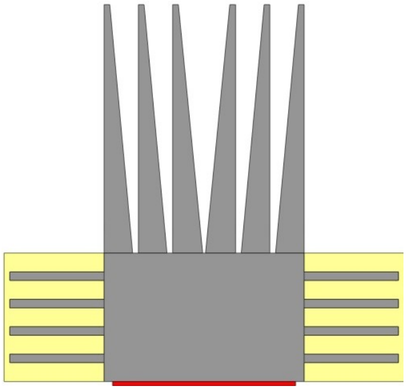

Figure 3.22. SpaceClaim: reservoir design.

To complete this simulation, the parameters in Table 3.4 were inputted into the program for solving in accordance with the ANSYS phase change material workshop [39].

Table 3.4. ANSYS transient thermal parameter for 2D simulations. Adapted from [39].

Step 1 Parameter	Value	Step 2 Parameter	Value
2D Behavior	Plane Stress	2D Behavior	Plane Stress
Stop End Time	0.1	Stop End Time	600
Auto Time Stepping	ON	Auto Time Stepping	ON
Define By	Time	Define By	Time
Carry Over Time Step	N/A	Carry Over Time Step	Off
Initial Time Step	1E-3	Initial Time Step	1E-3
Min. Time Step	1E-3	Min. Time Step	1E-4
Max. Time Step	0.1	Max. Time Step	5
Time Integration	On	Time Integration	On
Line Search	Off	Line Search	On
Nonlinear Formulation	Full	Nonlinear Formulation	Full

The heat flow was selected to 100 W as a conservatively large parameter to show an appreciable result within the simulation. The geometrical feature incorporating the heat flow boundary condition was the interface edge between the heater and bottom of the Al body. Since the simulation was based on a passive heat sink without any aid from forced circulation, conservatively there was no convection boundary condition set. The initial temperature of the surface was set to 65 °C, just below the melting point temperature of SA. Thermal stability was also conservatively ensured by setting the thermal stability correction factor, Theta, to 0.5 [39]. The number of iterations was limited to 1000 to allow sufficient iterations for convergence.

To properly capture the phase change behavior, enthalpy (H) and thermal conductivity (k) over a defined temperature range had to be entered into the "Engineering Data" section of the ANSYS Workbench Project. Enthalpy was calculated using the temperature ranges and equations in Table 3.5.

Table 3.5. Temperature ranges and enthalpy equations for ANSYS simulations.

Temperatures °C	Applicable Equation
0	$\left(\frac{H}{V}\right)_0 = 0$
0 to 68	$\left(\frac{H}{V}\right)_1 = (\frac{H}{V})_0 + \rho_{solid} C_{p,solid} \Delta T_{0-1}$
68 to 68.1	$\left(\frac{H}{V}\right)_2 = (\frac{H}{V})_1 + \rho_{70C} \Delta H_{fusion}$
68.1 to 200	$\left(\frac{H}{V}\right)_3 = (\frac{H}{V})_2 + \rho_{liquid,ave}(1.30) C_{p,solid} \Delta T_{2-3}$

The subscripts 0, 1, 2 and 3 correspond to temperatures 0 °C, 68 °C, 68.1 °C and 200 °C, respectively. 68 °C was the anticipated onset of melting based on the average SA melting point of 69 °C. The final temperature of 200 °C was assumed based on anticipated final temperatures over the battery of simulations performed. For the stored energy, the assumed volume was 1 mm^3 for simplicity of calculations and consistency of units. The densities used in the equations of Table 3.5 were based on the density test results found in Table 4.1. For the liquid region, the average density was used. The specific heat capacity (C_p) was determined by dividing the molar specific heat capacity of the solid (501 J/molK) by the molecular weight of SA (284 g/mol) [40], resulting in a specific heat of 1766 J/kgK. Since the specific heat capacity of the liquid region was unknown for the various temperatures, a 30 % increase was assumed, which is indicated by the “1.30” in the last row of Table 3.5. The enthalpy of fusion was determined by using its value in molar form (63.2 KJ/mol) and dividing it my the molecular weight of SA, similar to the specific heat capacity [41].

Figure 3.23 shows calculated outputs based on the associated inputs for enthalpy. The region in Figure 3.23 corresponding to the temperature range of 68 °C to 68.1 °C is approximately vertical and represents the latent heat of fusion energy absorption.

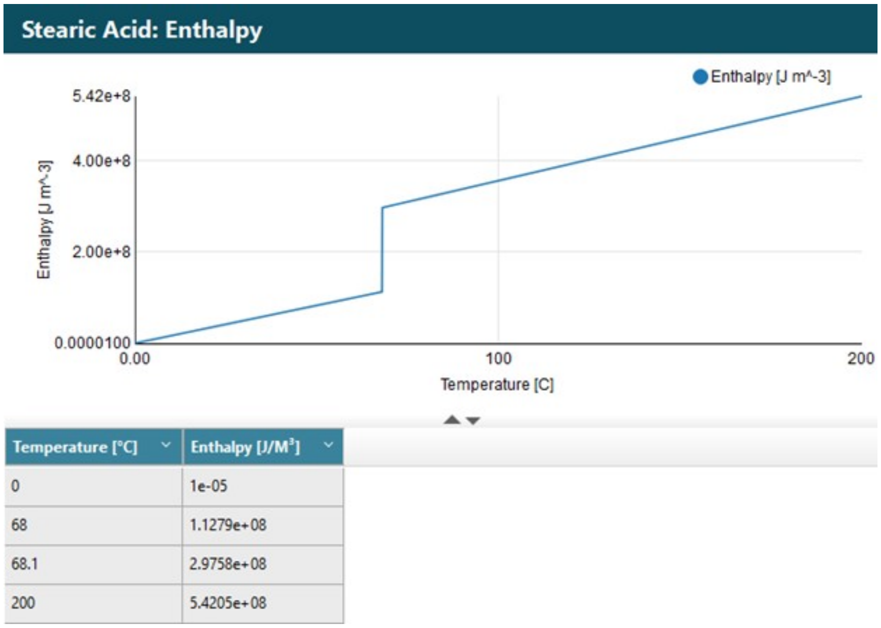

Temperature [°C]	Enthalpy [J/M^3]
0	1e-05
68	1.1279e+08
68.1	2.9758e+08
200	5.4205e+08

Figure 3.23. SA enthalpy and temperature inputs, with graph, for ANSYS simulation.

Thermal conductivity of pure SA was derived from known reference-based values. Figure 3.24 shows the SA thermal conductivity and temperature inputs, with a graph, for the ANSYS simulations.

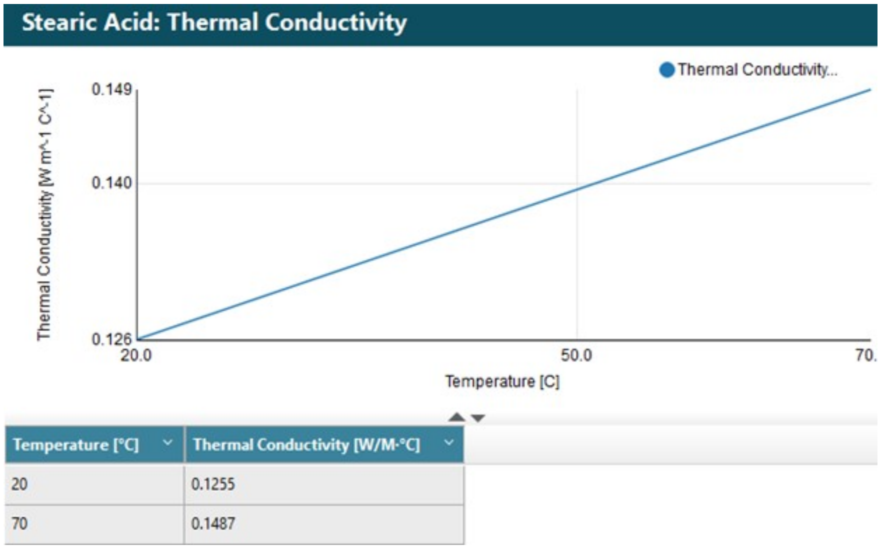

Temperature [°C]	Thermal Conductivity [W/M·°C]
20	0.1255
70	0.1487

Figure 3.24. SA thermal conductivity and temperature inputs, with graph, for ANSYS simulation.

Each mesh was selected to be quadrilateral dominant based on the relatively simple shapes of the models. Element order was set to quadratic and element size was set to 5E-3 for each simulation. Graphics of the meshes are shown in Figure 3.25 and Figure 3.26.

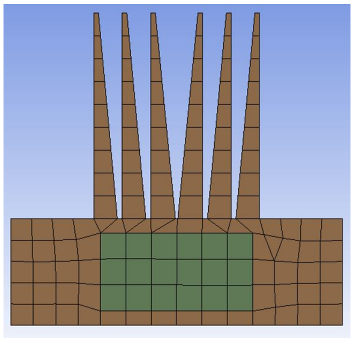
Figure 3.25. Mesh for SA bulk design.

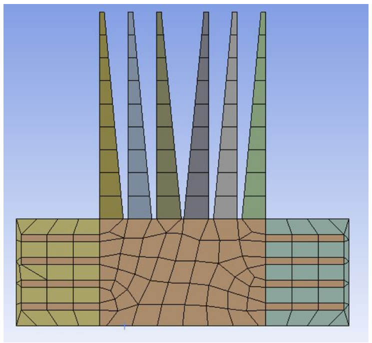
Figure 3.26. Mesh for SA reservoir design.

3.7.3 Heat Sink Vessel Design Considerations

The heat sink vessel design was selected based on the ANSYS simulations of Section 3.7.2. With the geometry selected, the volume available for SA needed to equal or exceed the amount of SA required to absorb the heat load. To calculate the required amount of thermal energy required to be absorbed, the heat flow and time period had to be determined. Consistent with the ANSYS simulations and a conservative overestimate for a higher power CPU, 100 W was chosen as the heat transfer rate. Based on the application, a time period of 30 seconds was selected for a program requiring a high amount of processing power over a short amount of time, such as a short simulation. This yielded a result of 3000 J. Assuming conservation of energy, no work done on the system, negligible mass transfer out of the system and only one initial mass component, the mass, m, was calculated given by

$$m = \frac{\mathbf{Q}}{h_f},$$

where **Q** is the heat energy supplied to the system and h_f is the enthalpy of fusion. The enthalpy of fusion was determined to be 203.83 kJ/kg based on a previous study [42]. This was a conservative assumption based on the highest value from Chapter 2 for SA and provided a higher bound estimate for the required mass. The required mass was calculated to be 14.72 g given the previously calculated heat transfer rate. Using the calculated mass of 14.72 g and previously calculated density per Table 4.1 to be 0.8318 g/cm^3, the required volume was determined to be 17.69 g/cm^3.

3.8 Experimental Testing

3.8.1 Power Cycles Test Rig Setup

At this point, material properties and interactions for the PCM and heat sink container material were understood and the heat sink geometry was selected based on simulations, application-modeled experimental testing was ready to commence. The printed reservoir design was filled with SA and assembled into the test rig. The heat sink was placed on a heat duct that resolved the variation in heat source (resistance heaters) contact area and the measured contact area of the application CPU. The heat duct was placed on four resistance heaters rated to 120 volts (V). The resistance heaters were embedded into insulation to establish adiabatic conditions on the sides and bottoms of the heaters, minimizing multi-directional heat loss. Figure 3.27 shows the resistance heaters embedded in insulation. Figure 3.28 shows the heat duct on top of the resistance heaters.

Figure 3.27. Resistance heaters in insulation.

Figure 3.28. Heat duct.

The heaters were connected in parallel to a programmable power supply, whose voltage was controlled by a LABVIEW program. Current was regulated by the programmable power supply. To ensure positive contact with all heating and cooling surfaces, along with equal contact pressure for each iteration and design, a cage was built consisting of 4 bolts and two aluminum frames to clamp the rig together. Thermal paste was used between all contact surfaces as an integrated heat spreader. Figure 3.29 shows the fully assembled rig with the cage securing the heat sink in place.

Figure 3.29. Power cycles test rig fully assembled.

Data was collected from the thermocouples at 6 different locations:

- One to measure ambient temperature.
- One to measure temperature at the resistance heaters (simulating the CPU).
- Three to measure the temperature within the base of the heat sink, each equidistant from each other in a vertical pattern.
- One to measure temperature at the top of one of the fins.

A side view of the rig showing the thermocouple connections to the heat sink is shown in Figure 3.30. Table 3.6 provides the associated label locations for the associated labels shown in Figure 3.30. The thermocouple at the heat pad is the thermocouple of interest for this study.

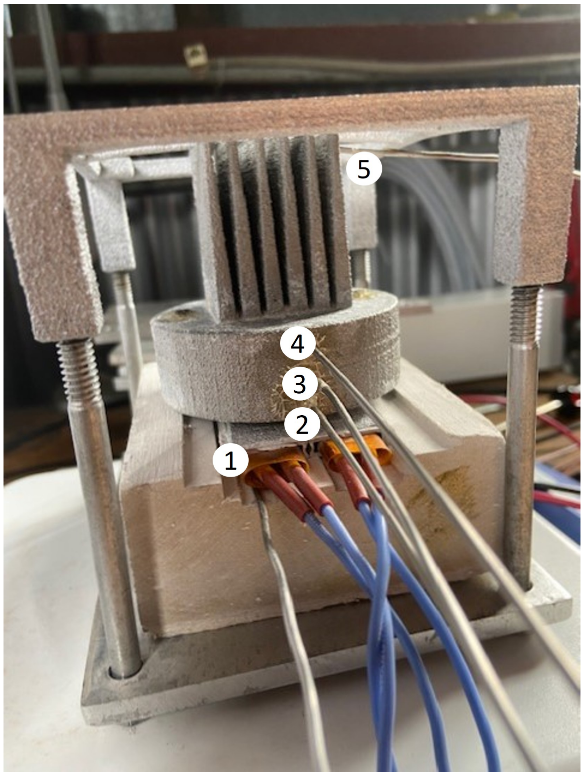

Figure 3.30. Side view of test rig showing thermocouple locations.

Table 3.6. Power cycle tests thermocouple locations.

Thermocouple	Location
1	Heat Pad
2	Below SA (in metal)
3	Within SA
4	Above SA (in metal)
5	Fin

Output power of the resistance heaters was verified to be within the range of the application specification identified in Section 3.1, and was adjusted based on the power cycles, as described in Section 3.8.2.

The data was collected using a data acquisition system, as shown in Figure 3.31. The yellow K-Type thermocouple is shown connected to the slot. Since a National Instruments (NI) RMX-4101 programmable power supply was used, the software selected to control the power supply within the NI LabVIEW 2022 Q3 program was NI-DAQmx. This was based on the user manual of the power supply and the compatibility of the NI products. For interfacing, the thermocouples were placed into the TC0 through TC5 positions within the NI PXIe-8381 slot, which was connected to the NI PXIe-1082 chassis.

Figure 3.31. Data acquisition system with power turned off.

Appendix D shows the front panel interface of the LABVIEW program used to control the programmable power supply and collect data during the study. Appendix E shows the back panel code of the LABVIEW program used to control the programmable power supply and collect data during the study.

3.8.2 Power Cycles

Short Duty Cycle, Long Test Duration

The first set of power cycles was determined based on a user that requires operation of the CPU at both low and high powers over a short period of time. Power was supplied two sets of two resistance heaters, each connected in parallel. To maintain within the application range while achieving a phase change, 8.25 V and 10 V were used to achieve powers of approximately 35 W and 50 W, respectively. These voltages were determined by trial and error to best understand the resistance heater behavior and output. The duty cycle was assumed to be 30 seconds of power-on followed by 30 seconds of power-off. This was repeated for a total time period of one hour for the 10 V setting and almost three hours for the 8.25 V setting.

Long Duty Cycle, Short Test Duration

A longer duty cycle was also desired to achieve the "shark fin" shape discussed in Section 2.1. To achieve this, a constant power of approximately 40 W was supplied to the resistance heaters until the thermocouple in the SA read 73 °C. This temperature was chosen based on the previously observed onset of SA melting. Once at that temperature, the cycles began. 9 V (40 W) was supplied over 100 seconds, 200 seconds and 300 seconds duty cycles, where each time increment was the half period of the each cycle. This voltage was also determined by trial and error and corresponded to approximately 40 W of power supplied to the heaters. Since these were longer duty cycles and phase change occurred in each, three iterations were run for each. Each duty cycle began after reaching 73 °C as measured within the bulk of the SA. This metric was determined based on the results of the short duty cycle, long test duration power cycles tests.

Table 3.7 summarizes the correlations found between input voltage and power of the resistance heaters used throughout the testing.

Table 3.7. Input voltage vs. power comparison for power cycle testing.

Input Voltage (V)	Power (W)
8.25	35
9	40
10	50

3.8.3 Comparison of Heat Sink Mediums

To properly determine the relative advantage of the phase change process as a thermal management strategy, the tests of Section 3.8.2 needed to be repeated for heat sinks of similar geometry to the selected "reservoir" design, but with different mediums. Several options were considered, but the goal was to compare the design to a solid (Al-4008 filled) heat sink, a hollow (air-filled) heat sink and a liquid-filled heat sink that did not change phase over the duty cycle and applied power. The liquid mediums were effectively the control to test the effectiveness of the phase change as a thermal management strategy. The primary parameters of consideration were specific heat capacity and thermal conductivity. Table 3.8 shows the comparison of internal fluids.

Table 3.8. Internal fluid comparisons for power cycle testing. Adapted from [40], [41], [43]–[49]

Material	Specific Heat Capacity (J/kgC)	Thermal Conductivity (W/mk)	Melting Point (°C)
SA	1.60 - 2.83	0.14 - 0.29	69
Soybean Oil	1.67 - 2.53	0.17 - 0.19	-5.8
Glycerol	2.49	0.29	17

CHAPTER 4:
Results and Discussion

This chapter presents and analyzes the results from the methodology established in Chapter 3. The results of the design space study are used to ensure the printer can develop a heat sink of adequate dimensions and material properties for the application. STA and SEM results prove the cycling behavior of SA and its interaction with the printed Al-4008 material, respectively. The density test results show the change in density of SA following phase transition over a small temperature range, suggesting expansion during heat-up is to be expected. The density data is then used to create material properties for the 2D transient thermal ANSYS simulations. These simulations are then used to determine the better relative heat sink design, which is then designed and printed. The basis of the resulting final design is then described and shown, with a verification that its internal volume is sufficient to hold the required amount of SA to thermally manage the expected thermal load of the application. Finally, the results of the two sets of power cycles are presented, analyzed and summarized, affirming the test results meeting of the goals of the study.

4.1 Design Space Analysis

Figure 4.1 shows the results of the study. The length units of the study are presented in units of meters (m), but the results were converted to centimeters to provide a more tangible understanding of the size of the maximum heat sink that the printer can produce relative to the one developed for this application-based research. The study revealed that the ElemX allows for the creation of a testable heat sink with a mass of up to 0.9 kg and contact area of 840 cm^2 (29 cm x 29 cm) which will yield a power of about 4000 W through. This provided a heuristic to the other types of designs that could be made and gave an idea of how other applications could be studied using this printer.

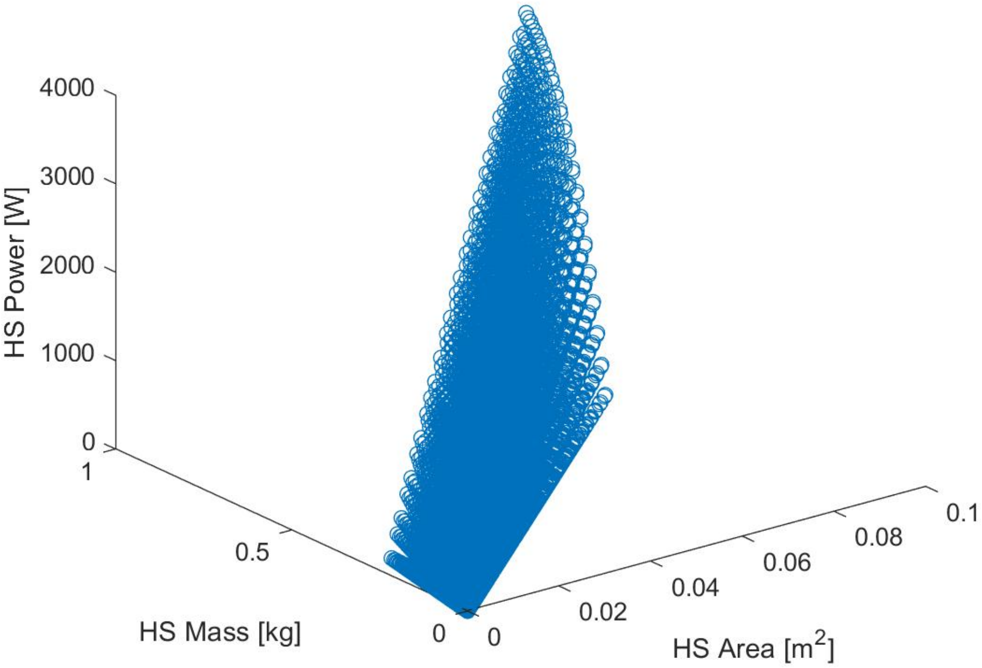

Figure 4.1. Design space study: power, mass and area.

Figure 4.2 shows the results for the heat sink mass (kg) vs. heat sink area (m^2). The red star is the plotted point of the mass and area for this research, corresponding to six fins and footprint area of 0.0078 m^2. It is clearly one of many options for heat sink designs. The footprint area and mass fall within a rectangular with a linear trending slop up until the mass limit of the ElemX.

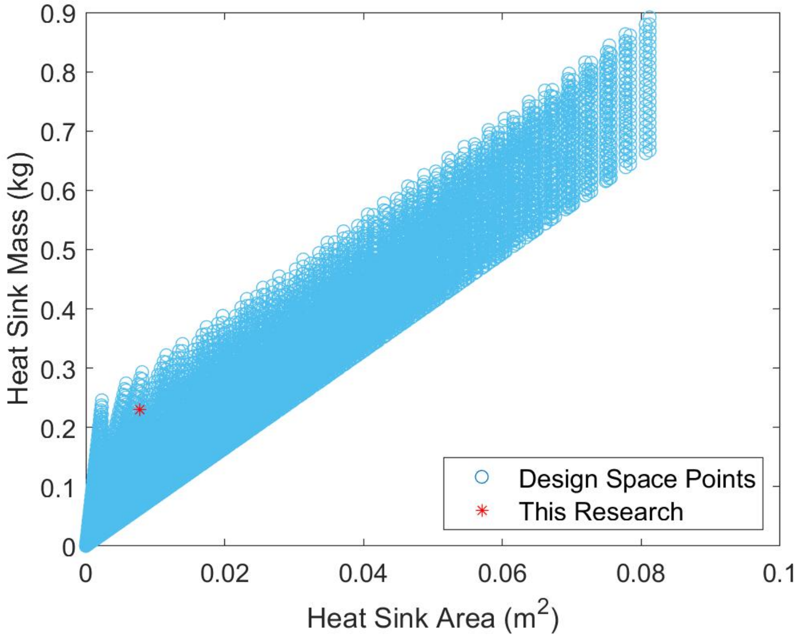

Figure 4.2. Design space study: heat sink mass (kg) vs. heat sink area (m^2).

Figure 4.3 shows the results for the heat sink power (W) vs. heat sink area (m^2). The red star is the plotted point of the power and area for this research, corresponding to a power of 50 W (the average power of the application power range) and footprint area of 0.0078 m^2. The power level is significantly lower than the capabilities of heat sinks designs possible with this printer. The design space branches linearly at various points, each of which are ultimately limited by a footprint area of approximately 0.08 m^2, corresponding to a power throughput of 4000 W.

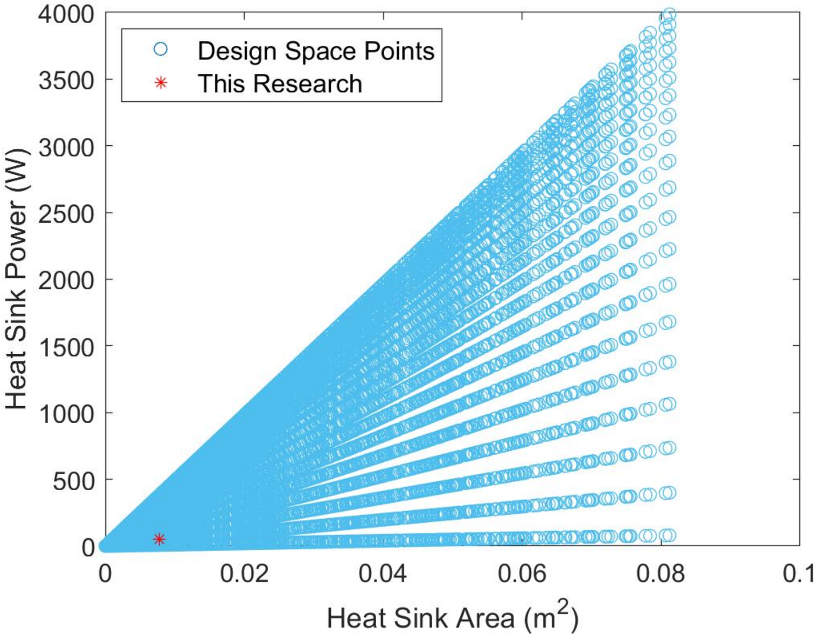

Figure 4.3. Design space study: heat sink power (W) vs. heat sink area (m^2).

Figure 4.4 shows the results for the heat sink power (W) vs. heat sink mass (kg). The red star is the plotted point of the power and mass for this research, corresponding to a power of 50 W (the average power of the application power range) and a heat sink mass of 0.23 kg. Though larger heat sinks could have been made for this study, the mass calculated was based on application dimensional constraints. Given the power range of the application, this design space study revealed that the maximum mass of the part that can be made it 0.67 kg. The maximum power throughput limit of 4000 W is limited by the ElemX mass limit of 0.9 kg.

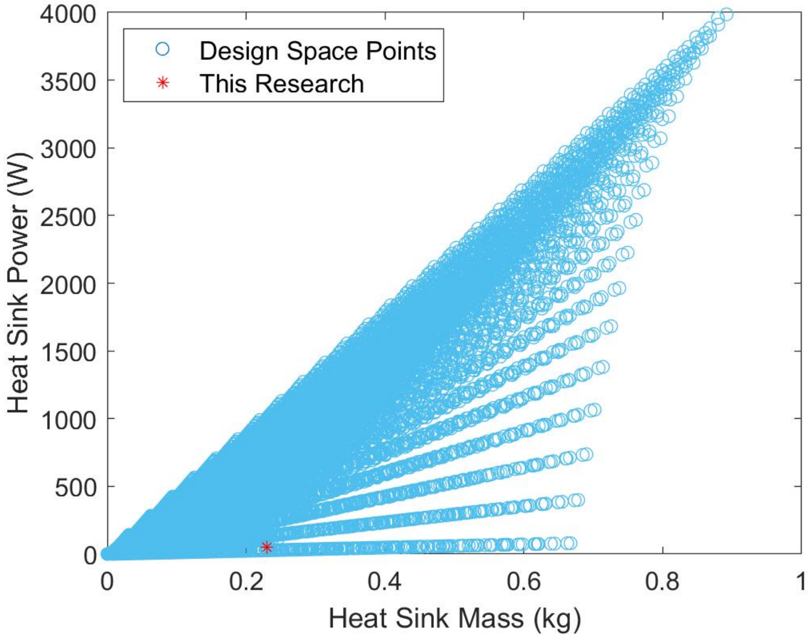

Figure 4.4. Design space study: heat sink power (W) vs. heat sink mass (kg).

Figure 4.5 shows the results for the number of fins vs. heat sink area (m^2). To fully understand the potential of the design space, it is imperative to recognize that the heat sink area is the footprint area. This is based on the ability, and the associated limitations, of printing various geometries with the ElemX. The red star is the plotted point of the power and mass for this research, corresponding to a 6 fins and a heat sink area of 0.0078 m^2. This is at the edge of the possibilities for the given number of fins. Should an increase in heat sink area be desired for a given application, the number of fins would have to be increased. Again, the ultimate limitation for this plot is the heat sink area of approximately 0.08 m^2, which corresponds to approximately 70 fins.

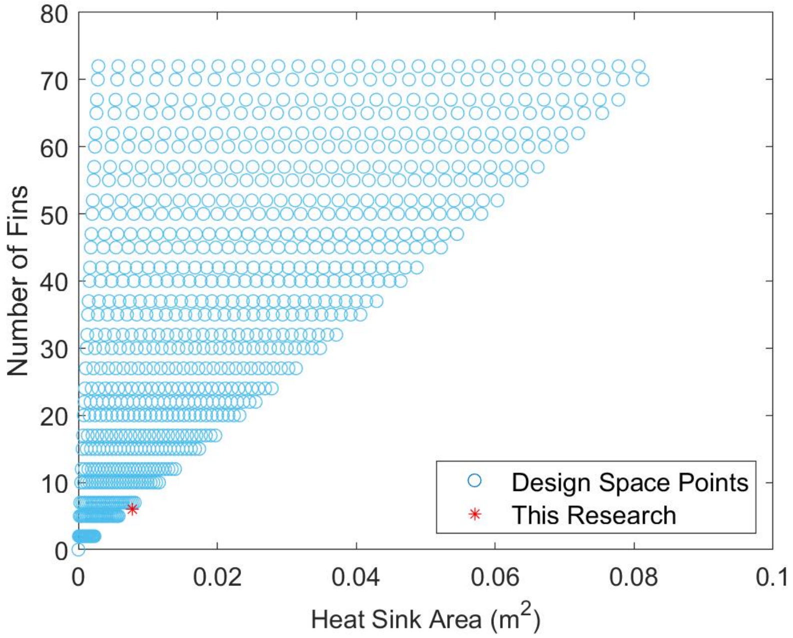

Figure 4.5. Design space study: number of fins vs. heat sink area (m^2).

4.2 STA Characterization and Material Interactions

The quality of the SA in the STA was 95 %. As shown in Figure 4.6, no byproducts formed after 50 cycles of analysis and there was no considerable effect on pore size. Phase segregation was noted before and after analysis, showing that SA was relatively stable with minimal material interaction in an Al-4008 filament.

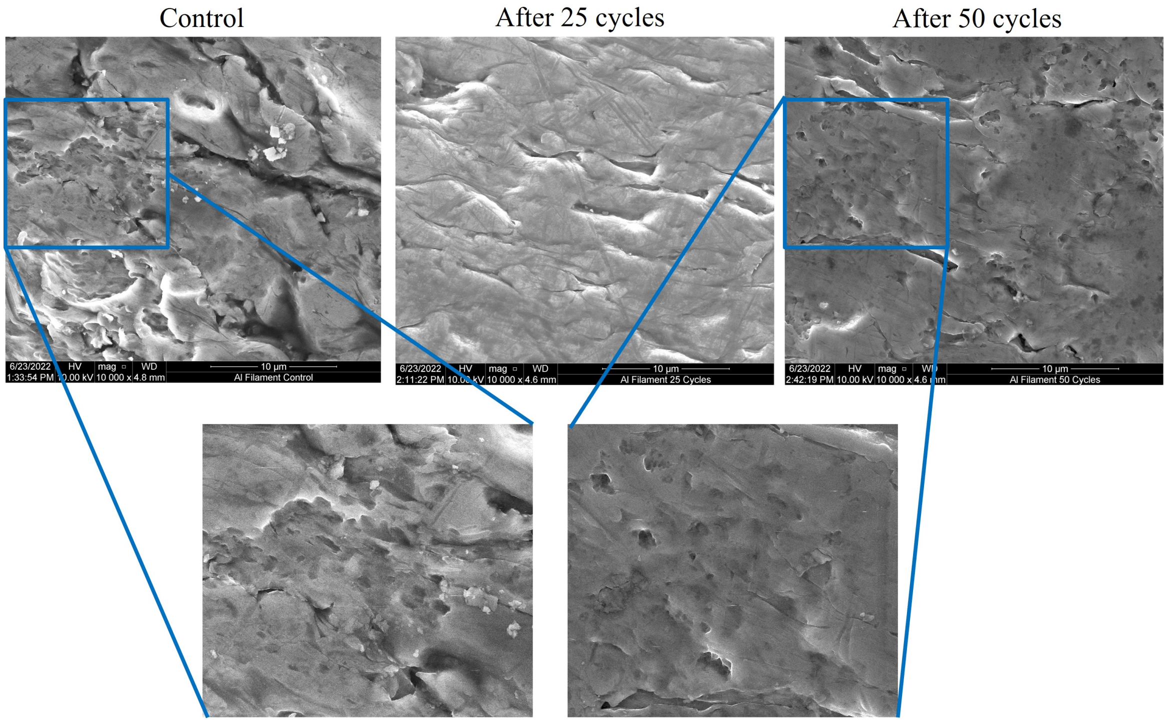

Figure 4.6. A SEM Image of SA Sample in Al-4008 filament following STA. Source: [37].

Based on STA of SA without an Al-4008 filament, peak temperature observed for SA during DSC transition showed a 0.5 % reduction after 25 cycles and 0.27 % more after 50 cycles [37]. A 9.5 % change was noted in another study following 50 cycles [42]. This could be due to the differing quality of SA used in each study since the study that noted a large change in thermophysical properties over many cycles used SA of 90 % quality whereas this research used SA of 95 % quality. Heat flow showed improvements over time with a 5.6 % increase after 25 cycles and 1.24 % more of an increase after 50 cycles. Figure 4.7 shows a much larger deviation for the heat of fusion as cycles increases to 450 [42].

From STA with an Al-4008 filament present, there was a noticeable effect on SA's ability to act as a heat transfer medium while in the presence of metal. From cycle 0-25, there was a 0.4 % reduction in peak temperature and, from cycle 25-50, there was a 0.14 % reduction in peak temperature. Heat flow also reduced by 0.7 % and 1.8 % from cycles 0-25 and 25-50, respectively [37].

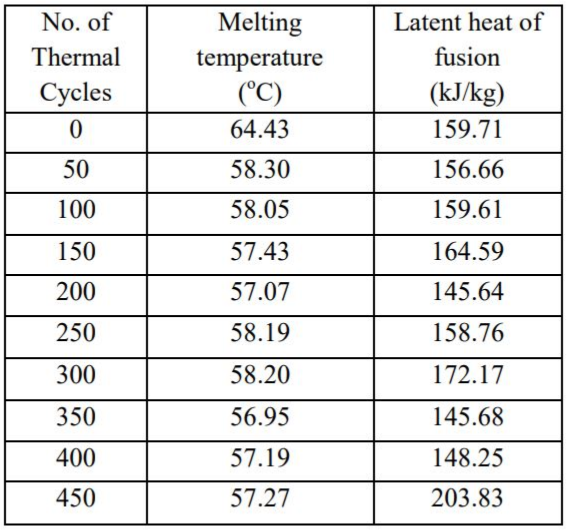

No. of Thermal Cycles	Melting temperature (^{o}C)	Latent heat of fusion (kJ/kg)
0	64.43	159.71
50	58.30	156.66
100	58.05	159.61
150	57.43	164.59
200	57.07	145.64
250	58.19	158.76
300	58.20	172.17
350	56.95	145.68
400	57.19	148.25
450	57.27	203.83

Figure 4.7. Thermal stability of SA. Source: [42].

The characteristic charging and cooling shape for a PCM is seen in Figure 4.8, which was developed by heating and cooling a box-shape heat sink. The findings of Figure 4.8 proved the concept of SA as a potentially effective PCM for thermal management.

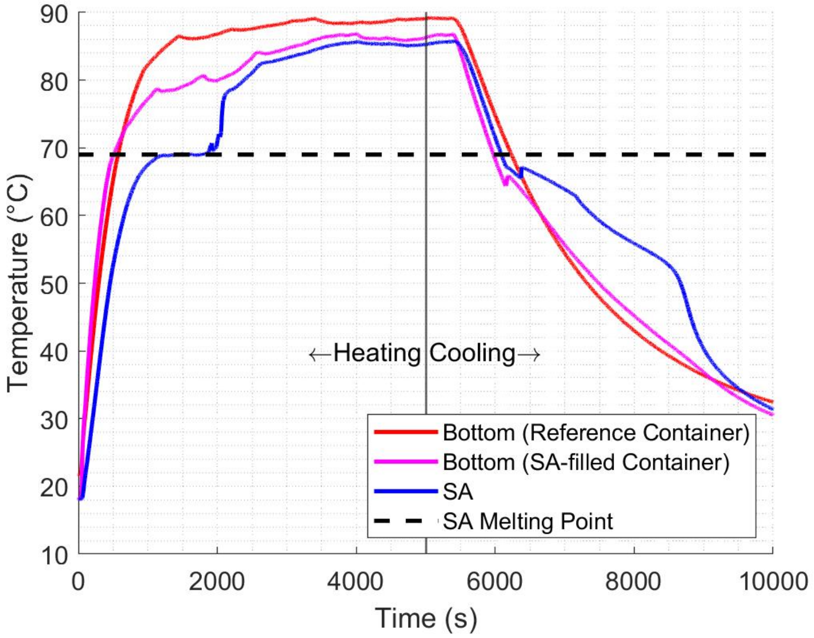

Figure 4.8. Heating and cooling cycles of a no-fin box-shape heat sink filled with SA. Source: [37].

4.3 Density Test

Table 4.1 shows the results of the density test, with units of density converted to g/cm^3. For the given temperature range, the results showed a significant change in density of SA.

Table 4.1. SA density at various temperatures.

Temperature (°C)	Density (g/cm^3)
20	0.9408
70	0.8318
80	0.8318
90	0.8281
100	0.8243
110	0.8109
120	0.7968
130	0.7776
140	0.7678

4.4 ANSYS Simulations

Each design was simulated twice: once with SA and once with Al assigned to the beige areas shown in Figure 3.25 and Figure 3.26. This was done to minimize potential discrepancies resulting from surfaces with similar geometries and material assignments but different meshes. Furthermore, the design scoping nature of the simulation did not require a refined mesh to obtain the desired performance results of the designs relative to one another. The average global temperatures of the bulk design with and without SA implementation are plotted in Figure 4.9.

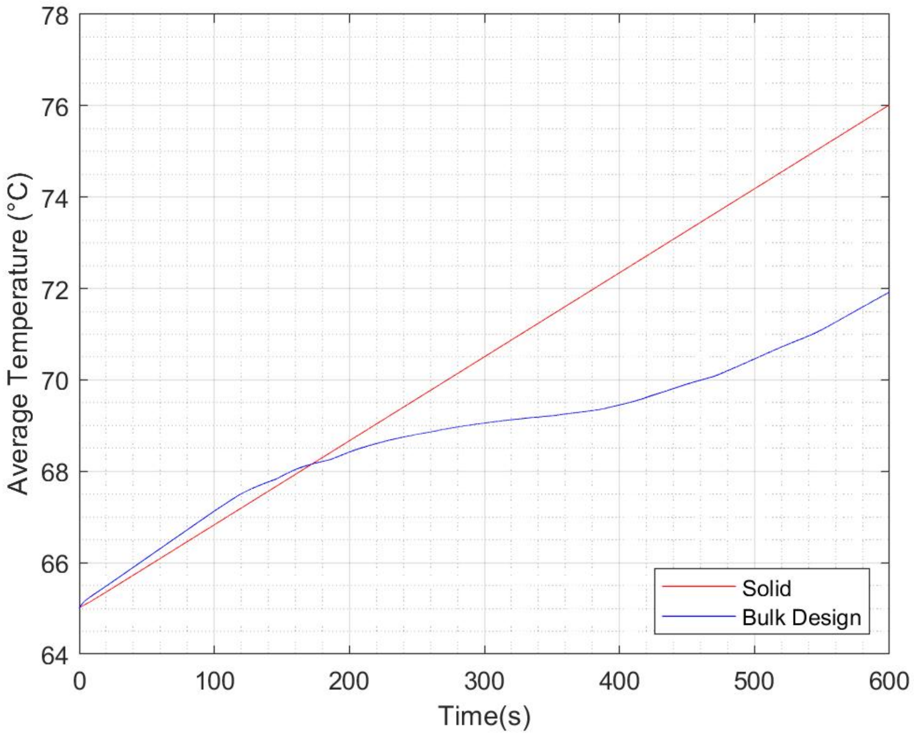

Figure 4.9. ANSYS 2D transient thermal simulation: bulk design.

Likewise, the average global temperatures of the reservoir design with and without SA implementation are plotted in Figure 4.10.

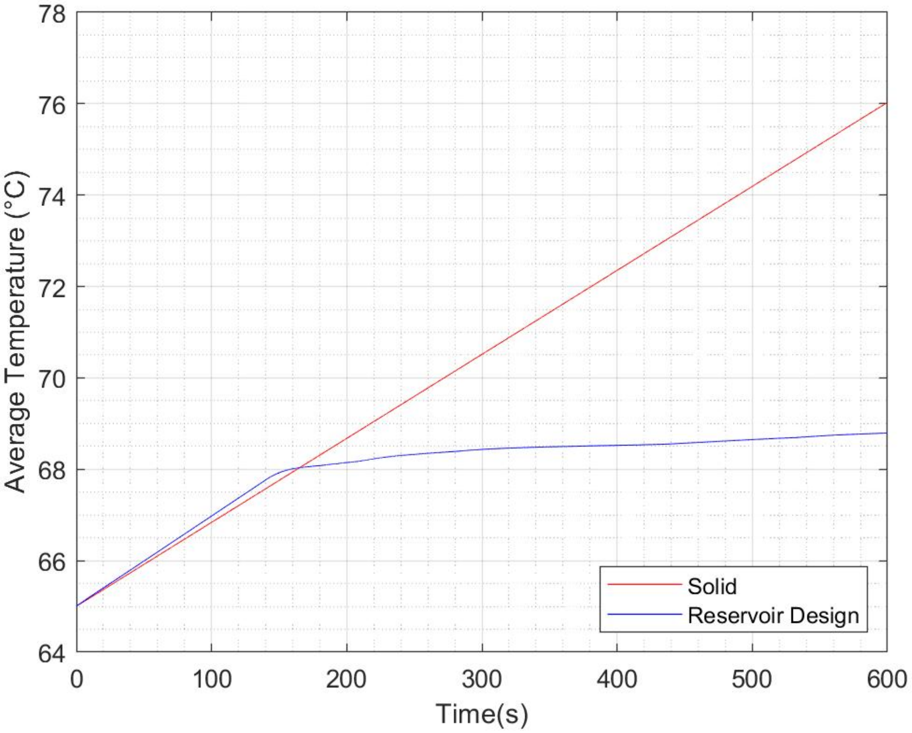

Figure 4.10. ANSYS 2D transient thermal simulation: reservoir design.

The bulk design reached an average temperature of 71.9 °C, whereas the reservoir design reached an average temperature of 68.8 °C. The phase change can be seen when the slope of each curve flattens. For the reservoir design, the geometry allowed for a more sustained exploit of the latent heat absorption during heat transfer. This is likely due to two paths: a steady state path from the source through the fins as well as a transient path for heat to the SA-filled reservoir as energy is added into the heat sink. The bulk design, on the other hand, only receives the benefit of the steady-state path as the heat passes through the bulk SA and to the fins. Therefore, based on the maximum average temperature reached and the associated thermal behavior, the reservoir design (with the SA located on the sides) was the clear choice of better design.

4.4.1 Heat Sink Final Design

Based on the results of the ANSYS simulations, the reservoir design was selected. Figure 4.11 and Figure 4.12 show the SolidWorks isometric external and section cutout views of the vessel design, respectively. The external fins are for natural convection and are expected to have limited effect during passive thermal management operations. The fins on the internal portion have gaps in the corners near the external wall. They are also at a lower height than the location of the lid, to allow for filling of SA. The interior fins provide a heat transfer advantage by providing a larger overall surface area for heat conduction to the SA. This concept was shown through analysis of Eq. 2.1 as well as the ANSYS simulation results.

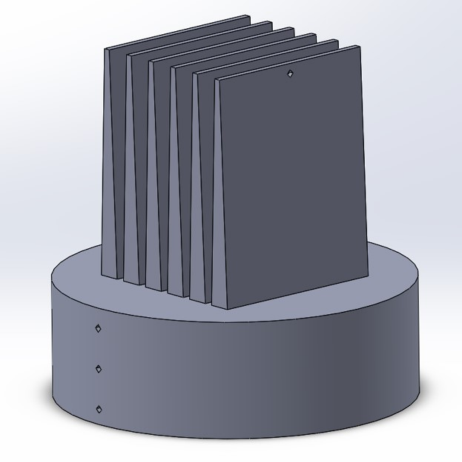

Figure 4.11. External view.

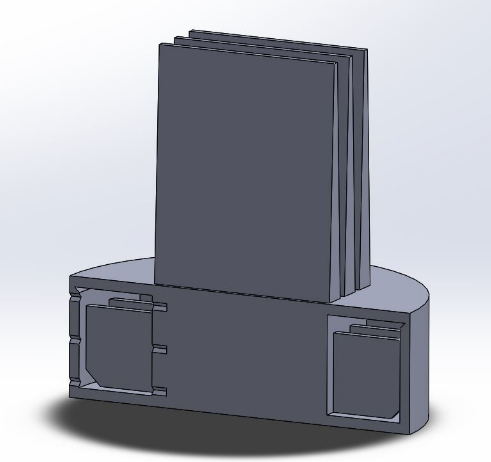

Figure 4.12. Section view.

Figure 4.13 shows the section view cutout from the top view perspective for the reservoir design. The blue regions are for the heat transfer medium (i.e, SA). The gray regions are solid Al-4008. The total volume of the space for SA was calculated, through SolidWorks to be 31.55 cm^3. This volume exceeds the calculated volume required to absorb the heat produced based on the conservative estimates in Section 3.7.3. Therefore, the design is adequate for the CPU application.

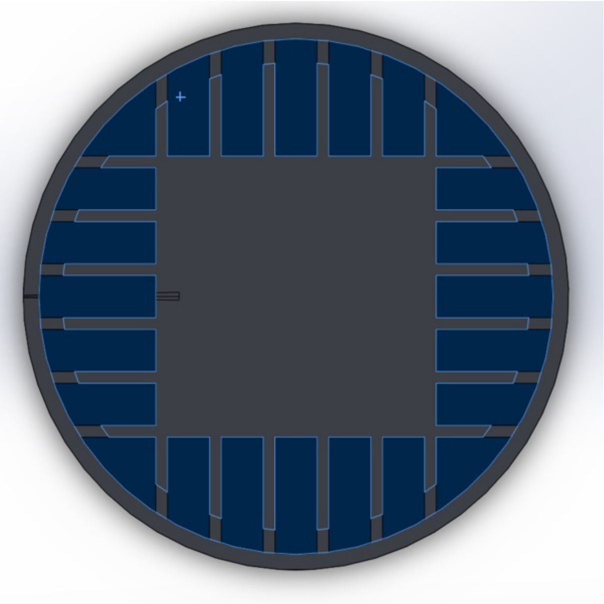

Figure 4.13. Top view cutout of reservoir design showing the reservoir area for SA.

4.5 Thermal Conductivity

As stated in Section 3.6, the thermal conductivity test was completed to verify that the inclusion of SA into the Al-4008 did not inhibit the heat flow through the heat sink. Table 4.2 summarizes the results of the thermal conductivity test. The average thermal conductivities of the reference pucks consistent with 4000 series Al. This provided validation of the process used to calculate the thermal conductivity through the SA-filled cylinder. The large gap in between TC3 and TC4 provides a visualization for the effect of SA within Al but does significant inhibition of heat transfer flow resulting from the presence of SA.

Table 4.2. Thermal conductivity test results (stearic acid).

Cylinder	Thermal Conductivity (W/mK)
Top Reference Puck	138.13
Bottom Reference Puck	159.39
Average of Reference Pucks	148.75
SA-filled Cylinder	68.85

Figure 4.14 shows the graphed results of the SA thermal conductivity test. There were minor heat losses to the heavy weight on top of the rig along with minor heat transfer losses between the hot plate and bottom cylinder. This is indicated by the lower temperature of TC1 compared to the hot plate setting. This lower temperature did not significantly impact the results of the test. The thermocouple locations provided data collection for the temperature difference calculation for each cylinder at steady state conditions so the thermal conductivity in each cylinder could be calculated, as described in Section 3.6.

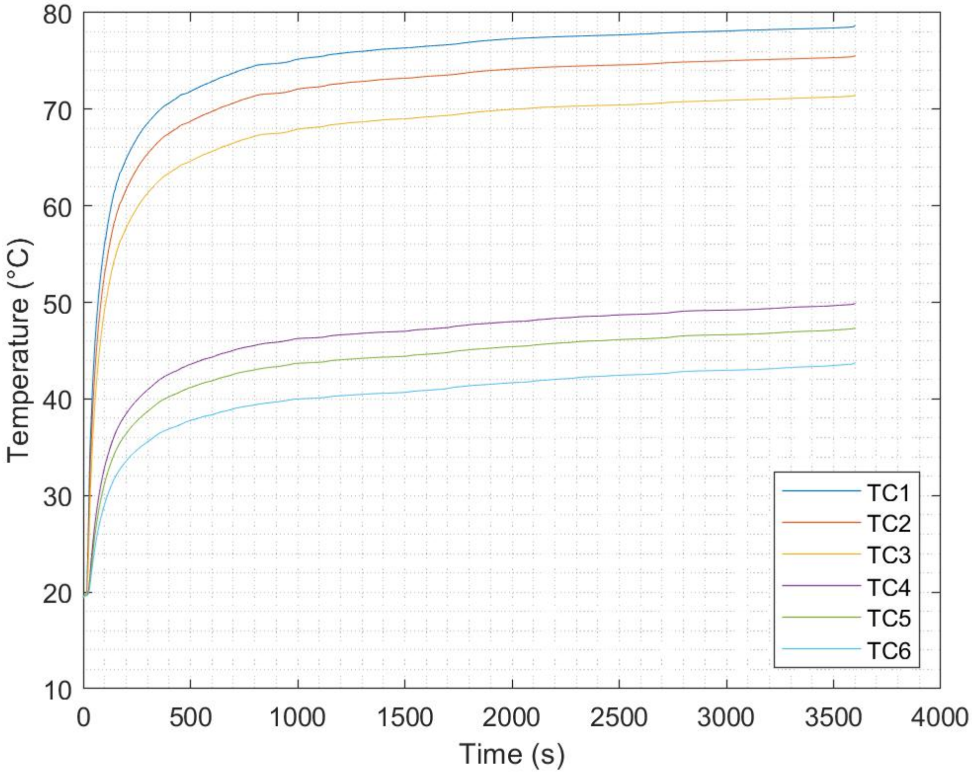

Figure 4.14. Thermal conductivity test data for SA sample.

Table 4.3 summarizes the thermocouple locations in the legend shown in Figure 4.14.

Table 4.3. Thermal conductivity test thermocouple locations.

Thermocouple	Location
TC1	Bottom of Bottom Puck
TC2	Top of Bottom Puck
TC3	Bottom of SA-filled Cylinder
TC4	Top of SA-filled Cylinder
TC5	Bottom of Top Puck
TC6	Top of Top Puck

4.6 Power Cycle Testing

Two sets of power cycle tests were completed. One was for short duty cycles over a long period (30 seconds on at high power heat load, 30 seconds off for many cycles) and the other was for a long duty cycle over a short testing period (hundreds of seconds on at high power heat load, hundreds of seconds off for a few cycles). The first set of power cycles was done to ensure sustainable thermal management capability of the selected PCM compared to a similar heat sink and to verify any potential material degradation of the PCM over many cycles did not affect its heat transfer capability. The second set was done to verify thermal stability over a sustained period of constant heat load, for one half-period of each cycle, over the course of multiple cycles.

4.6.1 Short Duty Cycle, Long Test Duration

Two tests were completed for a 30 second half period over the course of at least one hour. The first test, nearly three hours long, was with a voltage of 8.25 V (35 W). This corresponded to a resistance heater power output that was just below 35 W at the peak of the power cycle. Though below the target bound of 35 W for the CPU application, the test provided useful results. The assumption was made that heat losses to the environment were negligible based on the insulation around the resistance heater and the minimal thickness of the heat duct. The results of the first test are shown in Figure 4.15.

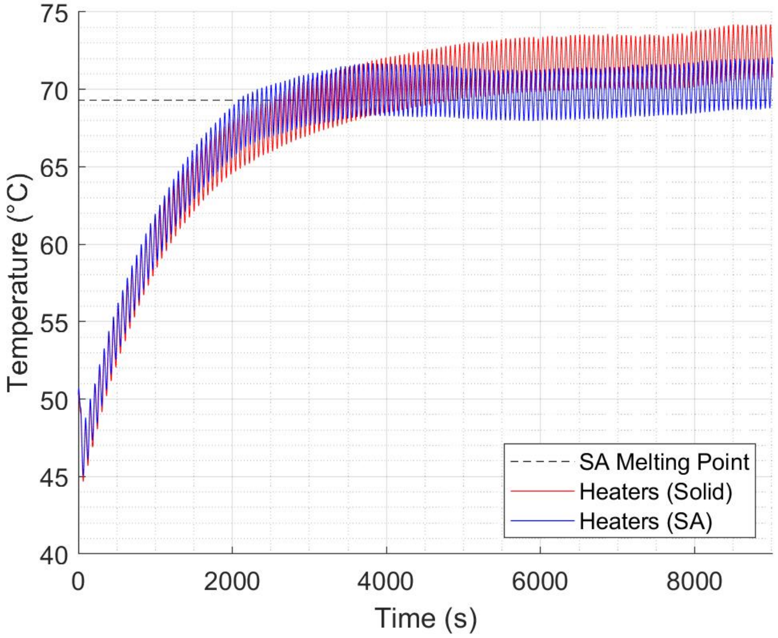

Figure 4.15. Short duty cycle, long test duration: 8.25 V (35 W).

On average, the PCM-filled heat sink performed better than the solid heat sink once the temperature increased to the operating range of the CPU. Prior to the operating temperature range, the solid heat sink reached a lower average temperature at the heater location for the modeled CPU. A slope can be derived from averaging the temperatures reached over the cyclic periods. This slope is nearly zero around the melting point of SA, indicating the advantageous effect of the solid-liquid phase transition of the SA. The solid heat sink seemingly indicated that only slightly higher temperatures were experienced but it is important to observe that the slope of the average temperatures is increasing over time, while it is relatively unchanged for the SA-filled heat sink. This unmitigated increase in temperature would be detrimental to electronic components.

The next test was with a voltage of 10 V, which corresponded to a resistance heater power output of 50 W. The results of the second test are shown in Figure 4.16. Between approximately 500 and 1500 seconds, a flattened slope, indicating the solid-liquid phase change, can be seen. The relatively isothermal heat absorption due to the latent heat of fusion exemplifies the benefit provided by the SA. Again, on average, the temperatures reached during the testing were lower for the SA-filled heat sink compared to the solid heat sink, even when past the melting point of the SA. However, it is noteworthy that there is a decrease in heat transfer capability of the PCM at higher powers. Once the phase changed from solid to liquid, the maximum temperatures reached by the SA-filled cylinder were only slightly lower than those of the solid filled heat sink. Therefore, the advantage of the SA is that it helps lower the average temperature better than it does the average peak temperature. Additionally, the region where the average temperature reached by the SA-filled heat sink becomes constant indicates that he onset of melting occurs at approximately 73 °C. This is approximately 4 °C above the average melting point of SA from review of literature. This discovery, along with the recognition that the solid heat sink seems to perform slightly better at absorbing heat prior to SA melting, indicate that selection of the proper PCM for a given operating temperature range is crucial to success of the heat sink. It also gives credence to the importance to choosing a PCM with reliable thermophysical data with low uncertainty and suggests that more research is required for SA thermophysical data.

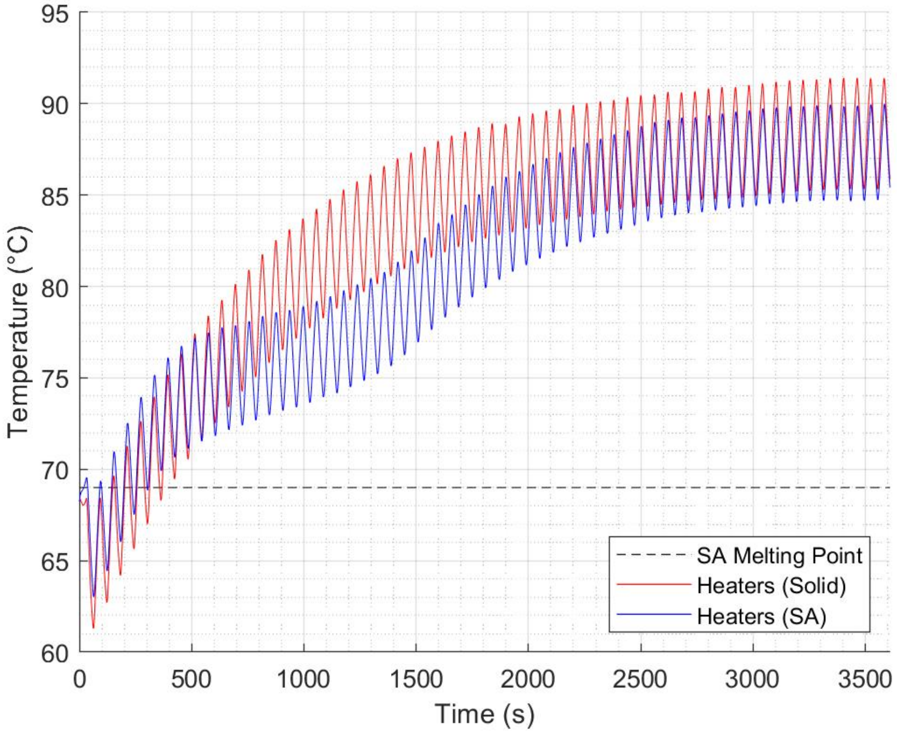

Figure 4.16. Short Duty Cycle, Long Test Duration: 10 V (50 W).

4.6.2 Long Duty Cycle, Short Test Duration

SA vs. Solid Heat Sink

The next test was with a long duty cycle and a short overall test duration. The first duty cycle is not shown to remove bias following heat-up, which provided erroneous results on the plot. In all tests, note the stability of the heat pad temperatures for the SA-filled heat sinks throughout each cycle as they reach nearly identical maximum and minimum temperatures.

The 100 second test for the SA vs. solid heat sink is shown in Figure 4.17. The 9 V in each test corresponded to approximately 40 W of power from the resistance heaters. The maximum difference in peak temperature between the heaters under the solid and the heaters under the SA-filled heat sink was 1.5 °C. The maximum heater temperature reached for the solid heat sink was approximately 83 °C. The heaters under the solid heat sink experienced approximately a 10 °C thermal transient. The heaters under the SA-filled heat sink also experienced approximately a 10 °C thermal transient.

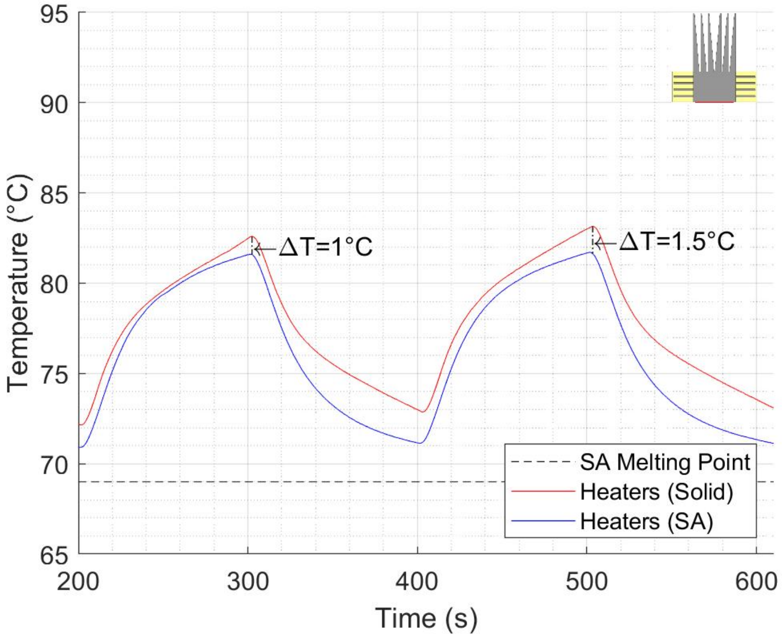

Figure 4.17. SA vs. solid heat sink: 100 second duty cycle.

The 200 second test for the SA vs. solid heat sink is shown in Figure 4.18. The maximum difference in peak temperature between the heaters under the solid and the heaters under the SA-filled heat sink was 4.5 °C. The maximum heater temperature reached for the solid heat sink was approximately 87.5 °C. The heaters under the solid heat sink experienced approximately a 12.5 °C thermal transient. The heaters under the SA-filled heat sink also experienced approximately a 12.5 °C thermal transient.

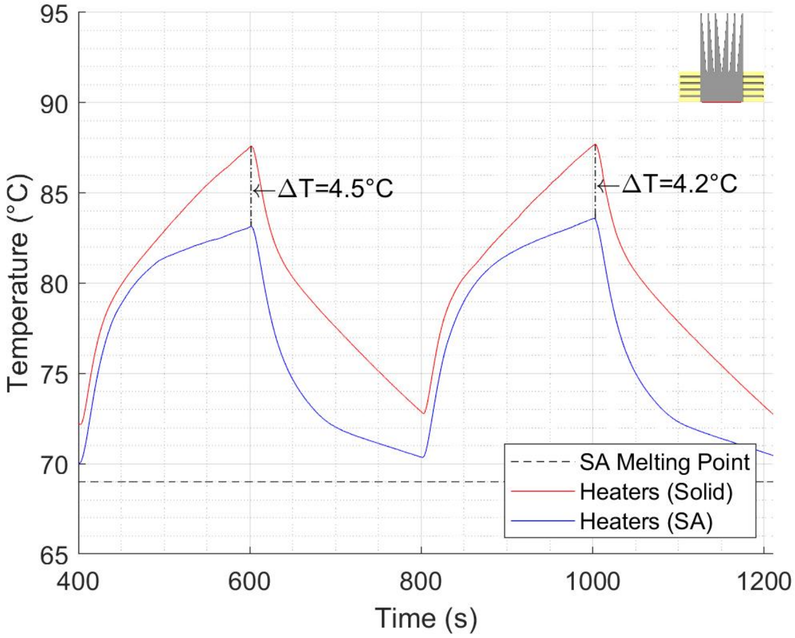

Figure 4.18. SA vs. solid heat sink: 200 second duty cycle.

The results from the 300 second test were essentially an amplification of the results from the 100 second test, as shown in Figure 4.19. Higher peak temperatures were reached and there were increased thermal amplitudes throughout the duty cycles. At approximately 72 °C, the onset of solidification can be seen for SA based on the decrease in slope during the power-off portion of the duty cycle. Additionally, the increased time of the resistance heater power-off state allowed the SA to dissipate more heat over time and solidify. The cyclic phase change improved the thermal management capability of the SA, which accounts for only a 1 °C increase in peak temperature compared to the 100 second test result. In contrast, the solid heat sink 300 second test reached a peak temperature that was up to 5 °C higher than the 100 second test. The maximum difference in peak temperature between the heaters under the solid and the heaters under the SA-filled heat sink was 4.9 °C. The maximum heater temperature reached for the solid heat sink was approximately 89.5 °C. The heaters under the solid heat sink experienced approximately a 19 °C thermal transient whereas the heaters under the SA-filled heat sink experienced approximately a 15 °C thermal transient.

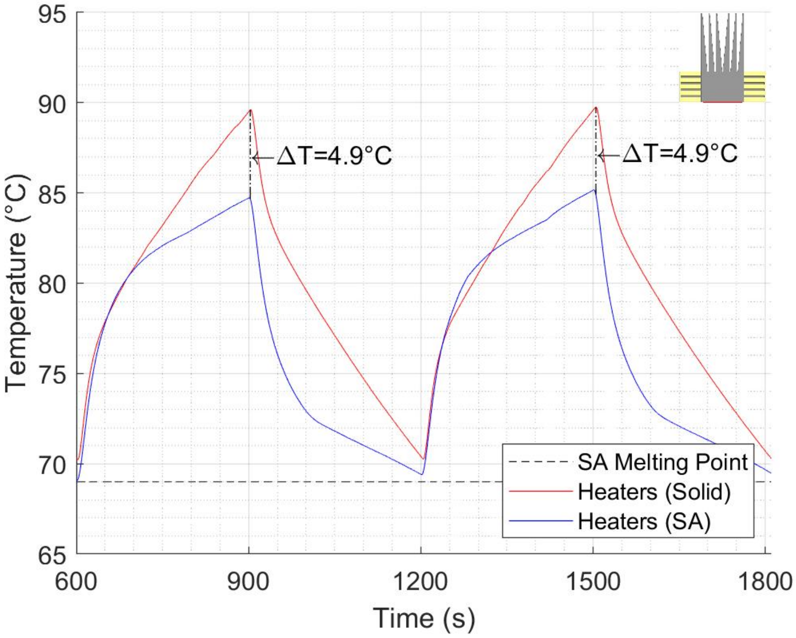

Figure 4.19. SA vs. solid heat sink: 300 second duty cycle.

Relative to the solid heat sink, the SA-filled heat sink overall reached lower peak temperatures, a relatively constant peak temperature over duty cycles and a lower amplitude thermal cycle per each duty cycle. Furthermore, the solid heat sink increased in temperature over each duty cycle. Though each set of results reached temperatures above the melting point of SA, the relative thermal response to each other were favorable to determining that SA is an effective PCM for thermal management in a cyclic thermal loading application.

SA vs. Hollow Heat Sink

The 100 second test for the SA vs. hollow heat sink is shown in Figure 4.20. The maximum difference in peak temperature between the heaters under the hollow (air-filled) and the heaters under the SA-filled heat sink was 0.5 °C. The maximum heater temperature reached for the hollow heat sink was approximately 82 °C. The heaters under the hollow heat sink experienced approximately an 11.5 °C thermal transient whereas heaters under the SA-filled heat sink experienced approximately a 10 °C thermal transient.

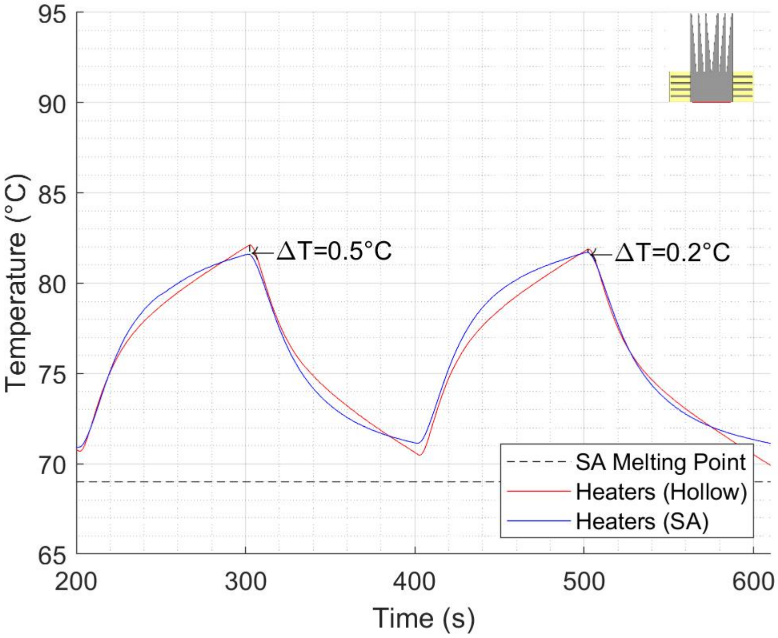

Figure 4.20. SA vs. hollow heat sink: 100 second duty cycle.

The 200 second test for the SA vs. hollow heat sink is shown in Figure 4.21. The maximum difference in peak temperature between the heaters under the hollow (air-filled) and SA-filled heat sink was approximately 3.8 °C. The maximum heater temperature reached for the hollow heat sink was approximately 87 °C. The heaters under the hollow heat sink experienced an 18 °C thermal transient whereas the heaters under the SA-filled heat sink experienced approximately a 12 °C thermal transient.

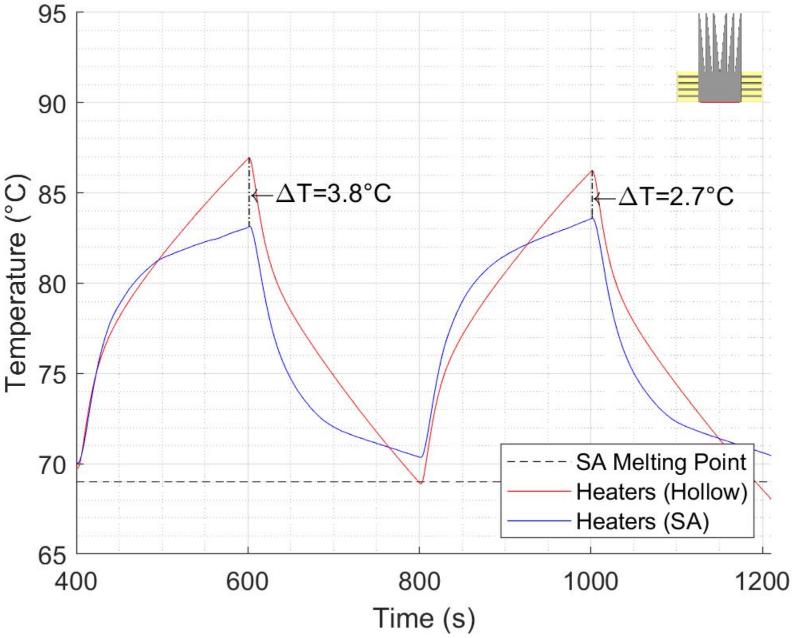

Figure 4.21. SA vs. hollow heat sink: 200 second duty cycle.

The 300 second test for the SA vs. hollow heat sink is shown in Figure 4.22. The maximum difference in peak temperature between the heaters under the hollow (air-filled) and SA-filled heat sink was approximately 5 °C. The maximum heater temperature reached for the hollow heat sink was approximately 89.5 °C. The heaters under the hollow heat sink experienced a 23.5 °C thermal transient whereas the heaters under the SA-filled heat sink experienced approximately a 15 °C thermal transient.

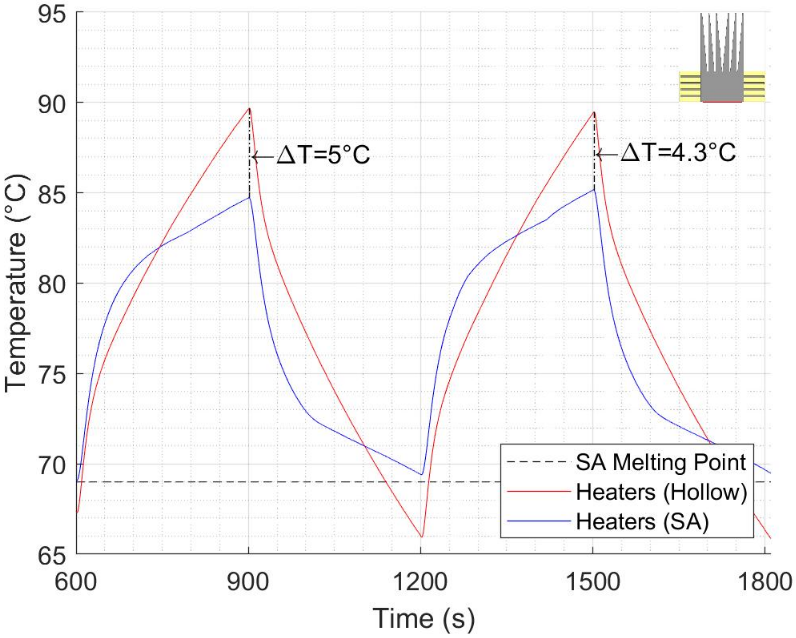

Figure 4.22. SA vs. hollow heat sink: 300 second duty cycle.

As expected, the SA-filled heat sink performed better than the hollow (air-filled) heat sink. The most alarming comparison was between the thermal transients, where the heaters under the hollow heat sink experienced much more severe thermal transients that the SA-filled heat sink. Compared to the tests with the solid heat sink, the thermal transient was larger for the hollow heat sink. This test was valuable to confirm that reluctance to include PCM in a hollow design would yield unfavorable thermal management results.

SA vs. Soybean Oil-filled Heat Sinks

The 100 second test for the SA vs. soybean oil-filled heat sink is shown in Figure 4.23. The maximum difference in peak temperature between the heaters under the soybean oil-filled and SA-filled heat sink was 2.9 °C. The maximum heater temperature reached for the soybean oil-filled heat sink was approximately 84 °C. The heaters under both heat sinks experienced approximately a 10 °C thermal transient.

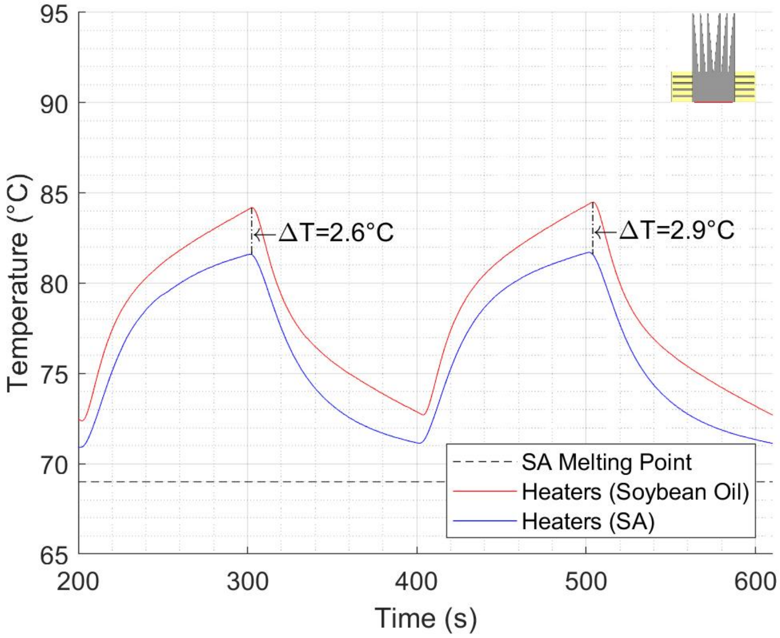

Figure 4.23. SA vs. soybean oil-filled heat sink: 100 second duty cycle.

The 200 second test for the SA vs. soybean oil-filled heat sink is shown in Figure 4.24. The maximum difference in peak temperature between the heaters under the soybean oil-filled and SA-filled heat sink was 5.7 °C. The maximum heater temperature reached for the soybean oil-filled heat sink was approximately 88.5 °C. The heaters under the soybean oil-filled heat sink experienced a thermal transient of approximately 16 °C while the heaters under the SA-filled heat sink experienced a thermal transient of approximately 12.5 °C.

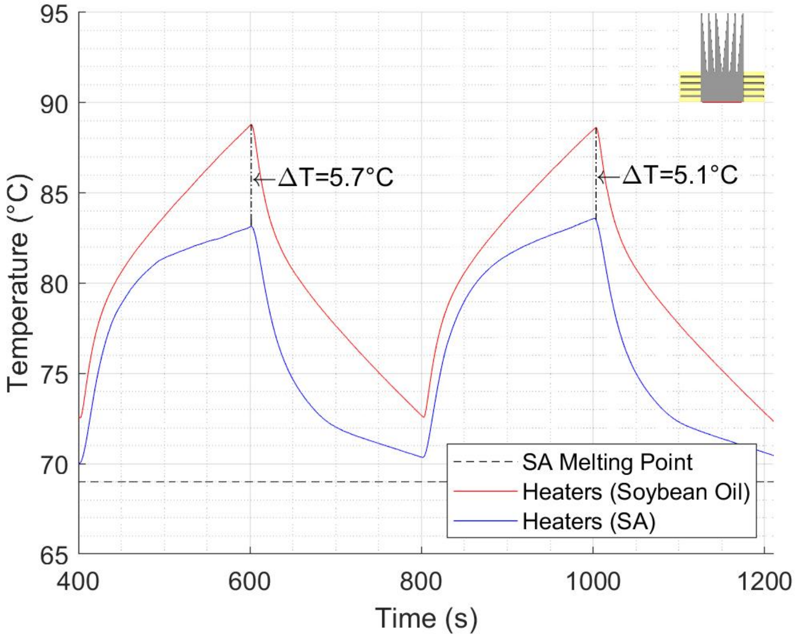

Figure 4.24. SA vs. soybean oil-filled heat sink: 200 second duty cycle.

The 300 second test for the SA vs. soybean oil-filled heat sink is shown in Figure 4.25. The maximum difference in peak temperature between the heaters under the soybean oil-filled and SA-filled heat sink was 7.5 °C. The maximum heater temperature reached for the soybean oil-filled heat sink was approximately 92 °C. The heaters under the soybean oil-filled heat sink experienced a thermal transient of approximately 19 °C while the heaters under the SA-filled heat sink experienced a thermal transient of approximately 15 °C.

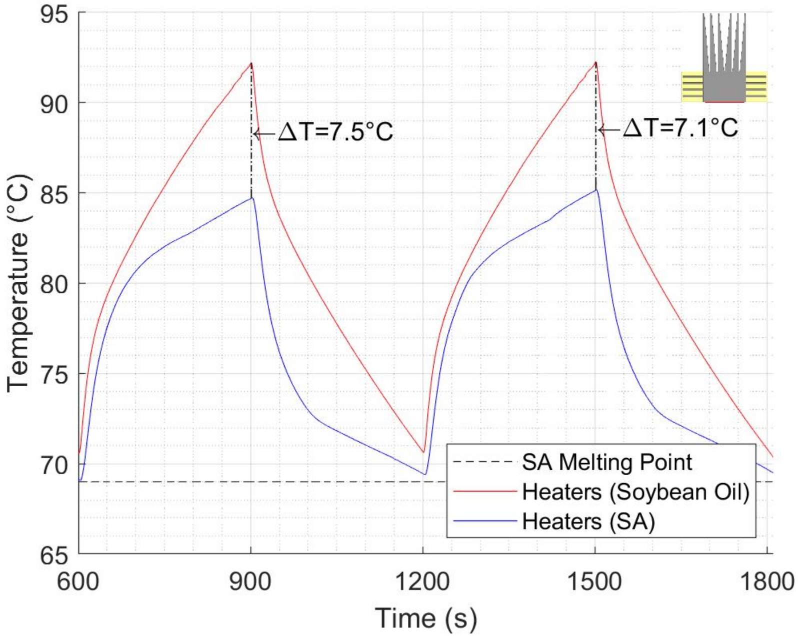

Figure 4.25. SA vs. soybean oil-filled heat sink: 300 second duty cycle.

The liquid-filled heat sink was used as a control to compare to the phase change impact of the SA, proving the phase change was an effective thermal management strategy. The SA-filled heat sink performed significantly better with respect to peak temperature and thermal transient.

SA vs. Glycerol-filled Heat Sinks

The 100 second test for the SA vs. glycerol-filled heat sink is shown in Figure 4.26. The maximum difference in peak temperature between the heaters under the glycerol-filled and SA-filled heat sink was 3.3 °C. The maximum heater temperature reached for the glycerol-filled heat sink was approximately 85 °C. The heaters under the glycerol-filled heat sink experienced a thermal transient of approximately 14 °C while the heaters under the SA-filled heat sink experienced a thermal transient of approximately 10 °C.

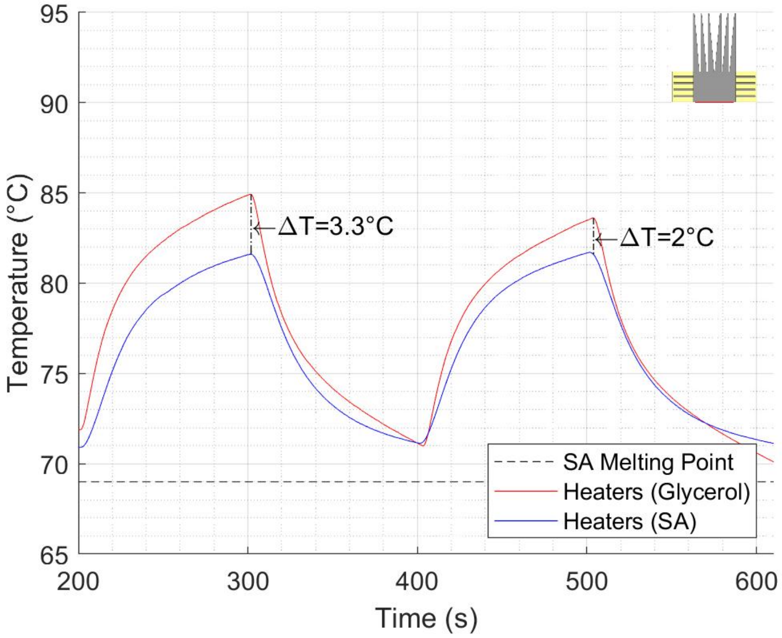

Figure 4.26. SA vs. glycerol-filled heat sink: 100 second duty cycle.

The 200 second test for the SA vs. glycerol-filled heat sink is shown in Figure 4.27. The maximum difference in peak temperature between the heaters under the glycerol-filled and SA-filled heat sink was 4.3 °C. The maximum heater temperature reached for the glycerol-filled heat sink was approximately 87.5 °C. The heaters under the glycerol-filled heat sink experienced a thermal transient of approximately 18 °C while the heaters under the SA-filled heat sink experienced a thermal transient of approximately 12.5 °C.

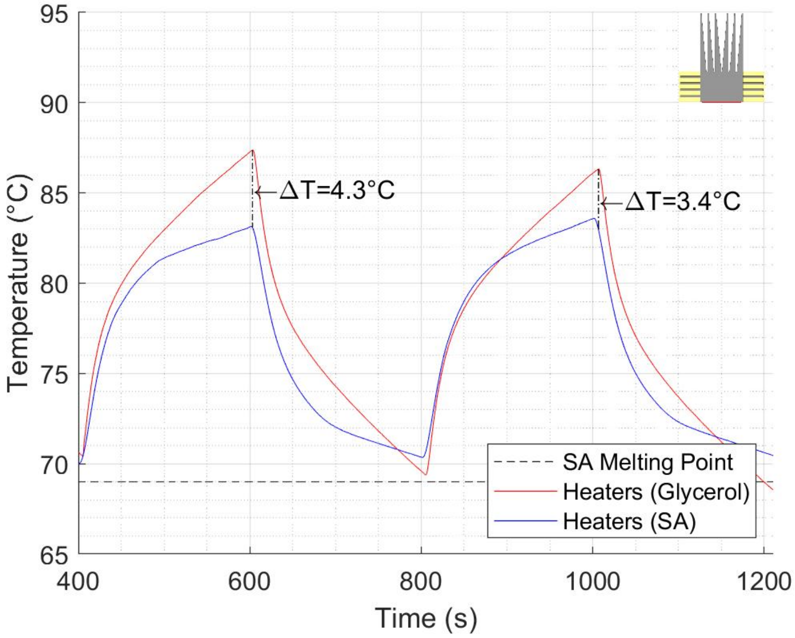

Figure 4.27. SA vs. glycerol-filled heat sink: 200 second duty cycle.

The 300 second test for the SA vs. glycerol-filled heat sink is shown in Figure 4.28. The maximum difference in peak temperature between the heaters under the glycerol-filled and SA-filled heat sink was 5.5 °C. The maximum heater temperature reached for the glycerol-filled heat sink was approximately 90 °C. The heaters under the glycerol-filled heat sink experienced a thermal transient of approximately 23 °C while the heaters under the SA-filled heat sink experienced a thermal transient of approximately 15 °C.

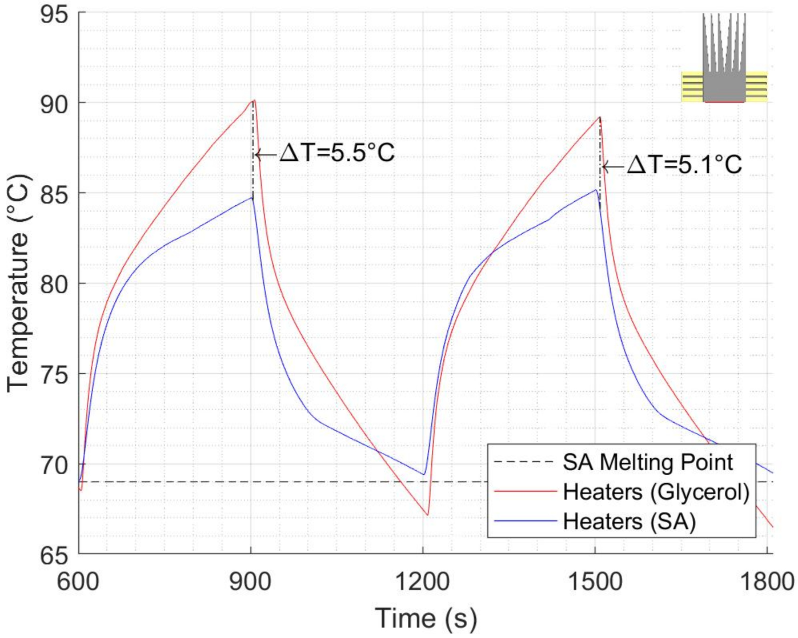

Figure 4.28. SA vs. glycerol-filled heat sink: 300 second duty cycle.

In all cases, the SA-filled heat sink performed better than the heat sinks filled with either soybean oil or glycerol. The glycerol and soybean oil remained liquid throughout the test and were tested soon after filling the heat sink to minimize potential material interaction of the fluid with the Al-4008 substrate. All heat sinks had similar internal geometries, but minor differences could have occurred during the manufacturing process. However, these geometrical differences would have been negligible with respect to total internal volume. Thus, biased to the results was reduced from corrosion and geometrical inconsistencies. Given the similar thermophysical properties of soybean oil and glycerol to the range of published values for SA, the results of these tests confirmed the thesis since, for heat sinks of similar geometry, the phase change provided advantageous thermal management ability and reduced the average component temperature.

Table 4.4 summarizes the results of the power cycle tests with a primary observation for each. The SA-filled heat sink maintained a stable temperature band throughout each cycle.

Table 4.4. Summary of power cycles results for long duty cycle, short test duration.

Test	Better Performance	Primary Observation
SA vs. Solid (100 s)	SA-filled heat sink	Lower overall temperature by 1.5 °C
SA vs. Solid (200 s)	SA-filled heat sink	Lower overall temperature by 4.5 °C
SA vs. Solid (300 s)	SA-filled heat sink	Lower overall temperature by 4.9 °C
SA vs. Hollow (100 s)	SA-filled heat sink	Smaller thermal transient by 1.5 °C
SA vs. Hollow (200 s)	SA-filled heat sink	Smaller thermal transient by 5.5 °C
SA vs. Hollow (300 s)	SA-filled heat sink	Smaller thermal transient by 8.5 °C
SA vs. Soybean Oil (100 s)	SA-filled heat sink	Lower overall temperature by 2.9 °C
SA vs. Soybean Oil (200 s)	SA-filled heat sink	Lower overall temperature by 5.7 °C
SA vs. Soybean Oil (300 s)	SA-filled heat sink	Lower overall temperature by 7.5 °C
SA vs. Glycerol (100 s)	SA-filled heat sink	Smaller thermal transient by 4 °C
SA vs. Glycerol (200 s)	SA-filled heat sink	Smaller thermal transient by 5.5 °C
SA vs. Glycerol (300 s)	SA-filled heat sink	Smaller thermal transient by 8 °C

Based on the summary of the power cycle results, it is clear that the objectives of Section 1.2 were met during the study since, in all tests:

- The SA-filled heat sink reduced the average temperature of a cyclically thermally loaded component compared to heat sinks of similar geometry and thermophysical properties.
- The SA-filled heat sink reduced the peak temperature of a cyclically thermally loaded component compared to heat sinks of similar geometry and thermophysical properties.
- The SA-filled heat sink regulated the thermal transient by maintaining the temperature of a cyclically thermally loaded component within a narrow, consistent temperature range. Heat sinks of similar geometry and thermophysical properties did not achieve the same results.

THIS PAGE INTENTIONALLY LEFT BLANK

CHAPTER 5: Concept Development

The design methodology was clearly established SA throughout each section of Chapter 3 and is reviewed in the following list:

1. Select an application requiring passive thermal management.
2. Select an AM for heat sink production and perform a design study using the code in Appendix A, modifying it as necessary to determine limitations of the AM method.
3. Select a PCM based on the operating temperature of the selected application.
4. Perform material interaction tests (i.e., STA and SEM imaging) between the selected PCM and printed heat sink container material to determine thermophysical properties of PCM and its compatibility with the container.
5. Perform density and containment testing to determine the transient thermal response of the PCM within the container material.
6. Perform a thermal conductivity test to determine expected heat flow through PCM while it is within the cavity of the hollow printed container.
7. Perform 2D transient thermal simulations to scope potential designs and determine, relatively, which heat sink design produces a lower average temperature given a heat source boundary condition.
8. Develop a test rig and build a data acquisition system to collect data generated during experimental testing. Ensure the components of the test rig (programmable power supply, heating element and programming environment) are all compatible and support generating required boundary conditions.

With the design methodology tested and established, the potential for concept development led to further research into metal PCM addition into a part during printing and the potential to induce a natural circulation loop in the fin of a heat sink.

5.1 Metal PCM Application

The design intended to incorporate the SA into the Al-4008 during printing, as mentioned in Section 3.7.1 was not possible since the boiling point of SA was 361 °C while the ElemX print bed temperature was 475 °C [41]. There was no method that could form a composite filler material or add SA to the heat sink material while printing without the SA vaporizing upon contact with the surface temperatures required for printing. Therefore, to research the possibility of adding a PCM to the liquid metal while printing, the boiling point needed to be above the bed plate temperature during printing. Furthermore, the post-processing required to fill the heat sink with SA proved challenging to contain and was not ideal for efficiency, reliability and consistency of production. Out of the metals PCMs discussed in Section 3.3, FM was chosen based on non-toxicity and a boiling point exceeding 1500 °C based on the composition of metals [34].

The material interaction between the FM PCM and Al-4008 substrate was not a focus of this work nor was it required to prove the ability to add FM while printing the heat sink. However, a macroscopic examination of the interaction at print bed temperature needed to be conducted to ensure the high temperature did not provide a catalyst for rapid corrosion of FM through the Al-4008. The basis for this concern is shown in Figure 5.1, where FM corrodes through Al. Of note, the type of Al was not revealed nor was the temperature. However, the corrosion (dark gray region) provided reason for concern. Therefore, a FM heating test was conducted to observe the corrosive behavior of the FM at print bed temperature on Al-4008.

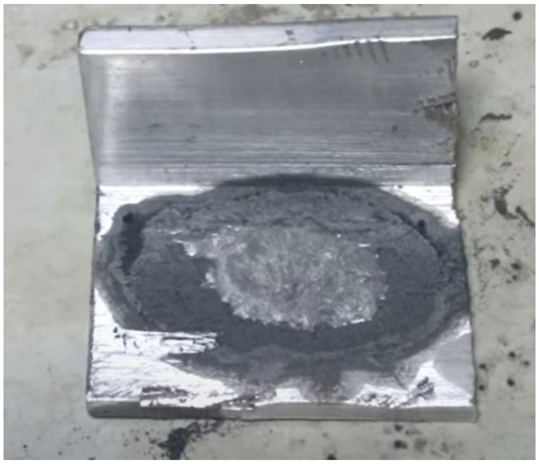

Figure 5.1. Effect of heating FM onto Al. Source: [16].

Figure 5.2 shows the preparation and results of the heating test. The heatup was conducted on a hot plate, external to the printer and at atmospheric conditions to provide a conservative environment comparable to the environment experienced within the ElemX printer. The image to the left shows the FM following melting on an Al-4008 substrate. It behaved like solder and was able to be scraped off with a fingernail. The image on the right shows the change in color of the FM following a 20 minute heat up of the Al-4008 substrate to approximately bed plate print temperature (475 °C). The high temperature was then held for 10 minutes. The 10 minute hold was based on the approximate time remaining in the print to secure a lid on a container and print overhead, as described in Section 3.5.1. The results of the test revealed some oxidation for theFM after heating but there was no macroscopic material degradation of the Al-4008 substrate.

Figure 5.2. Material interaction of FM on Al-4008 substrate before (left) and after (right) heating test.

Though the heat up test showed no reason for concern during the print process, extra precautions were taken to protect the bed plate should FM escape the print container for any reason. To allow the ability to perform follow-on thermal characteristic testing, the design chosen for printing was similar to the thermal conductivity test for SA. However, 3 mm of thickness was added to the walls and 5 mm of thickness was added to the top and bottom of the hollow middle cylinder. Additionally, a "skirt" was added to the bottom of the part as a tray to catch any FM that may not make it in the hollow section during printing. This was based on the unknown level of expansion due to temperature change experienced by the FM during addition as well as the movement of the bed plate during the final layers of printing after filling. The lid, shown mated to the top of the hollow region, contained a hole to ensure no air remained in the cylinder following filling.

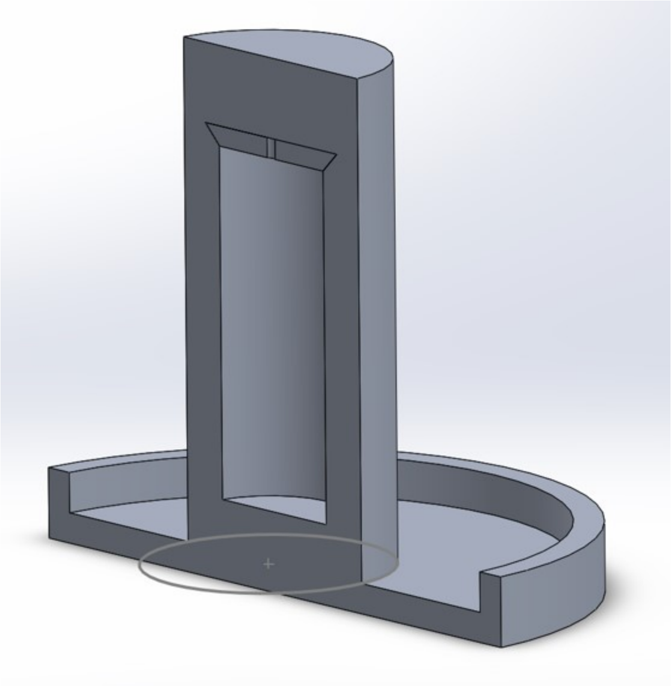

Figure 5.3. Isometric section view of FM thermal conductivity test SolidWorks model.

Ingots were added to the container by cutting small pieces of FM from the 0.11 kg (4 ounce) ingot received by RotoMetals and individually placing them in the hollow section with tongs, as shown in Figure 5.4. For each ingot, level was visually verified below the chamfered region for the lid.

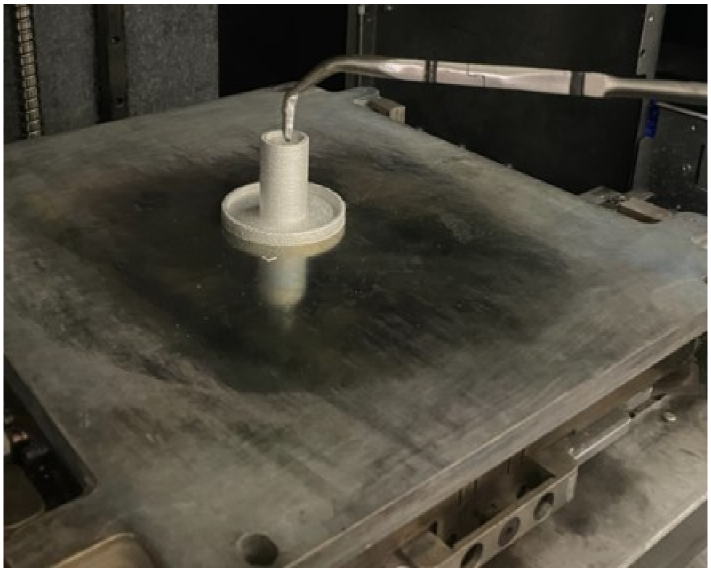

Figure 5.4. Addition of piece of FM ingot into thermal conductivity test cylinder during print.

Figure 5.5 and Figure 5.6 show the filled hollow region with liquid FM and the lid placed on the container, respectively. The oxidation of the FM, revealing a brown color, was noted to be consistent with the heating test. The lid was placed into the chamfered region with tongs prior to securing it in place.

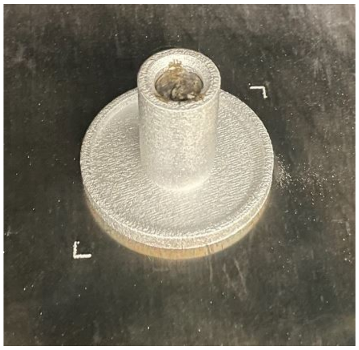

Figure 5.5. Liquid FM in cylinder.

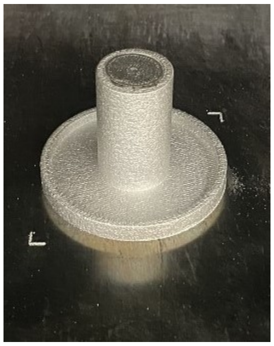

Figure 5.6. Lid on cylinder.

Securing the lid while ensuring the cylinder free of air was done by covering the hole with a tool, as shown in Figure 5.7, and lightly tapping the tool with a mallet against the lid to catch the FM coming through the center of the hole. Then, any excess FM on the top of the lid was scraped off onto the skirt. The frequency of the machine was then reduced to approximately 30 % to minimize vibrations of the print bed during the printing of follow-on layers. The concern was that the vibrations would cause sloshing of the FM within the open cylinder and cause it to spill over. Even though the catch tray was designed to prevent FM contact with the bed plate, it was important to take all precaution to minimize risk of spill over. Once a few layers were added to the top of the cylinder and the risk of spill over was no longer present, the frequency of the printer was increased to 100% to minimize the time the FM was at the bed plate temperature. This was done to minimize any further corrosion.

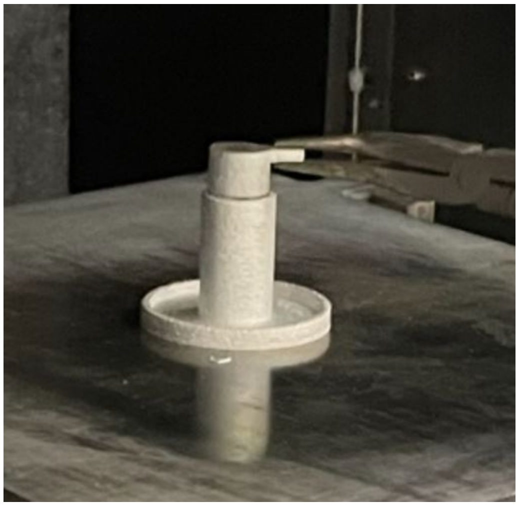

Figure 5.7. Placement of tool during FM fill level verification and lid placement.

Once complete, the part was manufactured to match the dimensions as closely as possible to the SA thermal conductivity cylinder dimension in Section 4.5. The skirt was removed using a lathe, which also ensured an even, flat bottom. Rather than using a polishing machine to polish the top and bottom of the cylinder, wet sanding was done using the same grit levels as 3.15 to support a controlled reduction of material. The thermocouples were drilled to provide a temperature differential over the same distance as the SA thermal conductivity tests. Figure 5.8 and Figure 5.9 show the printed part and the post-manufactured part, respectively.

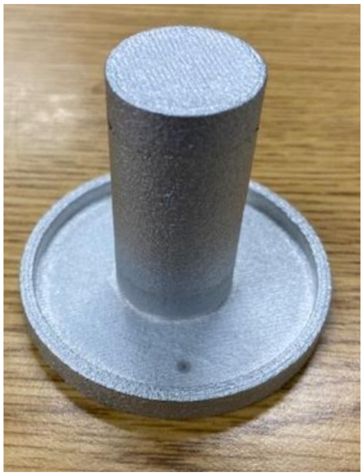
Figure 5.8. Printed.


Figure 5.9. Post-Manufactured.

The thermal conductivity test was conducted using a similar process and the same parts as in Section 4.5. Nominal and measured values of the test cylinders were noted, as shown in Table 5.1. The “Diameter” measurements were with respect to the cylinder contact surface diameters whereas the “Length” measurements were the distance between thermocouples for each cylinder. Again, the “Length” for the FM-filled cylinder was longer based on the increased thickness precaution taken during manufacturing.

Table 5.1. Thermal conductivity test nominal and measured values for applicable cylinder dimension.

Dimension	Nominal Value	Measured Value
Top Reference Puck Length (mm)	15	15.88
Middle Cylinder Length (mm)	45	46.80
Bottom Reference Puck Length (mm)	15	14.85
Top Reference Puck Diameter (mm)	25	25.18
Middle Cylinder Diameter (mm)	25	24.90
Bottom Reference Puck Diameter (mm)	25	25.15

Table 5.2 summarizes the results of the thermal conductivity test for FM. The average thermal conductivities of the reference pucks was, again, consistent with 4000 series Al. This, again, provided validation of the process used to calculate the thermal conductivity through the FM-filled cylinder since the average value is almost identical to the Al-4008 value.

Table 5.2. Thermal conductivity test results (Field's Metal).

Cylinder	Thermal Conductivity (W/mK)
Top Reference Puck	141.16
Bottom Reference Puck	155.54
Average of Reference Pucks	148.34
FM-filled Cylinder	100.09

Graphical thermal conductivity results for FM are shown in Figure 5.10. The surface of the hot plate was set to 110 °C to reach steady state and ensure the temperatures were within the melt range of the FM. The higher thermal conductivity is most attributable to the metallic composition of FM. Even though the thermocouple distance was similar for both tests, some inaccuracies may be present based on the increased thickness of the Al-4008 container. The large gap in between TC3 and TC4 provides a visualization for the effect of SA within Al but does significant inhibition of heat transfer flow resulting from the presence of SA. The shape of the curves are also closer together due to the improved thermal conductivity of the cylinder filled with a metal instead of SA.

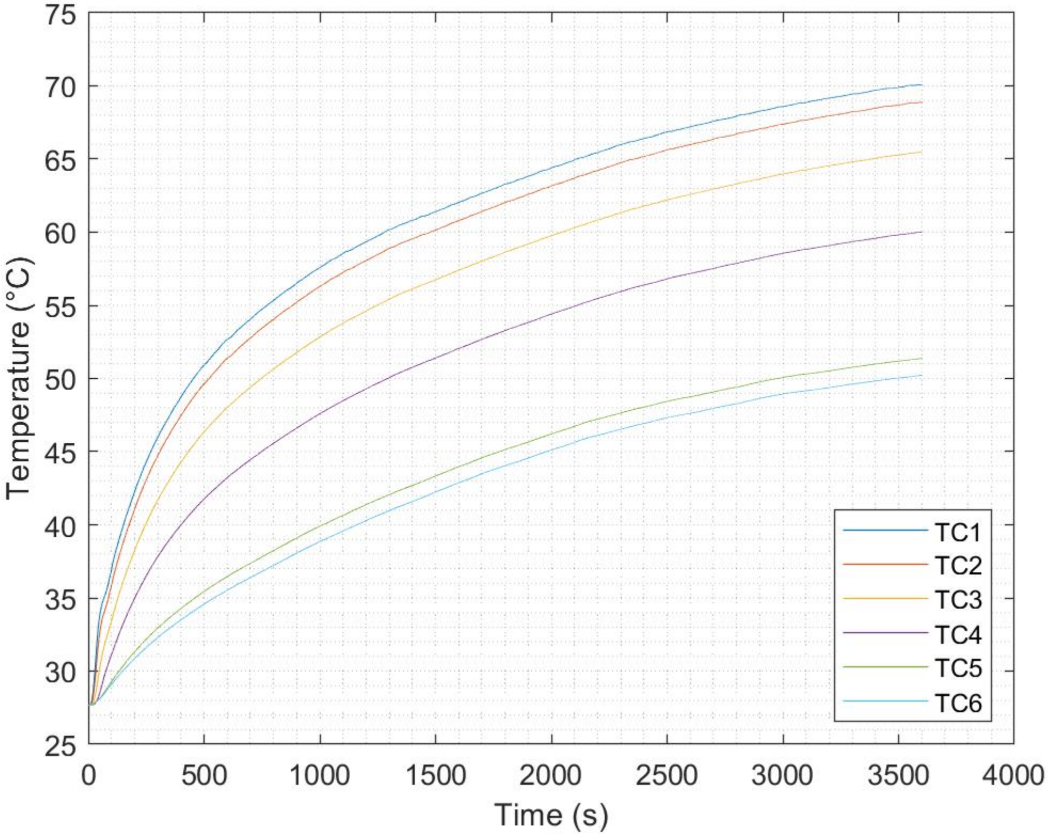

Figure 5.10. Field's Metal thermal conductivity results.

5.2 Natural Circulation

Another strategy of thermal management attempts to exploit the convective heat transfer capability of SA natural circulation. As fluid moves across the area connected to an external heat source, heat is continuously transferred to the fluid. While in liquid form, the PCMs would absorb sensible heat and reject it as it moves to the cooler regions of the channel. The natural circulation convection is not to be confused with increased convective heat transfer resulting from the buoyancy effects during melting of the SA [50]. Rather, this strategy assumes the SA is already melted and is similar to fluid flowing through a heat exchanger, transferring heat as lower temperature fluid from a colder section of the piping flows past the heat source. The difference in densities within the flow channel is anticipated to be the driving force of the flow. No research was found that indicated whether natural circulation is possible with any PCMs and application dimension constraints.

Based on the change in density over the wide range of temperatures in the density test, the potential for natural circulation exists. The motivation behind a design incorporating natural circulation would be to exploit the advantages of the convection capability of a moving fluid, similar to a heat exchanger. This would further lower the average temperature reached by the heat sink and increase the temperature differential seen at the end of Figure 4.15.

A design was built, as seen in Figure 5.11. The heat source was placed at the bottom of the rig and the left side was insulated. This was done to ensure there was a “hot” leg and a “cold” leg. The hot leg would be allocation of lower density SA, while the colder leg was expected to be the heavier, more dense portion of the channel. This pressure differential, aided by gravity due to the orientation of the rig, was expected to the the driving force of the SA through the channel. The option to add active cooling was available, but not used. Therefore, the cold leg was colder, in relative terms, to the hot leg based on lack of insulation. In theory, the flow of SA was expected to flow as shown by the yellow arrows within the SA channel. The larger channel on the outside was built for the placement of room temperature vulcanization to prevent the SA from leaking out of the rig.

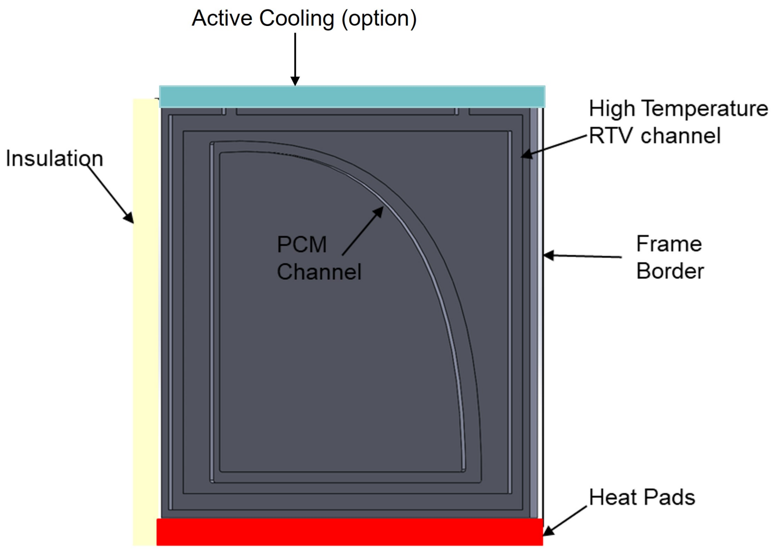

Figure 5.11. Graphic of natural circulation test design.

The rig was placed flat on a hot plate and iteratively filled with SA then cooled to ensure filling of the channels after SA worked into the crevices of the porous printed part. Yellow and blue food dye were placed in the corners of the channel, supplemented by fine glitter, as tracers to follow the SA as it moved through the channel. Figure 5.12 shows the filling process.

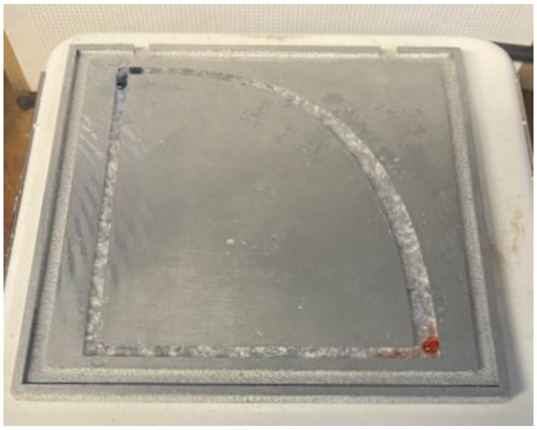

Figure 5.12. Filling of SA channel for natural circulation test.

Figure 5.13 and Figure 5.14 show the front and top views of the setup of the rig, respectively. The rig was mated together with the part profile by a pressure force between two insulating, transparent pieces of orange polysulfone. A bolted frame was used to provide the pressure force. The Al-4008 profile was machined approximately flat to remove surface roughness due to the jetting process. There was a coating of soybean oil placed on the front of the polysulfone to ensure a clear viewing window during testing. The test was conducted by placing the test rig on 4 resistance heaters and supplying 8.25 V to ensure the melting of the SA. A flashlight was used to ensure light was focused on the part while two cameras recorded the heat up. Leakage of the SA persisted on multiple iterations of the test. A new test was developed using O-rings, but has so far experienced similar leakage issues.

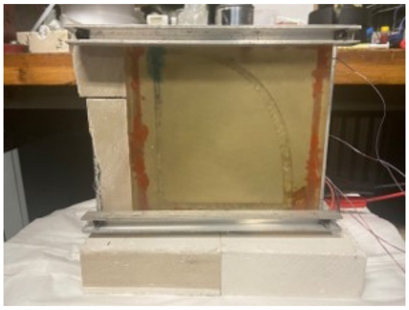

Figure 5.13. Front view.

Figure 5.14. Top view.

CHAPTER 6:
Conclusions and Future Work

6.1 Conclusions

Based on the results of the power cycle results, it is clear that the objectives of Section 1.2 were met during the study since, in all tests:

- The SA-filled heat sink reduced the average temperature of a cyclically thermally loaded component compared to heat sinks of similar geometry and thermophysical properties.
- The SA-filled heat sink reduced the peak temperature of a cyclically thermally loaded component compared to heat sinks of similar geometry and thermophysical properties.
- The SA-filled heat sink regulated the thermal transient by maintaining the temperature of a cyclically thermally loaded component within a narrow, consistent temperature range. Heat sinks of similar geometry and thermophysical properties did not achieve the same results.

The application selected was a CPU subjected to cyclic thermal loads CPU and SA was a practicable PCM for the temperature range based on its melting point and ability to isothermally absorb heat near temperatures of concern for the CPU. Two heat sink designs were determined to be practicable: a heat sink with bulk PCM in the middle and a heat sink design with an externally wrapped reservoir containing SA. The reservoir design proved to have superior thermal management capability based on the larger surface area for heat transfer within the internal fins of the design and the exploitation of the transient heat transfer to the reservoir during heat up. This was validated through an ANSYS 2D transient thermal simulation, where the reservoir design reached an average temperature of 68.8 °C compared to the 71.9 °C reached by the bulk design.

Hollow heat sinks were printed using a two-part printing process, where the lid was printed prior to the design. Stopping the print to install the lid did not appreciably change print time or quality of the part. SA was added to the part using a proven post-manufacturing and filling process using a hand-pumped vacuum and a separated tub of boiling water to slowly melt the SA. Penetrations into the SA-filled area were sealed with a stainless steel coating. There was some degradation of the sealant over time, but did not require re-coating more than once over the course of many tests.

Power cycle tests were completed for short duty cycles (30 seconds) over the course of at least one hour as well as long duty cycles (100, 200 and 300 second half periods) over a short period of time (3 iterations). The first set of power cycles compared performance of a SA-filled heat sink and a solid heat sink. The SA heat sink performed better at various power levels within the CPU application range. In no case did the solid heat sink perform better than the SA-filled heat sink. The second set of tests showed the stability of a SA-filled heat sink with respect to average temperature reached over the course of multiple cycles of various half-periods. The SA-filled heat sink was compared to four other heat sinks: a solid heat sink, a hollow (air-filled) heat sink, a soybean oil-filled heat sink and a glycerol-filled heat sink. The solid heat sink was used for comparison to a traditional heat sink. The hollow heat sink was used for comparison of a heat sink of similar geometry. The soybean oil-filled and glycerol-filled heat sinks were used for comparison to a heat sink of similar geometry and thermophysical properties to SA that did not change phase during the tests. In all tests and against all other heat sinks, the SA-filled heat sink performed better with respect to the goals of this study. For the SA-filled heat sink, the average temperature reached was lower and the thermal transient of the modeled CPU was lower. Thus, both thermal stresses that may effect a chassis as well as temperature variations that may effect some sensitive electronics such as a CPU were lower in the SA-filled heat sink. The power cycle tests concluded SA is an effective PCM for thermal management and that PCM incorporation into heat sinks is an effective thermal management strategy overall.

Alternate designs that were impractical within the temperature constraints of this study were the SA addition during printing and the natural circulation design. To support the temperature of the printing process, FM was selected as the metal PCM based on non-toxicity. The process of filling the FM into a printed part was proven possible during the print process. The printed part also contributed to the thermal conductivity calculation of the combined FM and Al-4008 part. The resulting thermal conductivity for the FM and Al-4008 combination was 100.09 W/mK. For comparison. the thermal conductivity of the SA and Al-4008 part was calculated to be 68.85 W/mK. The FM-filled heat part also proved the ability to create a PCM-filled part with less post-processing and less PCM-filled area penetration. This increases part generation efficiency and reduces risks associated with potential leakage of PCM during cycles reaching normal operating temperatures. The natural circulation design requires further testing to see if it can be implemented into the fin of a heat sink. The dimensional constraints proved this to be a difficult problem to solve.

The design space study revealed that the ElemX allows for the creation of a testable heat sink with a mass of up to 0.9 kg and contact area of 840 cm^2 (29 cm x 29 cm) which will yield a power of about 4000 W through.

When determining the PCM to be used, testing should be done to determine the onset of the PCM melting for a given application's power output and required component temperature range for optimal performance. SA worked within these tests to reduce to average temperature during thermal cycles. However, a PCM with a lower average melting temperature may have provided further improved results.

This research contributed the following to the fields of thermal management and additive manufacturing:

- It established a design methodology which can be applied and repeated for any PCM.
- It developed efficient methods for adding PCM into hollow parts.
- It proved the capability of using SA within additively manufactured parts as a passive thermal management technique to reduce the average peak temperature of a temperature-sensitive component.
- It proved the capability of using AM methods for thermal management device manufacturing.

6.2 Recommendations for Future Work

Based on the research, testing and results of this study, the following recommendations for future work are provided.

- Research material interactions and thermal management capability of the SA following the power cylce testing.
- Perform testing within an operating desktop computer.
- Perform a dedicated study into SA thermophysical properties.

- Complete further research into natural circulation capabilities, to include simulations.
- Conduct material interaction analysis of FM and Al-4008 substrate at various temperatures.
- Evaluate alternative AM techniques for compatibility with heat sink development and PCM incorporation.
- Develop PCM composites of SA and FM for testing.
- Perform similar research with a higher temperature, Navy-specific application.

APPENDIX A:
Design Space Study MATLAB Code

```
clear all;close all;clc;
count = 1;
set(gca,'fontsize',12)
% Triangular fin (eqn 3.98 incropera & Dewitt 7th ed)
% Range variables:
% w (wideness of fin)
% t (thickness of base of fin)
% L (length of fin from base to tip)
% S (fin pitch must be larger than t)
t = 0.003;
finspacing=0.001;
S = t+finspacing;
h = 10;
k = 148;
Tb=110;
Tinf = 25;
thetab = Tb-Tinf;
m = sqrt((2*h/(k*t)));
basethickness = 0.003; % Minimum thickness
materialdensity = 2730; % Density of Al 4008

iii_array = 0.01:0.01:.298;
jjj_array = 0.01:0.01:.298;
flflfl_array = 0.001:0.01:0.2;

DATA = zeros([numel(iii_array)*numel(jjj_array)*numel(flflfl_array) 4]);

for iii = iii_array
    for jjj = jjj_array
        for flflfl =flflfl_array
        Nfins = floor(jjj/S);
        w = iii;
        L = flflfl;
```

```
        Vbase = w.*basethickness.*S.*Nfins;

        finheight = sqrt((L.^2+(0.5.*t).^2));
        Af = 2.*w.*finheight;
        Vf = 0.5.*t.*finheight.*w;

        eta_f = 1/(m*L)*(besseli(1,2*m*L)/besseli(0,2*m*L));

        Qmaxfin = h.*Af.*thetab;
        Qf = Qmaxfin.*eta_f;

        Abase=(finspacing)*w.*Nfins;
        Atotal = Nfins.*Af+Abase;

        Qmaxarray = h.*Atotal.*thetab;
        eta_o = 1-(Nfins.*Af)./Atotal.*(1-eta_f); % Array efficiency eqn 3.107

        Qtarray = eta_o.*Qmaxarray;
        massofSink = (Vf+Vbase).*materialdensity;
        HSArea = w.*S.*Nfins;

        DATA(count,:) = [HSArea massofSink Qtarray Nfins];
        count = count + 1;

        end

        if massofSink<0.91 & Nfins>0
            figure(1)
            plot3(DATA(:,1),DATA(:,2),DATA(:,3),'o');
            xlabel('Heat Sink Area (m^2)');
            ylabel('Heat Sink Mass (kg)');
            zlabel('Heat Sink Power (W)');
            figure(2)
            plot(DATA(:,1),DATA(:,2),'o');
            xlabel('Heat Sink Area (m^2)');
            ylabel('Heat Sink Mass (kg)');
            figure(3)
            plot(DATA(:,1),DATA(:,3),'o');
            xlabel('Heat Sink Area (m^2)');
```

```
            ylabel('Heat Sink Power (W)');
            figure(4)
            plot(DATA(:,2),DATA(:,3),'o');
            xlabel('Heat Sink Mass (kg)');
            ylabel('Heat Sink Power (W)');
            figure(5)
            plot(DATA(:,1),DATA(:,4),'o');
            xlabel('Heat Sink Area (m^2)');
            ylabel('Number of Fins');

        end
    end
end
```

THIS PAGE INTENTIONALLY LEFT BLANK

APPENDIX B:
Thermal Conductivity MATLAB Code

```
clc; clear all; close all
%PCM Thermal Conductivity Test
set(gca,'fontsize',12)
% Raw Data
file = "C:\Users\txg50\Documents\NPS\Thesis\11May23FieldsThermCond110C"
Temperatures = readmatrix(file);
Time=Temperatures(1:12176,1);
Tamb = Temperatures(1:12176,2);
T1 = Temperatures(1:12176,3);
T2 = Temperatures(1:12176,4);
T3 = Temperatures(1:12176,5);
T4 = Temperatures(1:12176,6);
T5 = Temperatures(1:12176,7);
T6 = Temperatures(1:12176,8);

% Plot
plot(Time,T1)
hold on
xlabel 'Time (s)'; ylabel(strcat("Temperature (",char(176),"C)")); grid minor
plot(Time,T2)
plot(Time,T3)
plot(Time,T4)
plot(Time,T5)
plot(Time,T6)
xlim([0 4000])
legend("TC1","TC2","TC3","TC4","TC5","TC6", 'location','southeast')

% Calculating Thermal Conductivity
T1forCalc = Temperatures(end-1,3);
T2forCalc = Temperatures(end-1,4);
T3forCalc = Temperatures(end-1,5);
T4forCalc = Temperatures(end-1,6);
T5forCalc = Temperatures(end-1,7);
```

```
T6forCalc = Temperatures(end-1,8);


R1dx = 14.85;
Fieldsdx = 46.80;
R2dx = 15.88;

R1dT = T1forCalc-T2forCalc;
FieldsdT = T3forCalc-T4forCalc;
R2dT = T5forCalc-T6forCalc;

KAl = 148; %from matweb.com
AR1 = pi*(25.15/2)^2 %mm^2
AS = pi*(24.90/2)^2
AR2 = pi*(25.18/2)^2


QR1 = AR1*KAl*(R1dT/R1dx);
QS = AS*KAl*(FieldsdT/Fieldsdx);
QR2 = AR2*KAl*(R2dT/R2dx);155.538
Qave = (QR1+QR2)/2;
KR1 = (Qave*R1dx)/(AR1*R1dT);
KS = (Qave*Fieldsdx)/(AS*FieldsdT);
KR2 = (Qave*R2dx)/(AR2*R2dT);

KS1 = (KAl*R1dT*Fieldsdx)/(FieldsdT*R1dx);
KS2 = (KAl*R2dT*Fieldsdx)/(FieldsdT*R2dx);
Kave = (KS1+KS2)/2;
KComp1 = (KAl*R2dT*R1dx)/(R1dT*R2dx);
KComp2 = (KAl*R1dT*R2dx)/(R2dT*R1dx);

disp("Cacluations Using Qave:")
disp("------------------------------------------------------------")
fprintf("QR1:  %.3f W\n",QR1)
fprintf("QS:  %.3f W\n",QS)
fprintf("QR2:  %.3f W\n",QR2)
fprintf("Qave:  %.3f W\n",Qave)
fprintf("Thermal Conductivity of Reference 1:   %.3f W/mK\n",KR1)
fprintf("Thermal Conductivity of Sample:   %.3f W/mK\n",KS)
fprintf("Thermal Conductivity of Reference 2:   %.3f W/mK\n",KR2)
```

```
disp(" ")
disp("Calculations Equating Q")
disp("--------------------------------------------------------------")
fprintf("Thermal Conductivity Using Bottom Reference:   %.3f W/mK\n",KS1)
fprintf("Thermal Conductivity Using Top Reference:   %.3f W/mK\n",KS2)
fprintf("Average TC of Top and Bottom Reference:   %.3f W/mK\n",Kave)
fprintf("Thermal Conductivity for Ref 1 using Ref 2:   %.3f W/mK\n",KComp1)
fprintf("Thermal Conductivity for Ref 2 using Ref 1:   %.3f W/mK\n",KComp2)
```

THIS PAGE INTENTIONALLY LEFT BLANK

APPENDIX C:
Power Cycles MATLAB Code

```
%S1
clear all;clc;close all

S1file = "C:\Users\txg50\Documents\NPS\Thesis\Vessel Tests New\04Feb23 " + ...
    "Solid Wrapped HS V1 100s High Time 9V from 73C at Mid"; %Solid HS Test Data File
pcm1file = "C:\Users\txg50\Documents\NPS\Thesis\Vessel Tests New\04Feb23 " + ...
    "PCM Wrapped HS V1 100s High Time 9V from 73C at Mid";
set(gca,'fontsize',12)
%Reading Data
S1 = dlmread(S1file,'');
PCM1 = dlmread(pcm1file,'');

%Creating Matrices
Stime = S1(:,1);
SHP = S1(:,6);

pcmtime = PCM1(:,1);
pcmHP = PCM1(:,6);

%Attenuating Time Matrix
j = 1;
if length(Stime) > length(pcmtime)
    while j <= length(pcmtime)
        time(j) = pcmtime(j);
        SHP(length(pcmtime)+1:end) = [];
        j = j + 1;
    end
elseif length(pcmtime) > length(Stime)
    while j <= length(Stime)
        time(j) = Stime(j);
        pcmHP(length(Stime)+1:end) = [];
        j = j + 1;
    end
```

```
elseif length(Stime) == length(pcmtime)
    disp("length of stime == length of pcmtime")
    while j <= length(pcmtime)
        time(j) = Stime(j);
        j = j + 1;
    end
end

%Plotting Data
j = 1;
while j <= length(time)
    MP(j) = 69;
    j = j + 1;
end

%Heat Pad Temperature Comparisons
hold on
plot(time,MP,'k--')
plot(time,SHP,'r-')
plot(time,pcmHP,'b-')
SPeaks = islocalmax(SHP);
SHighTemps=SHP(SPeaks);
pcmHighTemps=pcmHP(SPeaks);
timeHighTemps=time(SPeaks);
p1 = [timeHighTemps(2) SHighTemps(2)];
p2 = [timeHighTemps(2) pcmHighTemps(2)];
dp = p2-p1;
dpT=round(p1(2)-p2(2),1);
quiver(p1(1),p1(2),dp(1),dp(2),0,'k-.')
p3 = [timeHighTemps(3) SHighTemps(3)];
p4 = [timeHighTemps(3) pcmHighTemps(3)];
dp2 = p4-p3;
dpT2=round(p3(2)-p4(2),1);
quiver(p3(1),p3(2),dp2(1),dp2(2),0,'k-.')
text(timeHighTemps(2),SHighTemps(2)-dpT/2, ['\leftarrow\DeltaT=', ...
    num2str(dpT) ,char(176),'C'],'FontSize',12)
text(timeHighTemps(3),SHighTemps(3)-dpT2/2, ['\leftarrow\DeltaT=', ...
    num2str(dpT2) ,char(176),'C'],'FontSize',12)
hold on
grid on
```

```
grid minor
legend("SA Melting Point","Heaters (Solid)","Heaters (SA)",'Location','southeast')
SCImage=imread('SpaceClaimPCMonSides.jpg');
hold on
image(SCImage,'xdata',[550 600],'ydata',[95 90])
xlabel("Time (s)")
xticks([200 300 400 500 600])
xlim([200 time(end)])
ylim([65 95])
ylabel(strcat("Temperature (",char(176),"C)"))
```

THIS PAGE INTENTIONALLY LEFT BLANK

APPENDIX D:
LABVIEW Interface (Front Panel)

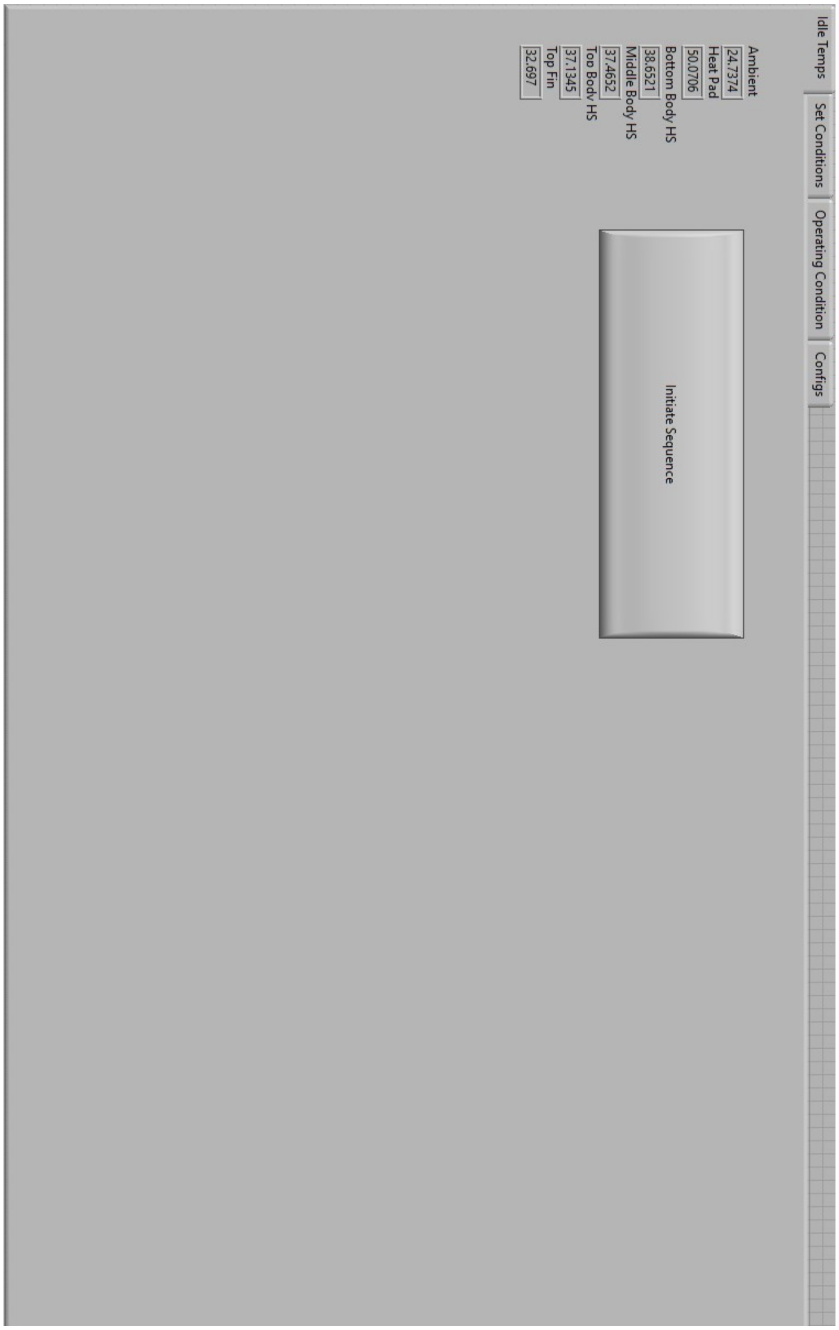

Ambient
24.7374
Heat Pad
50.0706
Bottom Body HS
38.6521
Middle Body HS
37.4652
Top Body HS
37.1345
Top Fin
32.697

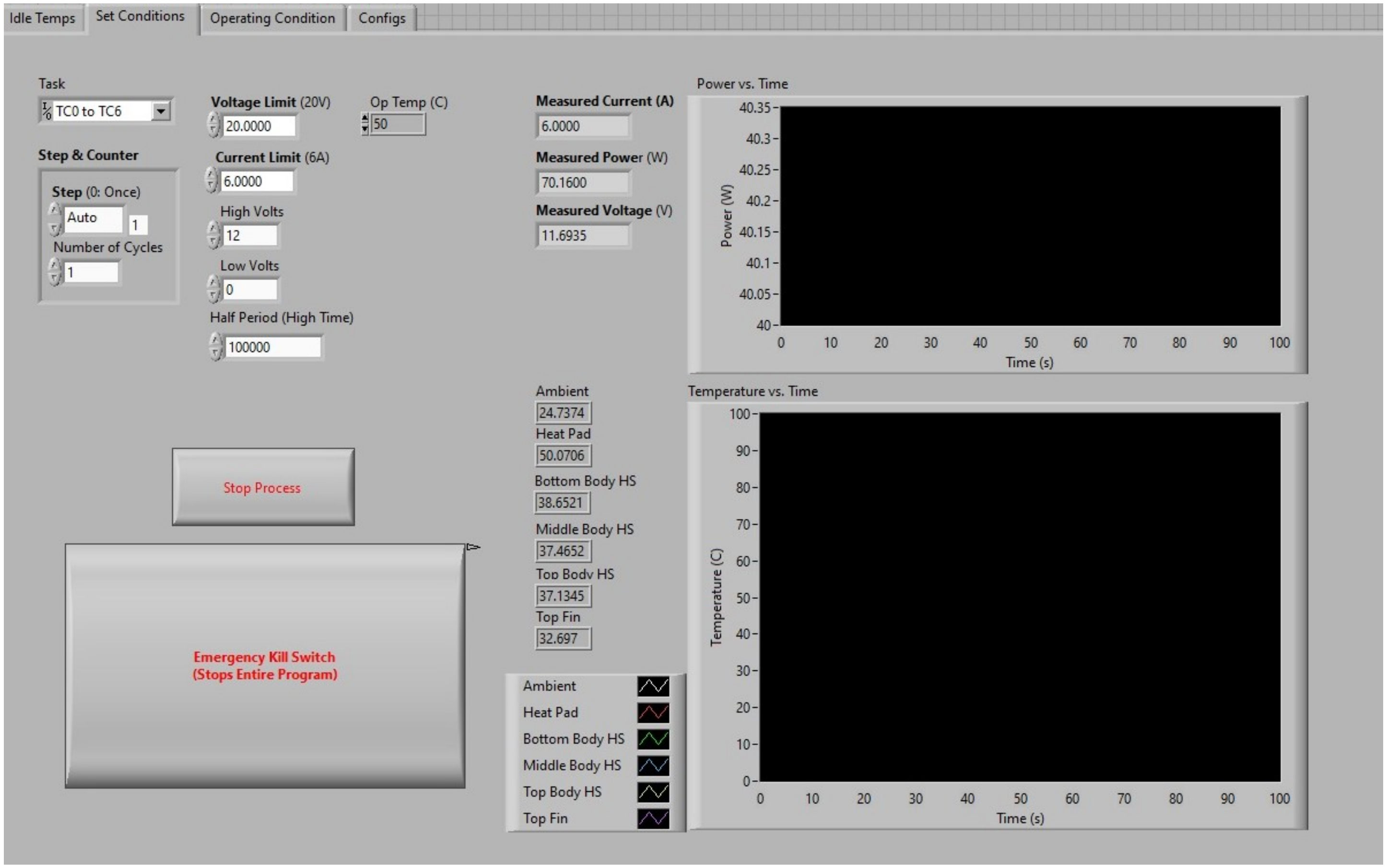

Task: TC0 to TC6

Step & Counter

Step (0: Once): Auto 1

Number of Cycles: 1

Voltage Limit (20V): 20.0000

Op Temp (C): 50

Current Limit (6A): 6.0000

High Volts: 12

Low Volts: 0

Half Period (High Time): 100000

Measured Current (A): 6.0000

Measured Power (W): 70.1600

Measured Voltage (V): 11.6935

Ambient: 24.7374

Heat Pad: 50.0706

Bottom Body HS: 38.6521

Middle Body HS: 37.4652

Top Body HS: 37.1345

Top Fin: 32.697

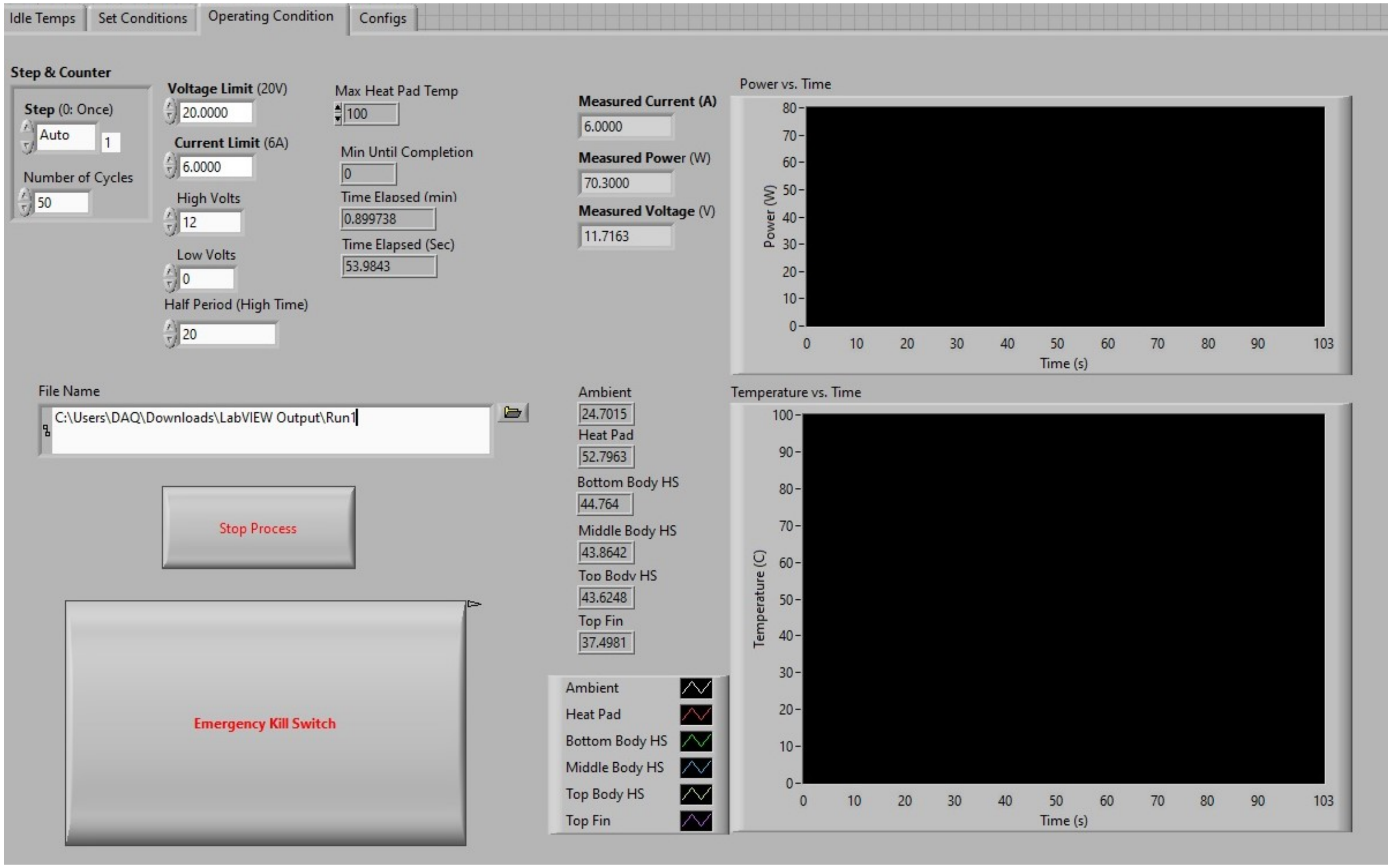

Step (0: Once): Auto 1

Number of Cycles: 50

Voltage Limit (20V): 20.0000

Current Limit (6A): 6.0000

High Volts: 12

Low Volts: 0

Half Period (High Time): 20

Max Heat Pad Temp: 100

Min Until Completion: 0

Time Elapsed (min): 0.899738

Time Elapsed (Sec): 53.9843

Measured Current (A): 6.0000

Measured Power (W): 70.3000

Measured Voltage (V): 11.7163

File Name: C:\Users\DAQ\Downloads\LabVIEW Output\Run1

Ambient: 24.7015

Heat Pad: 52.7963

Bottom Body HS: 44.764

Middle Body HS: 43.8642

Top Body HS: 43.6248

Top Fin: 37.4981

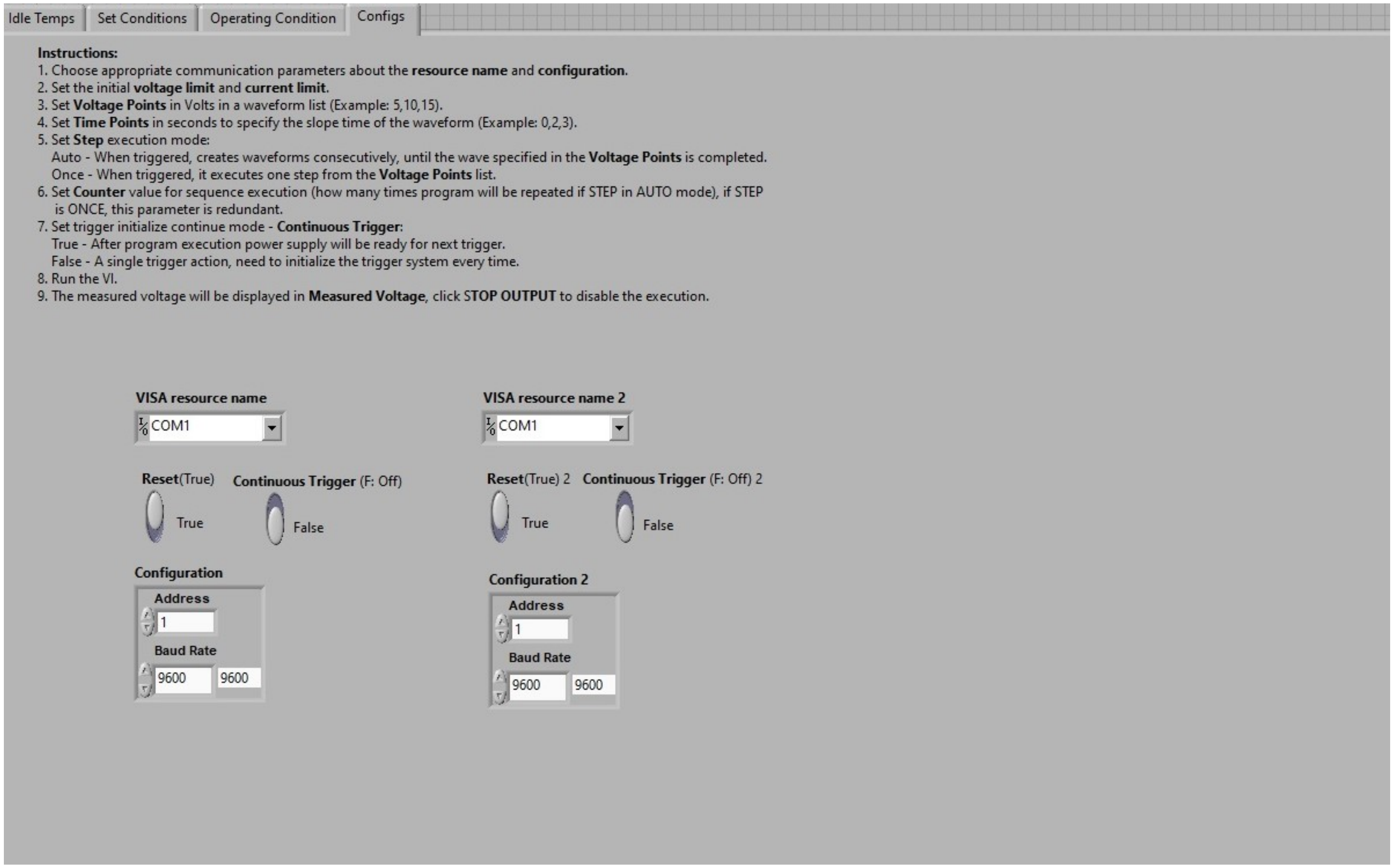

Instructions:

1. Choose appropriate communication parameters about the **resource name** and **configuration**.
2. Set the initial **voltage limit** and **current limit**.
3. Set **Voltage Points** in Volts in a waveform list (Example: 5,10,15).
4. Set **Time Points** in seconds to specify the slope time of the waveform (Example: 0,2,3).
5. Set **Step** execution mode:
   Auto - When triggered, creates waveforms consecutively, until the wave specified in the **Voltage Points** is completed.
   Once - When triggered, it executes one step from the **Voltage Points** list.
6. Set **Counter** value for sequence execution (how many times program will be repeated if STEP in AUTO mode), if STEP is ONCE, this parameter is redundant.
7. Set trigger initialize continue mode - **Continuous Trigger**:
   True - After program execution power supply will be ready for next trigger.
   False - A single trigger action, need to initialize the trigger system every time.
8. Run the VI.
9. The measured voltage will be displayed in **Measured Voltage**, click **STOP OUTPUT** to disable the execution.

VISA resource name: COM1

Reset(True): True

Continuous Trigger (F: Off): False

Configuration
Address: 1
Baud Rate: 9600 9600

VISA resource name 2: COM1

Reset(True) 2: True

Continuous Trigger (F: Off) 2: False

Configuration 2
Address: 1
Baud Rate: 9600 9600

APPENDIX E: LABVIEW Code (Back Panel)

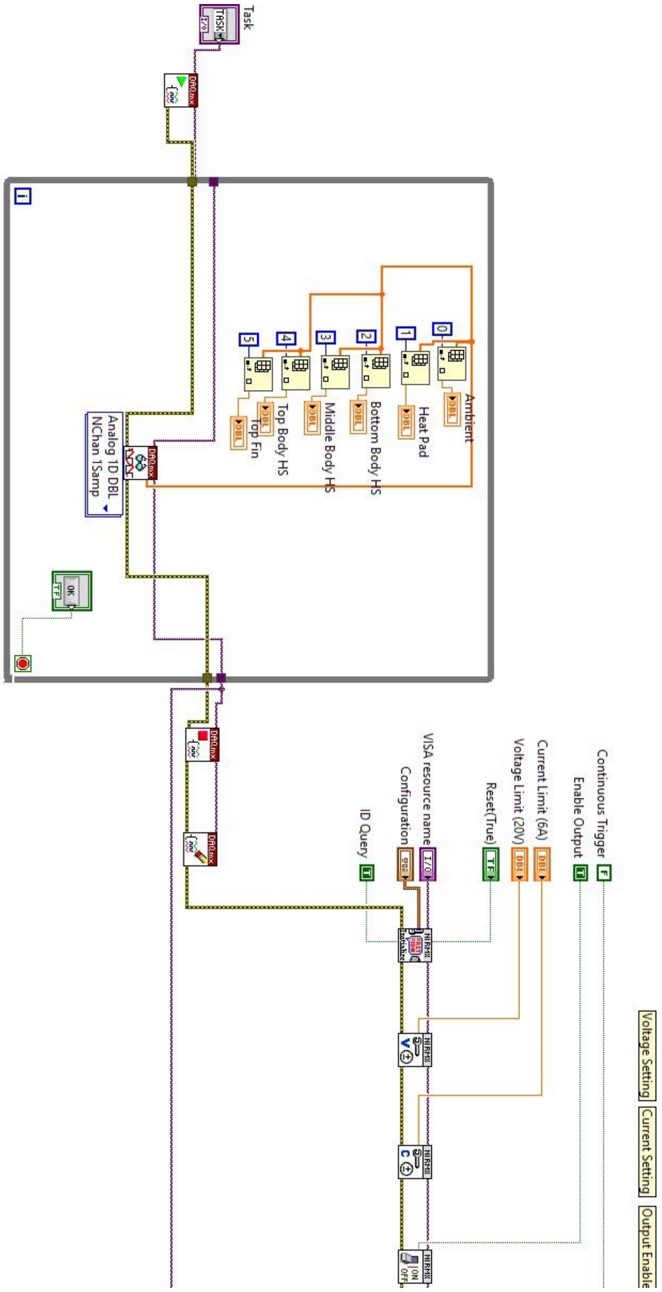

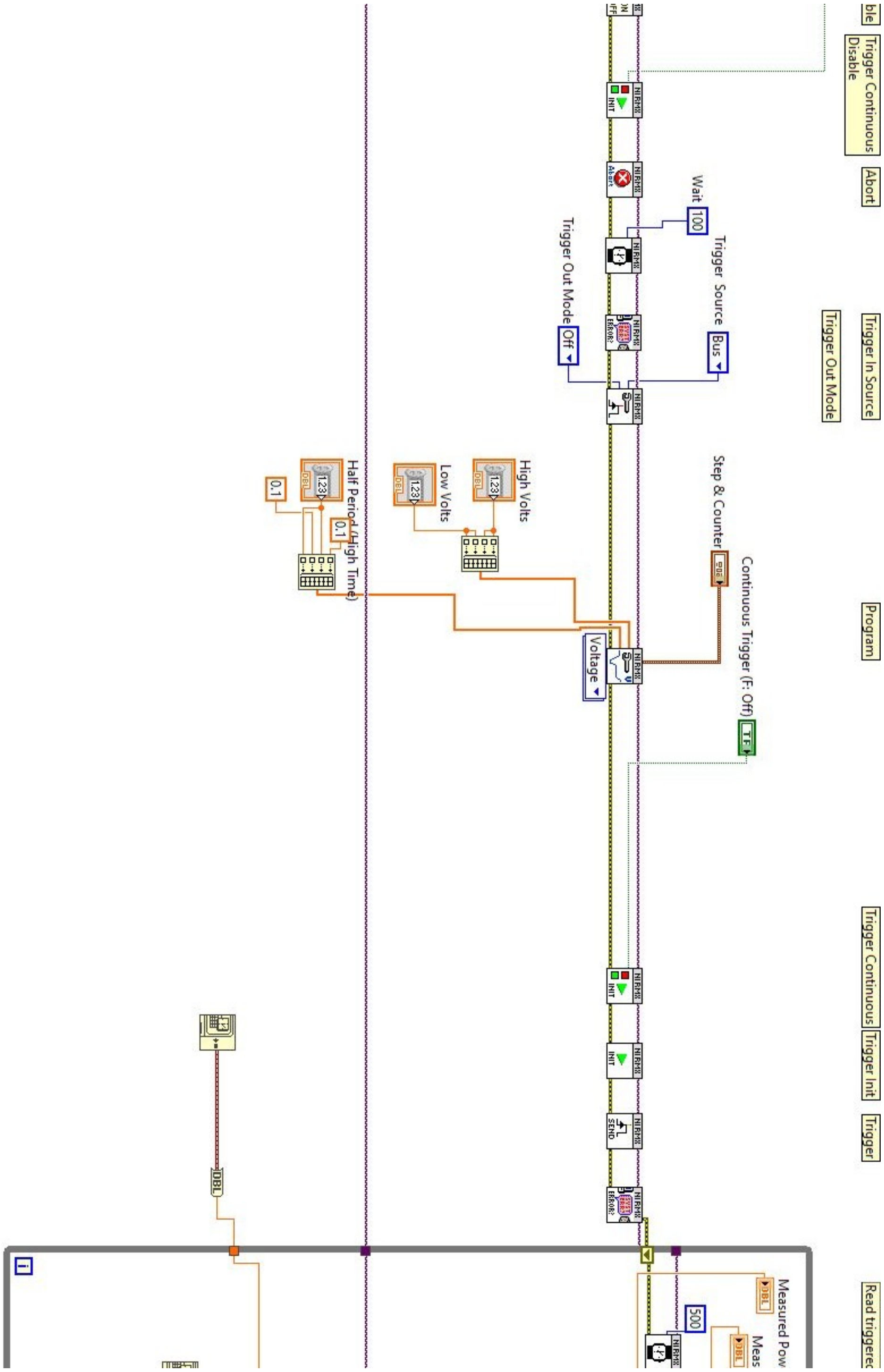
Trigger Continuous Disable
Abort
Wait
100
Trigger Source
Bus
Trigger Out Mode
Off
Trigger In Source
Trigger Out Mode
High Volts
Low Volts
Half Period (High Time)
0.1
0.1
Step & Counter
Continuous Trigger (F: Off)
Voltage
Program
Trigger Continuous
Trigger Init
Trigger
DBL
500
Measured Pow
Meas
Read triggerec

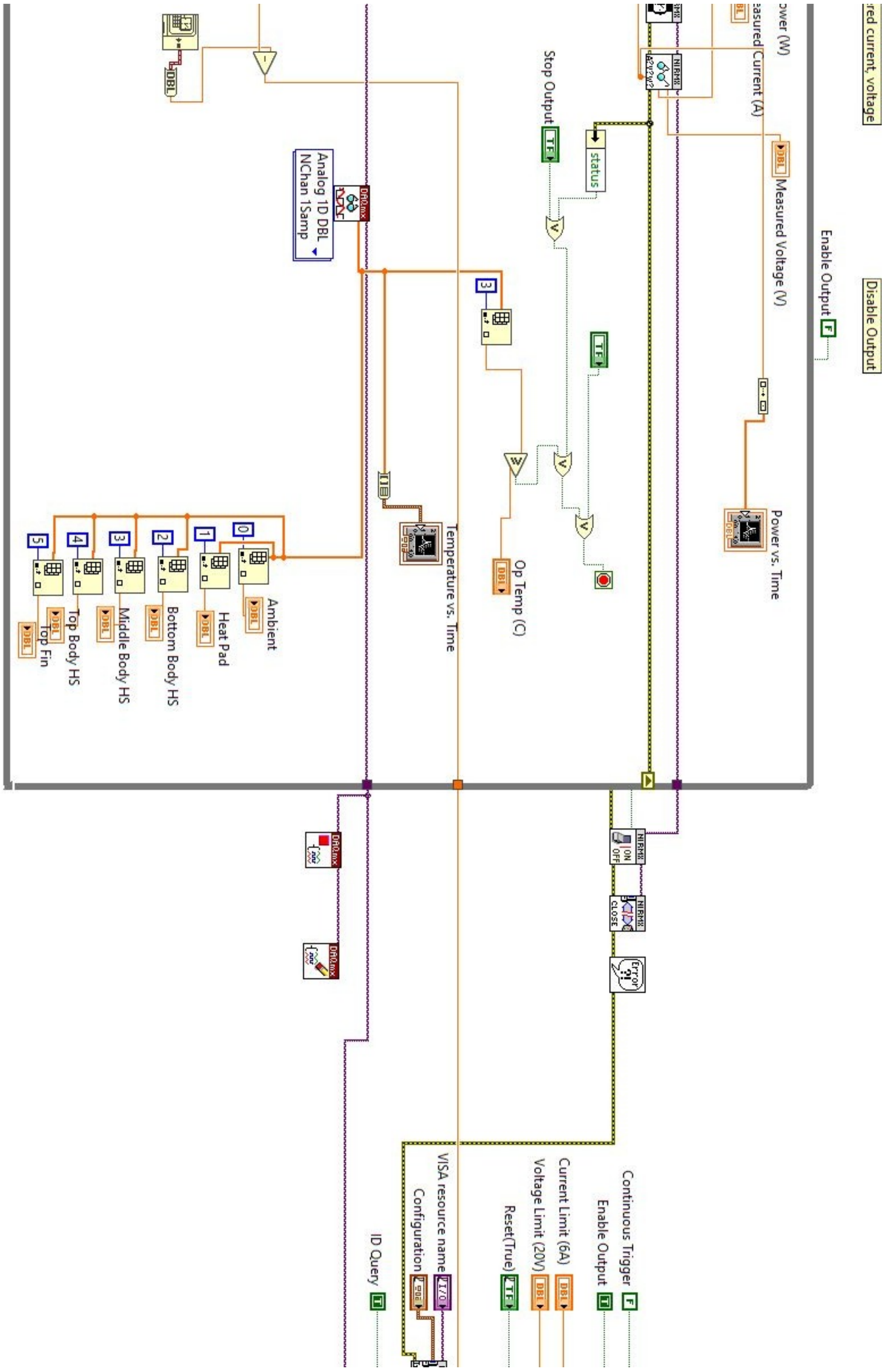
red current, voltage
Disable Output
Enable Output
ower (W)
easured Current (A)
Measured Voltage (V)
Stop Output
status
Analog 1D DBL
NChan 1Samp
DAQmx
Power vs. Time
Op Temp (C)
Temperature vs. Time
3
0
1
2
3
4
5
Ambient
Heat Pad
Bottom Body HS
Middle Body HS
Top Body HS
Top Fin
DBL
TF
ON OFF
CLOSE
Error
Continuous Trigger
Enable Output
Current Limit (6A)
Voltage Limit (20V)
Reset(True)
VISA resource name
Configuration
ID Query

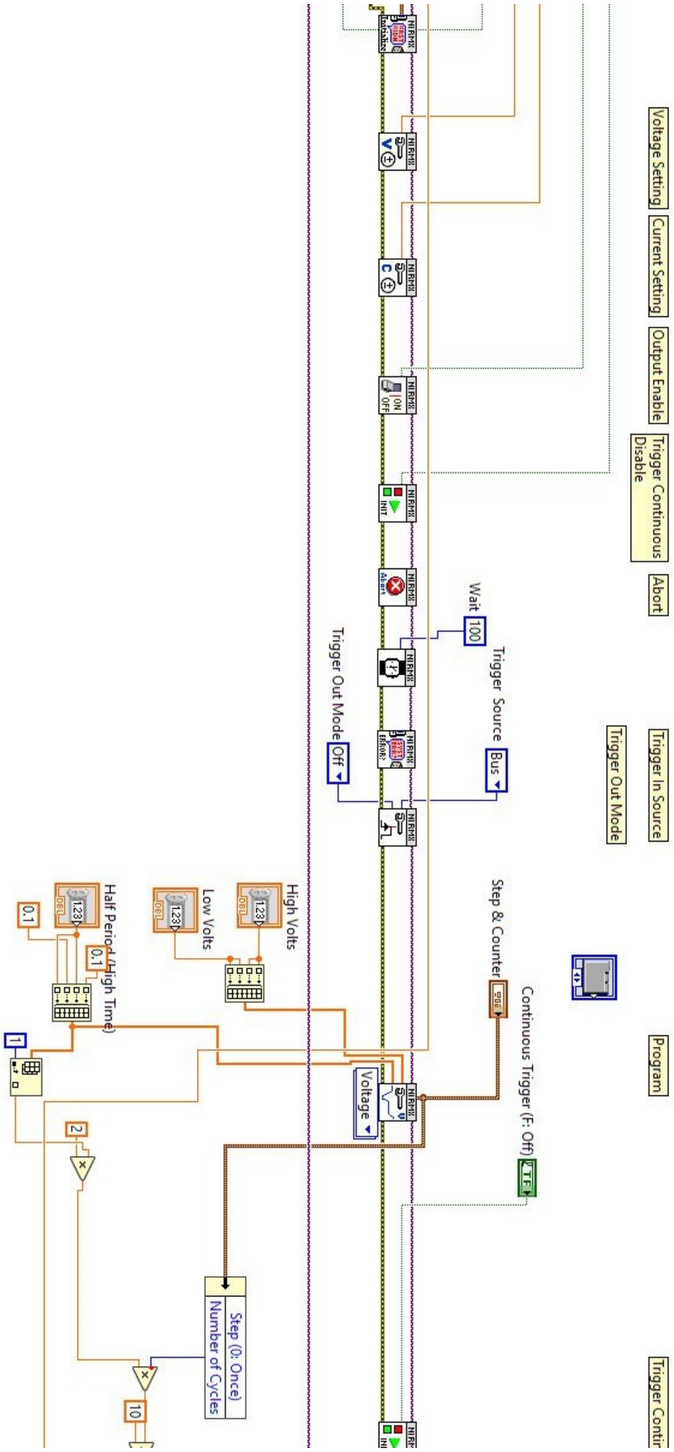
Voltage Setting
Current Setting
Output Enable
Trigger Continuous Disable
Abort
Trigger In Source
Trigger Out Mode
Program
Trigger Conti
Wait
100
Trigger Source
Bus
Trigger Out Mode
Off
Step & Counter
Continuous Trigger (F: Off)
High Volts
Low Volts
Half Period (High Time)
0.1
0.1
1
2
10
Voltage
Step (0: Once)
Number of Cycles

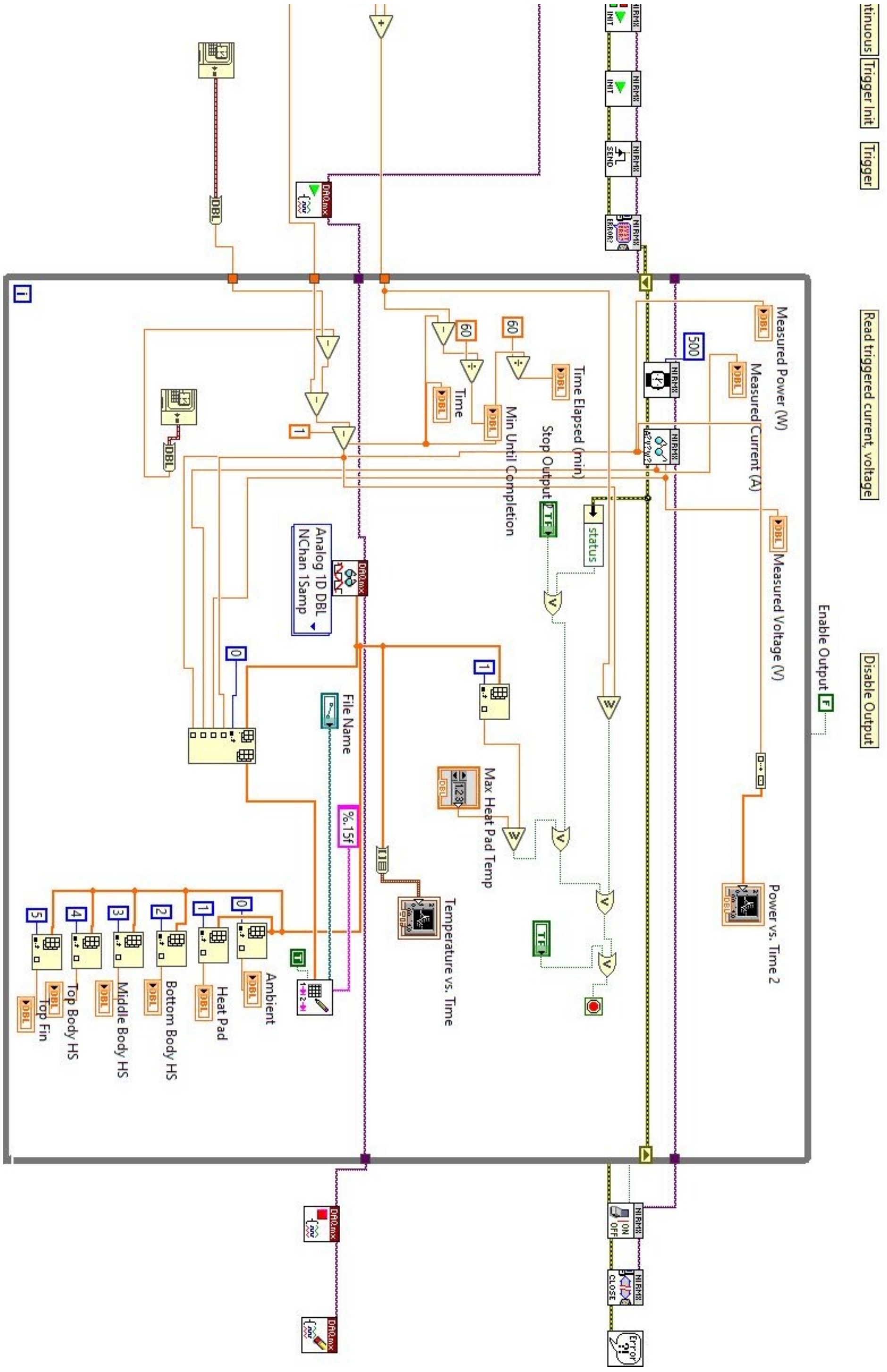
tinuous
Trigger Init
Trigger
Read triggered current, voltage
Disable Output
Enable Output
Measured Power (W)
Measured Current (A)
Measured Voltage (V)
500
Time Elapsed (min)
Stop Output
Min Until Completion
Time
60
60
1
status
Analog 1D DBL
NChan 1Samp
0
1
File Name
%.15f
Max Heat Pad Temp
Temperature vs. Time
Power vs. Time 2
5
4
3
2
1
0
Ambient
Heat Pad
Bottom Body HS
Middle Body HS
Top Body HS
Top Fin
DAQmx
NI RMX
INIT
SEND
ERROR?
ON OFF
CLOSE
Error

THIS PAGE INTENTIONALLY LEFT BLANK

List of References

[1] V. Lakshminarayanan and N. Sriraam, “The effect of temperature on the reliability of electronic components,” in *2014 IEEE International Conference on Electronics, Computing and Communication Technologies (CONECCT)*, 2014, pp. 1–6 [Online]. Available: https://doi.org/10.1109/CONECCT.2014.6740182

[2] X. Jin, M. H. Azarian, C. Lau, L. Cheng, and M. Pecht, “Physics-of-failure analysis of cooling fans,” in *2011 Prognostics and System Health Management Conference*, 2011, pp. 1–8 [Online]. Available: https://doi.org/10.1109/PHM.2011.5939584

[3] H. Jung, C. V. Subban, J. D. McTigue, J. J. Martinez, A. E. Copping, J. Osorio, J. Liu, and Z. D. Deng, “Extracting energy from ocean thermal and salinity gradients to power unmanned underwater vehicles: State of the art, current limitations, and future outlook,” *Renewable and Sustainable Energy Reviews*, vol. 160, pp. 3–9, 2022 [Online]. Available: https://doi.org/https://doi.org/10.1016/j.rser.2022.112283

[4] Advanced Cooling Technologies, “A gude to cooling RADAR electronics.” 2023 [Online]. Available: https://www.1-act.com/blog/a-guide-to-cooling-radar-electronics/

[5] Dell Inc., *Dell Power Manager User Guide Version 3.13*, Dell Technologies, 2023 [Online]. Available: https://dl.dell.com/content/manual22711377-dell-power-manager-user-s-guide-version-3-13.pdf?language=en-us

[6] Z. Wang and H. Hu, “Development of an ultra-quiet fan for computer cooling applications,” in *Fluids Engineering Division Summer Meeting*. American Society of Mechanical Engineers, 2014, vol. 46216.

[7] J. J. Magnusson, “Additive manufacturing hollow metal parts with liquid metal,” 2022-06 [Online]. Available: https://hdl.handle.net/10945/70744

[8] C. J. Anderson, “Microstructural surface incorporation of phase change materials for thermal management applications,” ESTEP, Monterey, CA 93943, 2022-06 [Online]. Available: https://hdl.handle.net/10945/70622

[9] K. Faraj, M. Khaled, J. Faraj, F. Hachem, and C. Castelain, “Phase change material thermal energy storage systems for cooling applications in buildings: A review,” *Renewable and Sustainable Energy Reviews*, vol. 119, 2020 [Online]. Available: https://doi.org/https://doi.org/10.1016/j.rser.2019.109579

[10] G. S. Sodhi, C. Botting, E. Lau, M. Palanisamy, M. Rouhani, and M. Bahrami, “Hybrid heat sinks for thermal management of passively cooled battery chargers,” *International Journal of Energy Research*, vol. 45, no. 4, pp. 6333–6349, 2021.

[11] Advanced Cooling Technologies, “Pcm types .” 2023 [Online]. Available: https://www.1-act.com/products/pcm-heat-sinks/pcmselection/

[12] D. Colarossi and P. Principi, “Experimental investigation and optical visualization of a salt gradient solar pond integrated with pcm,” *Solar energy materials and solar cells*, vol. 234, pp. 111 425–, 2022.

[13] Y. Cui, J. Xie, J. Liu, and S. Pan, “Review of phase change materials integrated in building walls for energy saving,” *Procedia Engineering*, vol. 121, pp. 763–770, 2015.

[14] R. Miraftab-Salo, “Thermal Energy Storage and Cooling Capability of Composite Field’s Metal and Paraffin Phase Changing Material (May 2022),” 2022.

[15] M. Ostrỳ, S. Bantová, and K. Struhala, “Compatibility of phase change materials and metals: Experimental evaluation based on the corrosion rate,” *Molecules*, vol. 25, no. 12, p. 2823, 2020.

[16] Cody’sLab. *Field’s Metal vs Aluminum*. (October 8, 2018). Accessed Jan. 29, 2023 [Online Video]. Available: https://www.youtube.com/watch?v=LZs21tpKgyI

[17] P. Tan, P. Lindberg, K. Eichler, P. Löveryd, P. Johansson, and A. S. Kalagasidis, “Effect of phase separation and supercooling on the storage capacity in a commercial latent heat thermal energy storage: Experimental cycling of a salt hydrate PCM,” *Journal of Energy Storage*, vol. 29, p. 101266, 2020.

[18] K. S. Reddy and S. Dufera, “Additive manufacturing technologies,” *International Journal of Management Information, Technology and Engineering*, vol. 4, pp. 89–112, 2016.

[19] G. Spinelli, R. Kotsilkova, E. Ivanov, V. Georgiev, C. Naddeo, and V. Romano, “Thermal and dielectric properties of 3D printed parts based on polylactic acid filled with carbon nanostructures,” in *Macromolecular Symposia*, no. 1. Wiley Online Library, 2022, vol. 405, p. 2100244.

[20] G. Potter, “Vader systems may have created a quantum leap in manufacturing,” *University at Buffalo News Center*, Jan 12, 2017 [Online]. Available: https://www.buffalo.edu/news/releases/2017/01/020.html

[21] MatWeb, “Overview of materials for 4000 series aluminum alloy” [Online]. Available: https://www.matweb.com/search/datasheet.aspx?matguid=a965260f643e47e98c11ae7786bdbf65

[22] J. Welty, G. L. Rorrer, and D. G. Foster, *Fundamentals of Momentum, Heat, and Mass Transfer*. John Wiley & Sons, 2020.

[23] F. Incropera and D. DeWitt, *Fundamentals of heat and mass transfer 4th edition*, 1996.

[24] D. Wentworth, “What is stearic fatty acid fsed for?” Twin Rivers Technologies, blog, Jan. 10, 2021 [Online]. Available: https://www.twinriverstechnologies.com/blog/stearic-fatty-acids#:~:text=Stearic%20acid%20is%20mainly%20used,hard%20candies%20retain%20their%20shapes.

[25] Intel Corporation, “Intel Core i5-6500 Processor Product Specifications,” 2015 [Online]. Available: https://www.intel.com/content/www/us/en/products/sku/88184/intel-core-i56500-processor-6m-cache-up-to-3-60-ghz/specifications.html

[26] Intel Corporation, “Intel Core i5-6500T Processor Product Specifications,” 2015 [Online]. Available: https://ark.intel.com/content/www/us/en/ark/products/88183/intel-core-i56500t-processor-6m-cache-up-to-3-10-ghz.html

[27] Dell Inc., “Dell OptiPlex 5040 Desktop,” 2015 [Online]. Available: https://www.dell.com/ae/business/p/optiplex-5040-desktop/pd

[28] J. Elliott, M. Lebon, and A. Robinson, “Optimising integrated heat spreaders with distributed heat transfer coefficients: A case study for cpu cooling,” *Case Studies in Thermal Engineering*, vol. 38, 2022 [Online]. Available: https://doi.org/https://doi.org/10.1016/j.csite.2022.102354

[29] W. Smith, Base code provided to the author via personal communication, 2022.

[30] H. Sertel and K. Bilen, “The effect of using sinusoidal profile in fins on thermal performance,” *International Journal of Heat and Technology*, vol. 37, no. 3, 2019.

[31] R. Elarem, T. Alqahtani, S. Mellouli, G. A. El Awadi, S. Algarni, and L. Kolsi, “Experimental investigations on thermophysical properties of nano-enhanced phase change materials for thermal energy storage applications,” *Alexandria Engineering Journal*, vol. 61, no. 9, pp. 7037–7044, 2022.

[32] A. Sharma, V. Tyagi, C. Chen, and D. Buddhi, “Review on thermal energy storage with phase change materials and applications,” *Renewable and Sustainable Energy Reviews*, vol. 13, no. 2, 2009 [Online]. Available: https://doi.org/https://doi.org/10.1016/j.rser.2007.10.005

[33] W. Su, J. Darkwa, and G. Kokogiannakis, “Review of solid–liquid phase change materials and their encapsulation technologies,” *Renewable and Sustainable Energy Reviews*, vol. 48, pp. 373–391, 2015.

[34] Rotometals, Inc., “Field’s metal safety data sheet,” 2015 [Online]. Available: https://store-cra054.mybigcommerce.com/content/FieldsSDS.pdf

[35] Rotometals, “Roto144F low-melt fusible ingot alloy - Fields metal (4 Ounces),” https://www.rotometals.com/roto144f-low-melt-fusible-ingot-alloy-fields-metal-4-ounces/, 2023. Accessed: April 30, 2023 [Online]. Available: https://www.rotometals.com/roto144f-low-melt-fusible-ingot-alloy-fields-metal-4-ounces/

[36] Rotometals, Inc., “Wood’s metal safety data sheet,” 2015 [Online]. Available: https://store-cra054.mybigcommerce.com/content/WoodsSDS.pdf

[37] W. Smith, D. Dausen, C. Luhrs, G. Lyons, M. Hong, F. Shaner, and T. Genito, “Evaluation of phase change materials insertion into additively manufactured metal parts as a thermal management strategy,” Presentation, 2022 Q2 Sponsor Project Update, Monterey, CA, 2022.

[38] F. Shaner, Thermal conductivity figures provided to the author via personal communication, June 10, 2022.

[39] ANSYS Mechanical, “Workshop 06.2: Phase change, ANSYS mechanical heat transfer,” Presentation, Provided to author via E-mail., 2019.

[40] National Institute of Science and Technology (NIST), “Octadecanoic acid,” Condensed Phase Data, 1982 [Online]. Available: https://webbook.nist.gov/cgi/cbook.cgi?ID=C57114&Mask=2#Thermo-Condensed

[41] National Institute of Science and Technology (NIST), “Octadecanoic acid,” Phase change data, 2007 [Online]. Available: https://webbook.nist.gov/cgi/cbook.cgi?ID=C57114&Units=SI&Mask=4#Thermo-Phase

[42] V. N. Chaudhari, M. K. Rathod, and K. A. Chaudhari, “Stearic acid as phase change material: Thermal reliability test and compatibility with some construction materials.” *seeds*, vol. 4, p. 5, 2013.

[43] A. Karaipekli, A. Sarı, and K. Kaygusuz, “Thermal conductivity improvement of stearic acid using expanded graphite and carbon fiber for energy storage applications,” *Renewable Energy*, vol. 32, no. 13, pp. 2201–2210, 2007 [Online]. Available: https://doi.org/https://doi.org/10.1016/j.renene.2006.11.011

[44] J. Santos, M. Santos, J. Dantas, M. M. Conceição, P. Athaide-Filho, and A. Souza, "Comparative study of specific heat capacities of some vegetable oils obtained by dsc and microwave oven," *Journal of thermal analysis and calorimetry*, vol. 79, pp. 283–287, 2005.

[45] A. C. Okafor and T. O. Nwoguh, "A study of viscosity and thermal conductivity of vegetable oils as base cutting fluids for minimum quantity lubrication machining of difficult-to-cut metals," *The International Journal of Advanced Manufacturing Technology*, vol. 106, pp. 1121–1131, 2020.

[46] R. T. Nassu and L. A. G. Gonçalves, "Determination of melting point of vegetable oils and fats by differential scanning calorimetry (dsc) technique." *Grasas y Aceites*, vol. 50, no. 1, pp. 16–21, 1999.

[47] National Institute of Science and Technology (NIST), "Glycerin," Condensed Phase Data, 1982 [Online]. Available: https://webbook.nist.gov/cgi/cbook.cgi?ID=C56815&Mask=2#Thermo-Condensed

[48] P. S. G. Medeiros, C. R. F. Barbosa, F. d. A. O. Fontes *et al.*, "Effects of addition glycerol co-product of biodiesel in the thermophysical properties of water-glycerol solution applied as secondary coolant," 2010.

[49] National Institute of Science and Technology (NIST), "Glycerin," Phase change data [Online]. Available: https://webbook.nist.gov/cgi/cbook.cgi?ID=C56815&Mask=4#Thermo-Phase

[50] G. Baran and A. Sari, "Phase change and heat transfer characteristics of a eutectic mixture of palmitic and stearic acids as PCM in a latent heat storage system," *Energy Conversion and Management*, vol. 44, no. 20, pp. 3227–3246, 2003 [Online]. Available: https://doi.org/https://doi.org/10.1016/S0196-8904(03)00104-3

THIS PAGE INTENTIONALLY LEFT BLANK

Initial Distribution List

1. Defense Technical Information Center
   Ft. Belvoir, Virginia

2. Dudley Knox Library
   Naval Postgraduate School
   Monterey, California